Journal of Luminescence 269 (2024) 120462

Contents lists available at ScienceDirect

Journal of Luminescence

journal homepage: www.elsevier.com/locate/jlumin

Review

# Recent trends in synthesis, properties, and applications of $CsPbX_3$ quantum dots: A review

Aryamol Stephen [a], A. Biju [b,*], Sona C. P [a], Jayaram Peediyekkal [a]

[a] Materials and Condensed Matter Physics Laboratory, Department of Physics, MES Ponnani College, Ponnani, Malappuram, Kerala, India
[b] Department of Physics, MES Asmabi College Kodungallur, Thrissur, Kerala, India

ARTICLE INFO

*Keywords:*
Quantum dots
Lead halide perovskites
Perovskite quantum dot
Optical properties

ABSTRACT

All inorganic Cesium lead halide perovskite quantum dots ($CsPbX_3$ QDs, X = Cl, Br, I) have sparked a great interest due to their remarkable properties and wide range of applications in optoelectronic devices. These perovskite quantum dots exhibit unique characteristics such as high photoluminescence quantum yield, tunable emission, narrow emission spectrum, and high carrier mobility, making them highly desirable for luminescent applications. Moreover, the introduction of various strategies aimed at enhancing stability and photoluminescent properties, along with the utilization of all-inorganic compositions, has established a resilient foundation for the development of ambient-stable quantum dot devices. This review reports recent advancements in $CsPbX_3$ quantum dots, encompassing their structure, synthesis methods, and morphological and optical properties. Furthermore, we discuss the emerging applications of inorganic perovskite quantum dots in quantum light-emitting diodes, solar cells, nanolasers, and in electronics, highlighting their potential as key components in next-generation optoelectronic technologies.

## 1. Introduction

In the last two decades, intensive research is carried out on colloidal quantum dots (QDs) or colloidal semiconductor nanocrystals as future optoelectronic materials with unique photonic and electronic properties. Among these materials, the recently advanced perovskite QDs (PQDs) have received much attention owing to their fascinating optical properties [1]. In 1839, German mineralogist Gustav Rose [2] discovered the first perovskite $CaTiO_3$ in the Ural Mountains, and the mineral was named perovskite after Russian mineralogist Count Lev Aleksevish von Perovski [3]. Perovskite oxides were first identified because of their advantages in terms of controlled structure, strong thermal stability, high catalytic efficiency, and inexpensive cost; similarly, halide perovskites have since received a lot of attention [4–6]. Among various halide perovskites, Lead halide perovskites (LHPs) with the general formula $APbX_3$ are showing great promise in photovoltaic applications [7]. 'A' can be organic ($CH_3NH_3^+$, $CH(NH_2)_2^+$) or inorganic cation ($Cs^+$), and X is a halide ($I^-$, $Br^-$, or $Cl^-$). In recent years, LHPs have shown remarkable progress in light-emitting diodes (LEDs), photodetectors, photovoltaics, and other optoelectronic devices because of their unique properties, such as narrow spectral width {full width at half-maximum (FWHM) < 20 nm}, long charge carrier mobility, tunable bandgaps, high light-absorption coefficients, and high defect tolerance [8]. In the 1920s, Goldschmidt et al. [9] worked on perovskite family structures which became the basis of investigation of many perovskite family structures as a result, many lead halide compounds having cesium and lead were discovered in the early stages. The $CsPbX_3$ perovskite with 'X' as Cl, Br, I and their combinations was reported in 1957 by C. K Moller [10], and the $CsPbX_3$ QD system was first synthesized by Kovalenko et al. [10] in early 2015. About twenty years ago, Mitzi and his colleagues [11] first demonstrated the intriguing optoelectronic characteristics of these perovskite materials. Very recently, inorganic $CsPbX_3$ QDs have garnered a lot of attention over the past two years due to their excellent optical performances by the combination of both QDs and halide perovskites. The bandgap and emission spectra of $CsPbX_3$ QDs and Nanocrystals undergo a dramatic change due to the modification of composition and quantum size effects. As a result of its other properties such as high fluorescence quantum efficiency, narrow-tunable emission, simple solution-based synthesis, and short carrier lifetime [12], this novel material has a lot of promises for use in visible-light communication, solar cells, low-threshold lasers, photoelectric detectors, bio-imaging, LEDs [13] and wide-colour gamut [14,15], photovoltaic

* Corresponding author.
*E-mail address:* bijuanchal@gmail.com (A. Biju).

https://doi.org/10.1016/j.jlumin.2024.120462
Received 19 October 2023; Received in revised form 1 January 2024; Accepted 11 January 2024
Available online 20 January 2024

devices, and bioimaging.

In the recent past, chalcogenides of groups II-IV and III-V (CdSe/CdS, CdSe/ZnS, and PbS) have been thoroughly researched for the photoluminescence [105–108]. Due to their distinctive optical characteristics, high capacity for sunlight absorption, and easily controllable photoluminescence, chalcogenides QDs have been extensively exploited as sensitizers in solar cells. Despite significant progress, application obstacles still exist for chalcogenide-based QDs such photodegradation, QD instability, low-temperature resistance, and the need for surface passivation to encourage photoluminescence [109,110]. The $CsPbX_3$ PQDs are currently developing as an alternative to the chalcogenides QDs for various optical applications.

Due to the ionic nature and low formation energies, $CsPbX_3$ QDs easily lose halide ions and they are susceptible to environmental deterioration caused on by light, heat, moisture, oxygen, and other factors. The structure can readily be harmed or the luminescence easily degraded by the accumulation of QDs, polar solvents, or even under ultraviolet light [111]. The complicated ion structure of perovskite materials, which encourages their breakdown, and the presence of multiple crystal polymorphs, can result in instability at room temperature. The improvement of stability has emerged as a crucial topic since this inherent instability severely restricts the practical application of PQDs [12]. To overcome the stability issues, a lot of strategies, such as ligand passivation and encapsulation have been designed [106,107,112].

In this review, we emphasize $CsPbX_3$ QDs with a focus on their short history, structure, various synthesis process, optical and morphological properties, strategies for improving stability and optical properties and their current status in various optical and electronic applications. Based on the results of these studies, summarized the challenges and directions for future development. Various difficulties with the $CsPbX_3$ perovskites are also discussed.

## 2. Crystal structure

Understanding the structure-property correlations of colloidally generated PQD is essential for intelligently tuning the optical properties of these QDs. All-inorganic perovskites ($CsPbX_3$) have a fundamental crystal structure that is identical to that of methylammonium lead iodide ($CH_3NH_3PbI_3$), which is frequently used as an exemplary reference chemical [113]. The commonly used chemical formula for perovskite compounds is $ABX_3$, where A and B represent cations, and X represents an anion. The A cation occupies a cuboctahedral cavity within the corner-shared $BX_6$ octahedral framework, resulting in a three-dimensional (3D) structure. The divalent metal B is surrounded by six halogen atoms, forming the $BX_6$ octahedral structure [109]. Typically, A refers to Alkali metals (eg $K^+$, $Rb^+$, $Cs^+$) [110] alkaline earth metals (eg: $Ca^{2+}$, $Sr^{2+}$, $Ba^{2+}$) [114] or lanthanides (eg: La, Y,$Ce^{4+}$, $Nd^{3+}$, $Sm^{4+}$, $La^{3+}$, or $Gd^{3+}$) [115,116], B represents the transition metal, and X can be oxygen, any halide, nitrides or a combination of halides (Figs. 1 and 2). Temperature, doping, size geometry of cations/anions, and synthesis techniques all play a role in the production of various 3D perovskites structures [117]. Even though all mixture of $A^{1+}$, $B^{2+}$, and $X^{-1}$ can result in the intricate $ABX_3$ halide perovskite structure.

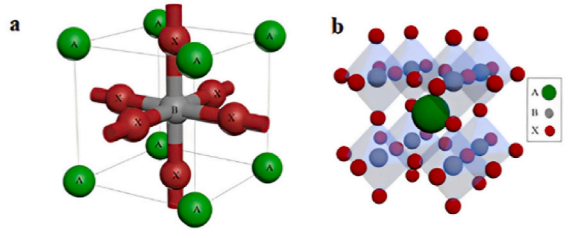


**Fig. 1.** a) The octahedral unit and b) Network crystal structure of Perovskite materials Adapted with Open access from Ref. [118].

To comprehend and quantify which combinations of chemical species can create perovskite structure, one criterion put out by Goldschmidt in the early 1920s is known as the tolerance factor ($t$) [120].

$$t = \frac{R_A + R_x}{\sqrt{2}(R_B + R_x)}$$

The ionic radii of the relevant elements at the A-site, B-site, and X-site are denoted as $R_A$, $R_B$, and $R_X$, respectively. An ideal fit and successful perovskite formation are indicated by a '$t$' value that is near to unity ($t = 1$). The A site cations' ability to fit in the cavities of the $BX_6$ octahedral framework can be assessed using the tolerance factor. Metal halide perovskite ($A^{1+}B^{2+}X_3^{1-}$), has a smaller range of cations than its oxide counterparts ($A^{2+}B^{4+}O_3^{-}$), because of two reasons. Halides are primarily able to compensate for the lower oxidation states of cations at the A-site and B-site because they possess a relatively smaller negative charge. Additionally, halides generally have larger ionic radii compared to oxides. To maintain the octahedral coordination geometry, it becomes necessary to utilize larger metal ions at the B-site due to the larger ionic radii of halides [121,122]. For lead halide perovskites, favourable $t$ value ranges between 0.85 and 1.11 [117,118]. Though lesser (0.8) or larger (>1) $t$ values lead to non-perovskite formations or in this range the cubic-like crystal structure may become tortured, distorted, and eventually destroyed [123,124]. In addition to the tolerance factor, the extra semiempirical geometric parameter known as the octahedral factor ($\mu$) is utilized to assess the octahedral stability [125] which is given by,

$$\mu = \frac{R_B}{R_x}$$

For halide perovskite, octahedral factor varies between $0.44 < \mu < 0.90$ [126,127].

The vast and captivating range of phase transitions observed in perovskites is of such significance that it forms a distinct and fascinating area of research in the field of physics. It is widely recognized that inorganic perovskites exhibit four primary phases: a room-temperature non-perovskite yellow phase (δ), and three high-temperature phases with cubic or black (α), tetragonal black (β), and orthorhombic black (γ) structures. At ambient temperature, all-inorganic $CsPbX_3$ will quickly transforms from its cubic structure to an orthorhombic one. For example, at cooling temperatures ranging from 360 °C to 25 °C, the structure of $CsPbI_3$ undergoes a series of transformations. Initially, it exists in the black cubic phase, then transitions to the black tetragonal β-phase at 260 °C, followed by the black orthorhombic γ-phase at 175 °C. Finally, upon cooling to room temperature, it assumes the yellow orthogonal δ-phase. In summary, $CsPbI_3$ exhibits a progression from different black perovskite phases (α, β, or γ) to a yellow non perovskite phase (δ) when it reaches room temperature [128].

The dominant phase stability of inorganic perovskites at room temperature is strongly influenced by their size. For instance, bulk $CsPbI_3$ perovskite tends to adopt a stable tetragonal phase at room temperature, but it can undergo a phase transition to a non-perovskite orthorhombic phase due to its low formation energy. However, when $CsPbI_3$ is reduced to QD scale, the surface energy and total Gibbs free energy of the non-perovskite orthorhombic phase become more significant, thus impeding the unfavourable phase transition. Consequently, the cubic and tetragonal phases of $CsPbI_3$ QDs are more thermodynamically favourable than the non-perovskite orthorhombic phase, which is less conducive to solar energy conversion. External conditions can also trigger phase transformations. Highly metastable cubic $CsPbI_3$ QDs can convert to the stable non-perovskite orthorhombic phase when extra polar additives are introduced to remove surface ligands, resulting in the loss of strong-emitting properties. Similarly, $CsPbBr_3$ and $CsPbCl_3$ QDs undergo phase transformations at elevated temperatures [121,129–134].

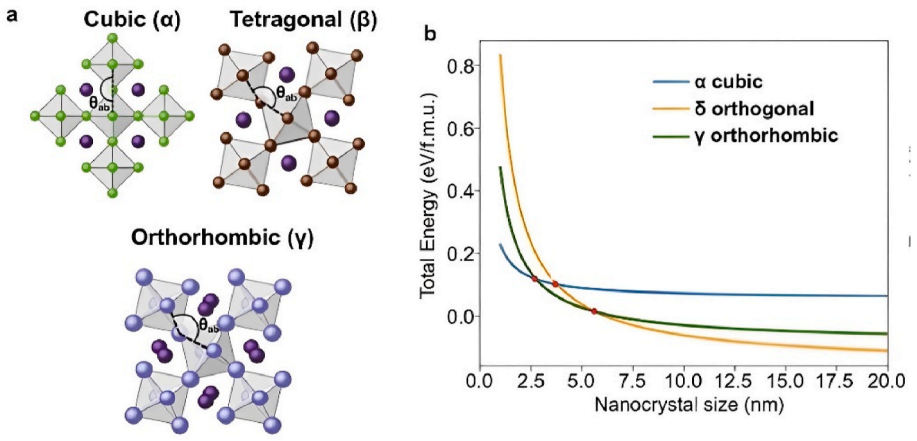


**Fig. 2.** a) Different phases of $CsPbX_3$ perovskites b) Size-dependent formation energy of the α, γ, and δ -phases of $CsPbI_3$ adapted with open access from Ref. [119].

According to reports, the phases of $CsPbI_3$, $CsPbI_2Br$, and $CsPbBr_3$ transition at temperatures of 310 °C [135,136], 230 °C [137], and 130 °C [135,138] from yellow phase to black phase, orthorhombic phase to cubic phase, tetragonal phase to "orange" cubic phase respectively [137]. The reason for the undesired phase transition of $CsPbI_3$ at room temperature is attributed to the inadequate size of the cesium cation, which is unable to sufficiently support the three-dimensional framework of $PbI_6$ octahedra within the cubic perovskite structure. Recent research has demonstrated that the introduction of a smaller bromine anion, through partial substitution of the iodine anion, can effectively stabilize the perovskite phase or black phase in $CsPbI_3$ [135–137]. Furthermore, it has been found that the tolerance factor of cubic $CsPbBr_3$ is 0.814, slightly larger than that of $CsPbI_3$, indicating that $CsPbBr_3$ is more stable than $CsPbI_3$ in an air atmosphere [139–141]. In a study by Nanjing University of Science and Technology China, it was demonstrated that partial substitution of the B-site of the perovskite with $Bi^{3+}$ ions can also stabilize the α -$CsPbI_3$ phase at room temperature. By substituting $Pb^{2+}$ with $Bi^{3+}$, which has a smaller radius, the tolerance factor of $CsPbI_3$ can be increased from 0.81 (for α -$CsPbI_3$) to 0.84 (for α -$CsPb_{1-x}Bi_xI_3$), thereby improving the stability of $CsPbI_3$ [142].

## 3. Synthesis approaches

In a comprehensive review by Manna et al. [143], a thorough exploration of synthesis methods, post-synthesis treatments, and optical properties of metal halide perovskite NCs was conducted. The authors outlined a number of pressing problems that still need to be addressed. This review offers important insights for researchers and substantially advances our understanding of $CsPbX_3$ quantum dot synthesis. These $CsPbX_3$ QDs are synthesized using various methods such as Hot injection (HI) method, ultra-sonication, room temperature precipitation, ion exchange technique and mechanochemical synthesis. The comparison of these widely used synthesis methods are summarized in Table 1.

### 3.1. Hot injection (HI) method

The first method employed in the colloidal production of CdSe QDs was the Hot injection technique, which has since been widely used to synthesize a variety of colloidal nanoparticles/QDs [144]. Later by modifying this method, colloidal PQDs are prepared in a supersaturated solution by quickly injecting the precursors at a high temperature. Protesescu et al. [15] reported synthesis of $CsPbX_3$ QDs by HI method at first. In this procedure, $Cs_2CO_3$ is placed in a 100 ml 3-neck flask with octadecene (ODE) and oleic acid (OA), dried at 120 °C for an hour, then heated to 150 °C under $N_2$ until the reaction is finished. When Cs oleate was preheated to 100 °C before injection, it precipitated from ODE at room temperature. ODE and $PbX_2$ were poured into a 25 ml 3-neck flask and dried under vacuum for 1 h at 120 °C to create $CsPbX_3$. Then dried oleyl amine (OLA) and dried OA. were injected at 120 °C under $N_2$. The temperature was increased to 140 °C-200 °C, and a small quantity of Cs-oleate prepared in the first step was swiftly injected after dissolving $PbX_2$ salt. After 5 s, the reaction mixture was cooled on an ice-water bath. Finally, tert-butanol was added to the crude solution, and it was centrifuged and re-dispersed in toluene or hexane. In this technique, the nucleation stage begins immediately after the injection of nuclei, and the growth stage follows its conclusion. This separation between the two

**Table 1**
Comparison of the existing, widely used synthesis methods of $CsPbX_3$ Q.

| Method | Principle | Advantages | Disadvantages | Reference |
|---|---|---|---|---|
| HI method | High temperature | Uniform size and shape, High crystallinity | Complex process | [16] |
| Ultrasonication assisted method | Ultrasonic treatment | Excellent control of the size of QD by reaction time, suitable for ligand modification. | Large wastage of product during separation and purification. High cost | [17] |
| Ligand assisted reprecipitation method | Rapid nucleation and crystal growth under the control of ligands due to the reprecipitation by mixing solvents with different polarities. | Room-temperature synthesis. Short reaction time. | Large amount of solvent required Complex preparation and purification process. Not suitable for mass production. Low crystallinity and stability | [18] |
| Supersaturated recrystallization method | Mixing solvents with different solubility | Easy operation, room temperature synthesis, suitable for ligand modification | Uneven size | [19] |
| Mechanochemical synthesis | Grinding | simple, high yield, environmentally friendly, solvent-free suitable for the mass production | Causes defects on the surface, not applicable to ligand modification | [20] |
| Wet ball milling | Mixed grinding with solvents | Easy synthesis | Low efficiency | [21] |
| Dry ball milling | solvent-free mixed grinding, | High purity, Fast | High surface defects | [22] |

stages enables the nanocrystals to have a restricted size distribution.

Yuan et al. [27] prepared $CsPbI_3$ QDs by HI method for investigating the stability, degradation mechanism and blinking behaviour of the QDs under different experimental conditions for their practical use in opto-electronic devices. Park et al. [145] also synthesized $CsPbX_3$ QDs of different compositions ($CsPbBr_3$, $CsPbI_3$, and $CsPbBr_xI_{3-x}$ with x = 1.3 and 1.5) via HI method with some modifications. The obtained QDs had cubic shape with mean sizes from 9.3 to 11.2 nm and a size dispersion of 8–10 %. Song et al. [146] reported the synthesis of high-quality $CsPbX_3$ QDs of average diameter 8 nm with a cubic shape by hot-injecting Cesium stearate (CsSt) to $PbBr_2$ solution at 170 °C (Fig. 4). Due to the rapid nucleation and growth kinetics, the involved ionic metathesis reaction only lasts a few seconds. Yu et al. [30] successfully synthesized high-quality, green-emitting $CsPbBr_3$ QDs via HI method (Fig. 4). The synthesis conditions are improved by experimenting with various injection temperatures. Under optimal conditions, high brightness with photoluminescence quantum yield (PLQY) up to 90 % and a small size distribution with a FWHM of 18.5 nm are obtained.

Yan et al. [147] suggested a modified HI method to create $CsPbBr_3$ QDs with excellent stability and effective emission by substituting the traditional oleic acid (OA) ligand with 2-hexyldecanoic acid (DA) (Fig. 3c). The modified QDs demonstrate exceptional stability against ethanol and water as well as a high PLQY of 96 % due to the substantial binding energy between the DA ligand and QDs. Thus, red AgInZnS QDs and $CsPbBr_3$ QDs are combined to create warm white light-emitting diodes (WLEDs) on blue-emitting InGaN chips. Hassanabadi et al. [148] synthesized ultra-stable $CsPbI_3$ QDs for over 15 months by controlling two major factors: synthesis temperature and capping ligand concentration. By increasing the concentration of capping ligands during the synthesis, the researchers were able to grow $CsPbI_3$ QDs in a wide range of temperatures, which improved the photophysical properties of the QDs by increasing the synthesis temperature. The highest photoluminescence quantum yield (PLQY) of 93 % was achieved for a synthesis conducted at 185 °C, which facilitated an efficient surface passivation to reduce the density of non-radiative recombination sites. With these optimized synthesis conditions, they were able to produce deep red LEDs with an External Quantum Efficiency (EQE) greater than 6 %, surpassing the performance of reported $CsPbI_3$ QD-LEDs with standard capping agents, without additional elements or further element exchange. N Pradhan et al. [149] reported a novel synthetic approach for the production of highly stable cubic $CsPbX_3$ QDs by utilizing molecular bromine ($Br_2$) as an independent halide precursor. The distinctive feature of this synthesis lies in the temperature-controlled in situ generation of oleyl ammonium halide species from molecular halogen and amine, resulting in unprecedented long-term stability, emission tunability, and desirable optical properties of the perovskite QDs (see Fig. 4).

HI approach often uses lengthy insulating ligands like OA and OLA, which have a restriction on the device's performance. They reduce the stability and photoluminescence of QDs while lowering their electrical conductivity. In order to get around these problems, Lu et al. [58] reported synthesis of $CsPbI_3$ QD by introducing octylphosphonic acid (OPA) as ligand, which has a shorter carbon chain. On the one hand, the removal of long chain ligands improved the electrical conductivity of QDs. On the other hand, because OPA accelerates the nucleation and growth stages of PQDs and was able to successfully passivate the surface defects caused by undercoordinated Pb atoms on the surface of $CsPbI_3$ QDs, the PL QY and colloidal stability of QDs were also improved. In order to create LEDs, these OPA-capped $CsPbI_3$ QDs with high PLQY of 98 % were employed as emitters. The HI approach has the unique advantage that the high reaction temperature allows for greater control of the QDs form and higher phase purity. Desirable QDs with superior mono dispersity and optical characteristics can be produced by adjusting the operation temperature. The requirement for rapid injection and subsequent fast cooling, which may not be appropriate for large-scale synthesis, is the key disadvantage. The reaction must take place in an

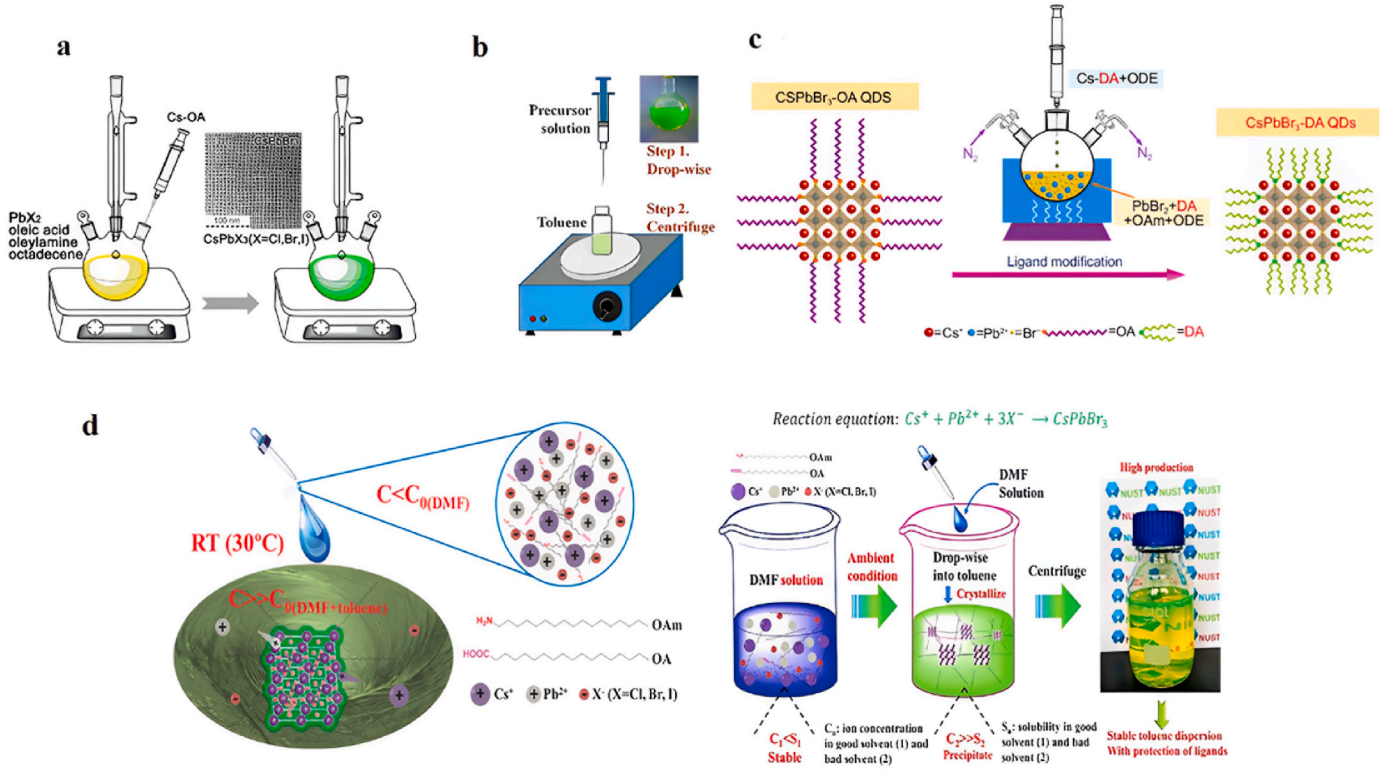


**Fig. 3.** Schematic representation of the a) hot-injection technique b) Ligand assisted re-precipitation technique. c) The schematic illustration of the surface in the $CsPbBr_3$ QDs with ligand modification process d) supersaturated recrystallization method for the synthesis of $CsPbX_3$ QDs/Nanocrystals Adapted with Open Access from Refs. [147,150,151].

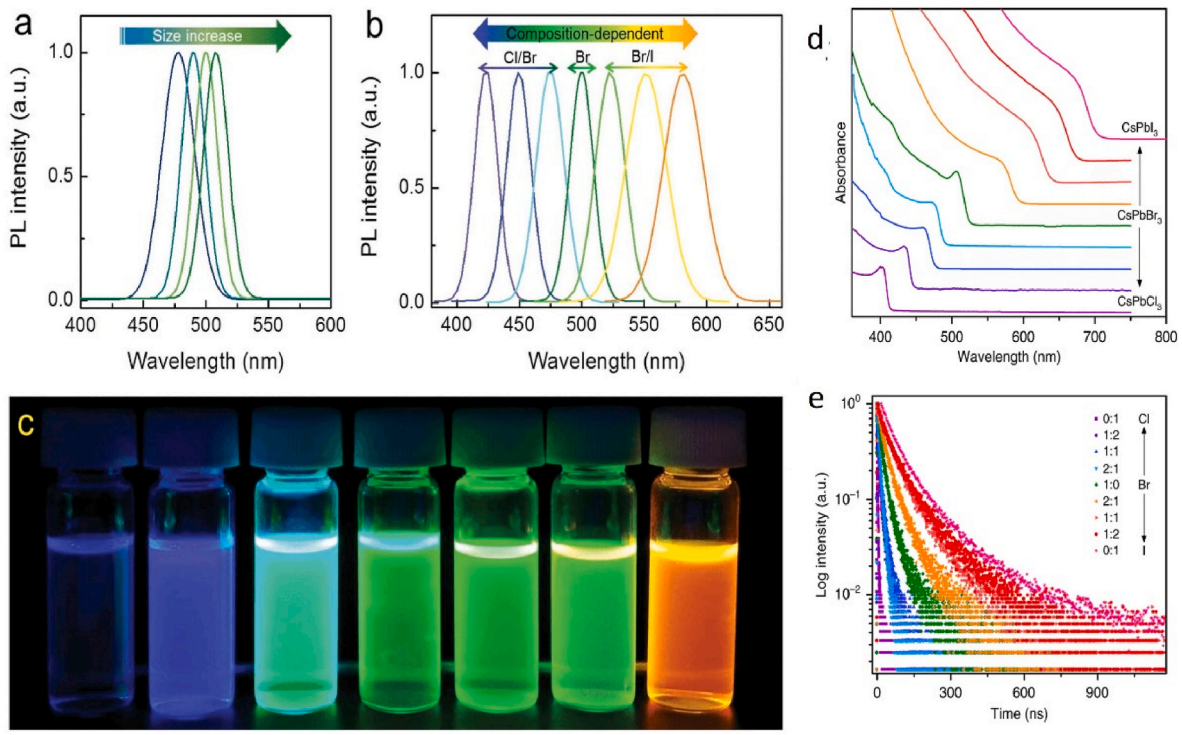


**Fig. 4.** a) PL spectra of perovskite $CsPbBr_3$ QDs with size dependence. The controlled sizes of PQDs were achieved by varying the reaction temperature, which was set to 140, 155, 170, and 185 °C, respectively b) PL spectra of composition-tunable $CsPbBr_3$ QDs with the addition of halides c) Sample of perovskite $CsPbX_3$ QDs synthesized by HI method Adapted with Open Access from Ref. [146] d) PL emission spectra and e) Decay emission curve of $CsPbX_3$ QDs with varied halide composition reproduced from Ref. [152] *CC BY 4.0*.

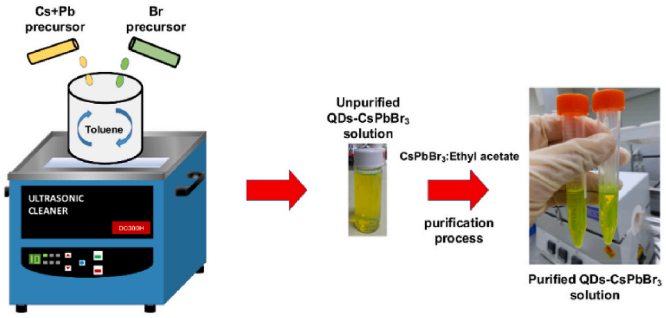


**Fig. 5.** Synthesis of $CsPbBr_3$ QDs by ultrasonic oscillation process Adapted with Open Access from Ref. [31].

inert environment to prevent oxidation [153].

### 3.2. Ultrasonication-assisted method

Xu et al. [154] reported the synthesis of blue emitting $CsPbBr_3$ quantum dots by simple and scalable ultrasonication-assisted method that combining reprecipitation technology with post synthetic strategy, including ultrasonication and hydrobromic acid (HBr) treatment under ambient air conditions without the need for inert gas protection. In the synthesis process, OA and OLA were used as capping ligands. By adding HBr to $CsPbBr_3$ QDs, a halide-rich environment is created, partially filling Br vacancies, which is helpful for acquiring minimal surface defects, achieving defect passivation, stabilizing crystal structures, and enhancing PLQY. $H^+$ cations take part in the development of new hybrid structures with a dynamic balance of QDs at the same time. Several scientists discovered that by incorporating a little quantity of HBr or Hydriodic acid into the perovskite precursor solution, homogeneous and continuous films can be created. Tien and his research group [31] were prepared high-quality perovskite $CsPbBr_3$ QDs using the ultrasonic oscillation method as the emission layer of the quantum dot LEDs. The composition of the emission spectra of the QDs are modified using the halide anion exchange approach and quantum size effects, which allows for tuning of the emission wavelength throughout a significant portion of the visible spectral range (450–650 nm). The purified $CsPbBr_3$ QDs film exhibited a prominent peak of high intensity at the *(200)* lattice plane, indicated the formation of an orthorhombic perovskite crystal structure with the *Pnma* space group. The QDs-$CsPbBr_3$ also exhibited high quantum yields of up to 99.2 %, a narrow line-width emission of 20 nm, and a radiative lifetime of up to 26 ns, which makes them suitable for various applications [155–157]. The authors suggest that the good properties of $CsPbBr_3$ QDs make them ideal for use as an active layer in perovskite QDLED (Quantum Light Emitting Diode) structures. The high quantum yields, narrow emission spectrum, and long radiative lifetime of the QDs can lead to efficient and high-quality QDLEDs. The ultrasonication process promotes the formation of nuclei and the growth of the $CsPbBr_3$ quantum dots. The size and morphology of the quantum dots can be controlled by adjusting the reaction time and temperature, as well as the concentration of the precursors and solvents.

### 3.3. Ligand-assisted reprecipitation

Recently, the Ligand-assisted Reprecipitation (LARP) has been proposed as a possible alternative because, despite its simple process, it can produce fine colloidal PQDs with high luminous quantum yield (Fig. 3 b). In LARP, the precursors are injected into a poor solvent after being dissolved in a good solvent to create the colloidal QDs. Because of the reprecipitation effect, this causes fast crystal nucleation and growth. By controlling the reaction temperature and employing the proper capping ligands, such as octanoic acid, oleic acid, octylamine, and oleylamine, the rate of nucleation and development can be managed. Often used to control crystal formation is a mixture of carboxylic acid and alkyl amine, but because of proton exchange between the ligands, there is a chance of

detachment. Because to the tiny amount of polar solvent in the precursor solution, the crystal formation of QDs is subject to complex processes like Ostwald ripening, aggregation, and/or fusion mechanisms after ligand detachment. As a result, more optimization is required to choose the right ligands and get rid of the polar solvent following synthesis [58,148,149,153]. Oshita et al. [158] used didodecyl dimethyl ammonium bromide (DDAB) as an aprotic ligand during simple LARP method for synthesizing $CsPbBr_3$ PQDs with narrow bandwidth, size control, and deep-blue emission. The DDAB has so far been applied as a posttreatment agent to stop PQD aggregation brought on by ligand exchange during solution aging. However even as the crystals grow, there is aggregation/fusion, which reduces the stability and colour-tunability of the colloidal QDs. To do this, DDAB was added to this contribution's weak solvents before the injection of the precursor solution. Despite this straightforward change, under ambient lighting circumstances, blue-emitting quantum-confined $CsPbBr_3$ QDs with a small bandwidth (20.5 nm) have been obtained. Additionally, they confirmed that the stability of the colloidal QDs in a liquid phase is greatly improved by using gel permeation chromatography (GPC) to remove more than 70 % of the polar solvents.

### 3.4. Supersaturated recrystallization (SR) method

Supersaturated recrystallization (SR), or the activation of a soluble system's constrained sustentative nonequilibrium state by an accident, such as stirring or an impurity, causes the supersaturated ions to precipitate as crystals. This phenomenon is frequently seen in natural minerals, alloys, and ion solutions. The system won't return to equilibrium until this spontaneous precipitation and crystallization reactions end. By considering the ionic crystal characteristics of halide perovskites, the above SR technique can be used to produce QDs in solutions with controlled well size and composition. This technique involves the process of mixing solvents with distinct polarities. It entails transferring $Cs^+$, $Pb^{2+}$, and $Br^-$ ions from soluble solvents to insoluble solvents, resulting in an ion transfer that leads to a supersaturated state. This supersaturated state enables the formation of $CsPbBr_3$ perovskite crystals in the presence of ligands. Hence it appears to be similar to solarizing seawater to produce edible salt, which has been utilized for a long time in human history when supersaturation-induced recrystallization and no use of heating are taken into account. The room-temperature (RT) synthesis of PQDs, their superior PL, their underlying origins, and their prospective applications in lighting and displays are all reported for the first time by Kolalenko et al. [19] which finished within a few seconds through transferring the $Cs^+$, $Pb^{2+}$, and $X^-$ ions from soluble to insoluble solvents. Dimethylformamide (DMF) was dissolved at room temperature with OAm and OA as surface ligands and $PbX_2$ and CsX as ion sources to act as precursors. A significant amount of perovskite crystals was precipitated after the precursor was added to the toluene solution in a supersaturated state. With PLQY values of 80 %, 95 %, and 70 % and FWHM values of 35 nm, 20 nm, and 18 nm for red, green, and blue, respectively, the resultant perovskite displayed good optical characteristics. In this technique, ligands work to passivate the QD's surface to minimize surface flaws and to prevent nonradiative recombination to enhance luminous performance and longevity. Also, it is easy to use without a high temperature or an environment with inert gas, and it is less impacted by the Emissions covering the entire visible region is obtained via fine controlling of com-position and particle size. Excellent photoluminescence with narrow line-widths, high QY and high photo stability are achieved, which are comparable with that synthesized by HI method. Detailed investigations about the influences of surface states and crystal structures on optical properties were made. The exciton binding energies are calculated to be 40 MeV and 44 MeV for $CsPbBr_3$ QDs with monoclinic phase and cubic phase, which are appropriate for the stimulated emission at RT. The Br rich surface states endow $CsPbBr_3$ QDs with interesting anion exchange reactions, self-passivating, and self-soldering behaviours. Finally, due to the outstanding optical properties, WLED with pure white colour and high stability is fabricated. Shu et al. [33] in 2021 synthesized Highly efficient and blue-emitting $CsPbBr_3$ quantum dots by two step SR technique. A substantial quantum confinement effect was produced by the products because the size of the QDs was tightly controlled to be within 2.8 nm. The optical capabilities of the as-synthesized $CsPbBr_3$ QDs included the longest PL lifetime of 12.24 ns and the highest PLQY of 87.20 %. The LED highlighted how well the $CsPbBr_3$ QD's blue optical characteristics worked. It was important to note that the two-step approach was essential for the development of the blue-emitting $CsPbBr_3$ QDs. The entire synthesis is suitable for large-scale synthesis and may be completed under ambient settings, which is significant for both theoretical research and practical applications of this class of blue-emitting materials.

Toluene is frequently employed as the anti-solvent in the SR method, which typically uses DMF or dimethyl-sulfoxide (DMSO) as the solvents. As we know, Toluene which is toxic, difficult to recycle, and leads to the production of QDs with varying properties. Additionally, toluene is used for long-term storage and purification of QDs, but it causes QD degradation. To address these issues, Gao et al. [26] proposed para-xylene as a new anti-solvent for synthesizing $CsPbBr_3$ QDs using the SR method. They found that the as-synthesized QDs were stable, highly photoluminescent, and well-dispersed in para-xylene. The QDs in para-xylene were more stable than those in other anti-solvents such as toluene and ethyl acetate. The high freezing point of para-xylene allowed for long-term storage of the QDs in the refrigerator. The QD's maximum photoluminescence emission intensity remained at 90 % of the original value after 60 days of storage under ambient conditions. Later Ma et al. [159] $CsPbBr_3$ QDs were synthesized by using the supersaturated recrystallization process. Synthesized QDs were optimized using HBr and the ideal preparation conditions were investigated. This procedure minimised the QD's surface flaws, enhanced their luminous qualities, and significantly raised the QY of from 45 to 95 %. The factors that affected HBr post-treatment were also investigated. The outcomes demonstrated that 20 °C and 20 μL of HBr were the ideal post-treatment temperatures and HBr amounts. Recently Han et al. [25] prepared $CsPbX_3$ QDs in an ambient atmosphere, by combining solution based on the supersaturated crystallization principle with an ion exchange method. The obtained samples were expressed as $CsPbBr_{1.9}Cl_{1.1}$, $CsPbBr_{2.1}Cl_{0.9}$, $CsPbBr_3$, $CsPbBr_{1.7}I_{1.3}$, and $CsPbB_{0.9}I_{2.1}$ for blue, cyan, green, yellow, and red samples, respectively. The results demonstrated that the pure $CsPbBr_3$'s green emission gradually changed to cyan, blue, yellow, and red depending on the degree of Br–Cl and Br–I ion exchange. As a result, the emission had a wide wavelength range between 472 nm and 638 nm. In terms of shape, the blue to red samples had larger crystals, and all of the as-synthesized quantum dots were spherical and monodisperse.

### 3.5. Mechanosynthesis method

The majority of synthesis methods for the $CsPbX_3$ QDs are laborious and hazardous solution synthesis techniques that require the use of volatile organic solvents, inert gas shielding, and high reaction temperatures which significantly restrict the practical application of synthesis strategies. Mechanosynthesis is a solid-state synthesis technique that can create nanoparticles, metal organic frameworks (MOFs), organohalide perovskites, graphene, black phosphorus (BP), and carbon hybrid materials without having to worry about solubility problems. The mechanochemical approach essentially grinds or mills easily available separate components together to harness the cocrystal formation process. CsX and $PbX_2$ salts (X = Cl, Br, I, or their mixture) can be stoichiometrically ball-milled or ground at room temperature without being first dissolved in solution, making it simple to create $CsPbX_3$ QDs. The initial documentation of this solid-phase synthesis was presented by Jana and colleagues [160]. This method involves a solvent-free and mechanochemical process where CsBr, $PbBr_2$, and n-octylammonium

bromide are ground together using a mortar and pestle at room temperature. Despite the simplicity of the synthetic procedure, the PLQY of the resulting $CsPbBr_3$ QDs are merely 13 %, significantly lower than the PLQY typically achieved through solution-based synthesis methods.

Zhu et al. [161] in 2017 reported synthesis of highly emissive $CsPbX_3$ QDs using a simple, environmentally friendly, solvent-free mechanosynthesis method. To conveniently change their composition, stoichiometric mixtures of raw reagents are mechanically milled or ground. This resulted in a product with a wide range of luminescence tunability, including adjustable wavelength, line width, and PLQY. When photoexcited, the as-prepared QDs showed quick charge-transfer characteristics with molecular electron donors, which is an advantage for charge-transfer-based photocatalytic applications and optoelectronic conversion devices. As a result, the work not only added new tools to the toolbox for making $CsPbX_3$ QDs, but also gave valuable insights into their exceptional luminescent capabilities and excited-state dynamics.

Protesescu and colleagues [162] introduced a novel wet ball milling method, employing a top-down approach. In this method, $CsPbBr_3$ was initially fabricated and utilized as the starting material. Alternatively, a mixture of CsBr and $PbBr_2$ powder in an equal molar ratio could serve as the precursor for wet ball milling. The halide perovskite bulk crystals or powder precursors were loaded into a zirconia bowl containing 23 zirconia balls, along with mesitylene as the solvent and oleylammonium halide (OAmX) as the ligand. The resulting product exhibited vibrant green luminescence, even under ambient light, indicating the successful formation of halide PQDs through this method. According to Palazon et al. [22], they observed the progression of mechanochemical synthesis of $CsPbBr_3$, using dry ball-milling of precisely balanced precursor materials. They found that there exists an optimal duration for ball-milling (approximately 5 min, specific to their material and ball milling system) in order to obtain high-quality perovskites with a narrow and intense PL emission. Lopez and colleagues [163] conducted a study where they synthesized orthorhombic $CsPbBr_3$ crystals using the mechanochemical method at ambient temperature. They further investigated the structural changes of the crystals at various temperatures.

Through an in situ ball milling method, a series of composites comprising $CsPbBr_3$ QDs and PMMA were successfully prepared by Liu et al. [164]. In this method, the synthesized QDs were encapsulated within a PMMA matrix. The incorporation of PMMA provided significant benefits by enhancing the stability of the quantum dots against heat, humidity, ethanol, and UV irradiation. The optimal mass ratio of the perovskite source in the composite was determined to be 1.5 %. Remarkably, the photoluminescent quantum yield of the 1.5 % $CsPbBr_3$ QDs/PMMA composites reached a high value of 78 %. Consequently, the prepared $CsPbBr_3$ QDs/PMMA composites hold great promise for applications in WLEDs and photocatalysis.

Despite its suitability for mass production of perovskite, the ball-milling method suffers from several drawbacks. One such drawback is that the reaction occurs in the presence of air, leading to potential complications. Additionally, mechanical grinding during the process can introduce numerous surface defects. These surface defects have a detrimental impact on the luminescent properties of the perovskite, highlighting the importance of finding effective solutions to address these challenges [165].

## 4. Morphological properties of $CsPbX_3$ QDs

QD morphology is crucial to understanding their physiochemical characteristics and applications. QDs and Nanocrystals have a very high surface-to-volume ratio due to their small size. Thus, the surface has a big impact on their characteristics. The organic ligands control the shape and surface modification of the QDs. $CsPbX_3$ QDs can achieve high PLQY without further shelling to passivate surface flaws, unlike traditional cadmium-based QDs. High defect tolerance refers to this feature, which indicates that it makes it simple to obtain good optoelectronic qualities because the flaws do not significantly damage or trap the excited carriers. For instance, theoretical studies have demonstrated that the majority of defect energy levels are found within the energy band or close to its margins, but deep energy level-related defects typically need significant formation energy [16,164,165]. The high defect tolerance, meanwhile, has not been observed in all members of the $CsPbX_3$ perovskite family since the defect tolerance of these materials is influenced by a number of variables, including their electrical and crystal structures. For instance, the lattice parameters in the $CsPbX_3$ drop when the halide is changed from I to Br to Cl. Greater interactions between $Pb^{2+}$ dangling bonds are a result of halide vacancies. This action and the reduced electron affinity result in deeper trap levels for the halide vacancy. As a result, $CsPbCl_3$ forms deep traps and is not defect tolerant, in contrast to $CsPbI_3$ and $CsPbBr_3$, which both form shallow traps and have high defect tolerance [153].

Inorganic PQDs exhibit a substantial size-dependent effect as a typical low-dimensional semiconductor quantum system. The quasi-continuous energy level splits and the bandgap widens as the particle size approaches the Bohr radius. Inorganic PQDs can have their bandgap adjusted by changing their size, which increases the wavelengths of their PL emission. According to Butkus et al. the bandgap of $CsPbBr_3$ QDs increases from 2.37 to 2.5 eV when the particle size is reduced from 8.5 to 4.1 nm, which is accompanied with glaring blue shifts in the PL spectra [166]. However, the quantum confinement effect becomes less significant as the size of inorganic PQDs exceeds the Bohr radius [167]. The size and halogen composition of $CsPbX_3$ QDs have a significant impact on carrier transport, spin relaxation, and phonon behaviours. Li et al. [168] conducted a study on $CsPbI_3$ and $CsPbBr_3$ QDs with varying sizes, investigating spin relaxation. Both types of QDs exhibited decreased spin lifetimes as their dimensions reduced. However, when compared to their bulk counterparts, the spin lifetimes of $CsPbI_3$ and $CsPbBr_3$ QDs were prolonged and shortened, respectively. This suggests distinct spin-flip mechanisms between bulk materials and QDs. The Elliott-Yafet (E-Y) phonon scattering mechanism was found to be significant in bulk $CsPbI_3$ but absent in bulk $CsPbBr_3$. In QD form, the suppression of E-Y scattering resulted in a longer spin lifetime for $CsPbI_3$ QDs. Conversely, $CsPbBr_3$ QDs exhibited size-dependent spin relaxation mechanisms, including surface scattering, electron-hole exchange, and spin-spin interaction with surface dangling bond spins, which shortened their spin lifetimes. This size-scaling mechanism highlights the influence of material dimensionality and carrier diffusion on luminescence efficiency and carrier recombination kinetics [169].

Changing the reaction temperature and adjusting the ligand chain lengths are common ways to manipulate the size of PQDs and nanocrystals [170–172]. The size and morphological dimension of PQDs can be altered by the variety of aliphatic carboxylate and amine ligand pairs. The lengths of the acid chains, which range from acetic to oleic acid and hexyl-to oleylamine, have been found to decrease as the size of the nanocube increases (Fig. 6 e). Shorter alkyl-amines and OA, on the other hand, can displace the naturally occurring cubic crystal structure and encourage the 2D formation of nanocrystals, such as nanosheets or nanoplatelets. Nanoplatelet thickness has an amine chain-length dependence. Hexylamine was used by Pan et al. [173] to create the thinnest nanoplatelet, which measured 1.8 nm. The researcher also investigated how surfactant ligands affect the surface properties of colloidal perovskite nanocrystals and the influence of acid and amine compounds, as well as temperature variations, on the size and shape of these nanocrystals. This was achieved by systematically altering the hydrocarbon chain composition of carboxylic acids and amines. (140–180 °C). The reaction medium, including ether solvents like ethylene glycol dibutyl ether (EGDBE), diethylene glycol dibutyl ether (di-EGDBE), and tetraethylene glycol dibutyl ether (tetra-EGDBE), can also have an impact on the nucleation and growth of $CsPbX_3$ Nanocrystals because of their different polarity at various temperatures [174, 175]. Peng et al. [176] reported the development of $CsPbX_3$ into hexapods in four (110) and two (001) directions at 200 °C and above. According to Zhai et al. [177], the thickness of $CsPbBr_3$ nanoplates remains

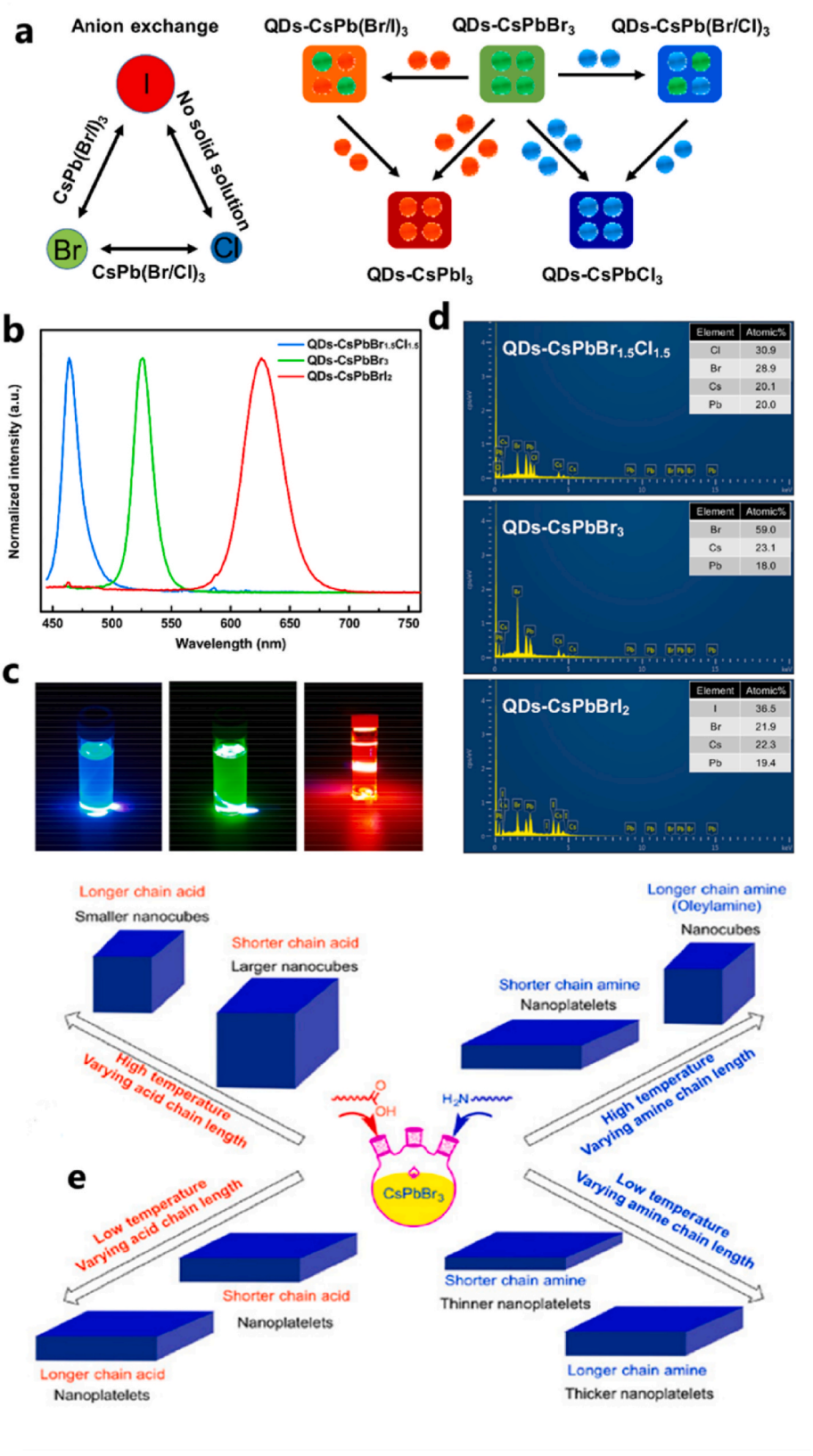


**Fig. 6.** (a) Schematic diagram of the anion exchange between $CsPbX_3$ QDs; (b) the PL emission spectra of $CsPbX_3$ QD solutions; (c) the emission photographs of the solutions of $CsPbX_3$ QDs under UV-405 nm laser excitation; (d) energy dispersive X-ray (EDS) analysis for the purified $CsPbX_3$ QDs. (e) Summary of correlation between the chain length of carboxylic acids and amines and their impact on the size and shape of $CsPbX_3$ materials reproduced with open access from [31,175].

constant at 4.2 nm, which is in the quantum confinement domain, but the lateral sizes may be accurately controlled by changing the solvothermal reaction temperatures and times.

In 2018, Dong and colleagues [178] developed a novel synthesis method that allows for precise tuning of the size of $CsPbX_3$ quantum dots based on thermodynamic equilibrium rather than kinetics. At a constant temperature, the QD size reduced as the Br/Pb ratio increased, showing higher size uniformity at the same time. The QD size shrank with decreasing temperature at a given Br/Pb ratio. It was possible to obtain excellent ensemble homogeneity and precise adjustment of the QD size in the quantum-confined regime by selecting the right combination of these two parameters. Although it is typically challenging to control the size of inorganic nanocrystals through thermodynamic equilibrium, the authors found that the unstable nature of X-in $CsPbX_3$ allowed them to use this approach for size regulation. This discovery has several advantages over conventional methods as it eliminates the need for meticulous control over nucleation and growth kinetics. The method was primarily applied to $CsPbBr_3$, but the authors showed that it could be extended to other $CsPbX_3$ quantum dots, including those with X = Cl, Br, and I. This suggests that the thermodynamic equilibrium approach is a universally applicable strategy for the synthesis of $CsPbX_3$ quantum dots. This unconventional approach has yielded highly uniform quantum dots with minimal exciton luminescence broadening [179,173]. By xu et al. [180–182] a straightforward and quick growth approach for regulating the size of $CsPbBr_3$ QDs by altering the synthesis temperature is reported, and the QD size-dependent photogenerated carrier dynamics is thoroughly investigated. Thus, for the growth of $CsPbX_3$ QDs, size control is still crucial. Moreover, it is important to consider the surface impacts of QDs. Particularly, the QD surface energy exhibits a substantial increase along with the specific surface area and surface binding energy with a decrease in size [175,176].

## 5. Optical properties of $CsPbX_3$ QDs

$CsPbX_3$ QDs have attracted significant attention in the field of optoelectronic devices and related areas due to their exceptional optical properties that distinguish them from other luminescent nanomaterials. These properties include a short radiative lifetime, wide emission spectra, extremely narrow emission bandwidth, high luminescence quantum yield, and precise shape control [177,178,183]. The ability to finely tune the emission wavelengths of $CsPbX_3$ QDs throughout the visible spectrum is facilitated by their compositional versatility. In comparison to conventional Cd-based chalcogenide QDs and other types of QDs, $CsPbX_3$ QDs exhibit outstanding optical characteristics. Their blinking behaviour, characterized by periodic on-off switching of emission, adds to their intrigue. Moreover, $CsPbX_3$ QDs display non-linear absorption and can undergo stimulated emission. These unique optical properties contribute to the fascination surrounding $CsPbX_3$ QDs and their potential applications [184].

While the optical properties of bulk solids remain largely unaffected by crystal size, the behaviour of QDs and nanocrystals deviates from this principle. These materials exhibit size-dependent optical properties owing to the phenomenon of quantum confinement, which can be characterized by the exciton Bohr radius. As a representative example of low-dimensional semiconductor quantum systems, $CsPbX_3$ QDs and nanocrystals showcase intriguing changes in their electronic and optical characteristics when their sizes approach the exciton Bohr radius. When QDs are smaller than their respective exciton Bohr radii, strong quantum confinement effects come into play, leading to significant alterations in their properties. This confinement causes the quasi-continuous energy levels to split, and the bandgap to widen, resulting in distinct optical behaviour. For $CsPbX_3$ QDs, the reported exciton Bohr radii are as follows: 2.5 nm for $CsPbCl_3$, 3.5 nm for $CsPbBr_3$, and 6.0 nm for $CsPbI_3$. These values indicate the critical size at which quantum confinement effects become prominent, influencing the electronic structure and optical response of the QDs. By leveraging the tunability of their size, $CsPbX_3$ QDs offer exciting possibilities for tailoring their properties to meet specific device requirements and enable advancements in optoelectronics [153,181].

$CsPbX_3$ QDs exhibit PL due to direct bandgap transitions or excitonic recombination [7,185]. The intensity of the PL spectrum is influenced by reaction temperature, cleaning, and separation conditions [186]. Higher synthesis temperature results in a red shift, while lower temperature leads to a blue shift in the size and position of the PL spectra. This temperature-insensitive emission characteristic, providing an advantage over traditional metal chalcogenide Nanocrystals and particularly beneficial for applications in LEDs, lasers, and photodetectors [146]. Both inorganic quantum dots and organic materials exhibit size-sensitive emission spectra. In the case of inorganic quantum dots, narrow emission spectra are observed only at sizes below 10 nm. On the other hand, organic materials display broad emission spectra at sizes greater than 10 nm. In contrast, HPs demonstrate very narrow spectra with a FWHM of approximately 20 nm, and this narrowness is independent of their size. Furthermore, the emission spectra of HPs can be tuned across the visible and near-infrared range by controlling their chemical composition, size, or morphology. This unique size insensitivity of emission spectra makes $CsPbX_3$ QDs promising materials for applications such as light-emitting diodes. $CsPbX_3$ QDs and Nanocrystals display stronger photoluminescence emission energy compared to bulk materials, making them promising for optical applications [131, 187–189].

$CsPbX_3$ QDs offer remarkable tunable bandgap energies and colours, making them promising candidates for light emission devices. PL emission spectra can be adjusted from ultraviolet (UV) to near-infrared (NIR) wavelengths by controlling the bandgap through chemical composition and crystallite size tuning. As we mentioned earlier, the HPs have a three-dimensional framework composed of corner-sharing metal halide octahedra, and their electronic levels are determined by hybrid states between metal halide orbitals. The bandgap of HPs can be tuned by mixing and substituting elements within the perovskite structure. The choice of halide elements significantly influences the bandgap and electronic states of HPs. Mixed halide compositions allow for precise control of the bandgap, leading to a wide range of PL emission energies. $CsPbX_3$ Nanocrystals or QDs exhibit tunable PL spectra ranging from 410 nm to 700 nm by adjusting the ratio of halide elements. The emission line-widths are narrow, and high quantum yields are achieved. Similarly, the bandgap of mixed halide HPs can be tuned by varying the ratio of halide elements. This tunability stems from the electronic structure of inorganic PQDs. The upper valence band mainly originates from the $np^6$ orbitals of the X-site anion (n = 3, 4, 5 for Cl, Br, I, respectively) and the $ns^2$ orbitals of the B-site cation (n = 6 for Pb). The lower conduction band is predominantly influenced by the p orbitals of the B-site cation and $np^6$ orbitals of the X-site anion. Consequently, as the halide changes from I ($5p^6$) to Br ($4p^6$) to Cl ($3p^6$), the energy of the X-site $np^6$ orbitals decreases, resulting in an increased valence band maximum. This shift enables the bandgap tunability of inorganic PQDs. Furthermore, modifications at the A- or B-site of halide PQDs can also alter the bandgap [190].

Carrier mobility, diffusion length, and carrier lifetime are crucial factors that determine the optoelectronic properties of material. In the case of PQDs, the carrier mobilities depend on the composition and generally follow a similar trend as observed in polycrystalline thin films. $CsPbI_3$ QDs demonstrate the highest carrier mobility of 20 $cm^2\,V^{-1}\,s^{-1}$, followed by $CsPbBr_3$ (~2.1 $cm^2\,V^{-1}\,s^{-1}$) and $CsPbCl_3$. These trends have been supported by both experimental and theoretical findings. Moreover, $CsPbI_3$ QDs exhibit the longest carrier lifetime of 29 ns, while $CsPbCl_3$ displays the shortest lifetime of 1 ns, as determined through time-resolved photoluminescence (TRPL) measurements. The diffusion length, which depends on carrier mobility and lifetime, can be expressed as $L_D = \sqrt{D_\tau}$, where $D$ represents the diffusion coefficient and $\tau$ represents the carrier lifetime. $CsPbI_3$ QDs also possess the longest diffusion

length due to their high carrier mobility and extended lifetime [125,189,191185,186,190,192–198].

Bi et al. [28] reported the synthesis of mixed-halide $CsPb(XY)_3$ QDs through a simple and efficient method of mixing stock solutions of single-halide $CsPbX_3$ QDs (where X = Cl, Br, and I) at room temperature. By precisely adjusting the ratio of the stock solutions, the cubic crystal structure of mixed-halide $CsPb(XY)_3$ QDs was obtained through anion-exchange and lattice reconstruction processes. These room-temperature synthesized QDs exhibited impressive properties, including bright photoluminescence with tunable emission peaks across the entire visible light spectrum, narrow emission linewidth, and high PLQY. These properties were comparable to QDs prepared using the traditional hot-injection method. Additionally, the researchers fabricated backlight light-emitting diodes (LEDs) using the mixed-halide QDs in conjunction with a commercial 365 nm PL-emitting InGaN chip. These QD-assisted LEDs demonstrated pure and bright emission, along with long-term stability (approximately 3600 h) under an average relative humidity of 60 %.

Su et al. [199] in 2017 synthesized high-quality $CsPbX_3$ and mixed halide $CsPbX_3$ QDs using HI technique. They used double ligands (OA/OAm) instead of the traditional OA/OAm/TOP mixture to improve the optical properties and stability of the PQDs. Unlike previous methods requiring vacuumization or glovebox equipment, their approach allows precise control of the halide atom ratio and achieves PQDs with high quantum yield (40–95 %), narrow emission linewidth (<10 nm), and tunable band gap (408–694 nm) covering the entire visible-light range. The PQDs also exhibited strong photostability, making them promising for applications in photoelectric devices like LEDs and solar cells. The experimental results were supported by theoretical calculations, which indicated that the high quantum yield of the PQDs could be attributed to their direct band gaps and validated the agreement between the theoretical and observed emission peak. Detailed PL information of $CsPbX_3$ QDs synthesised using various methods are summarized in Table 2.

Thermal quenching, the phenomenon wherein the photoluminescence intensity diminishes with an increase in temperature, frequently impedes the practical application of materials. Song et al. [200] investigated thermal quenching effects in $CsPbX_3$ QD films, unveiling a modifiable emission peak spanning 451–636 nm through the variation of halide ion composition. Temperature-dependent photoluminescence spectroscopy demonstrates the impact of thermal quenching on the blue shifting of band gaps and linewidth broadening. The analysis of activation energy (ΔE) and Huang–Rhys factor (S) indicates a correlation between halide composition and the efficiency of non-radiative electron transitions, emphasizing the role of thermal quenching in influencing the optoelectronic properties of these QD films. Recently, Song et al. [201] investigated the thermal quenching of $CsPbX_3$ QDs embedded into mesoporous spherical structures of $ATiO_3$ (A = Ca, Ba, Sr). Their study revealed that the unique mesoporous hollow microsphere structure, particularly in $SrTiO_3$, effectively inhibits thermal quenching by blocking heat transfer, showcasing its potential for enhancing the thermal stability of PQDs.

## 6. Strategies to improve stability and optical properties

### 6.1. Ion doping

The $CsPbX_3$ QDs have excellent optical properties such as high PLQY, low Auger recombination loss, and a large exciton binding energy but their poor stability due to high sensitivity to the external environment limits their commercial application. Implementing stabilization measures inevitably results in a decline in optical performance. Therefore, further investigation is needed to enhance the stability as well as the optical properties of these QDs. This section focuses on strategies aimed at improving the stability and optical performance of PQDs. The primary strategies involve doping engineering, surface ligand modification, and surface coating. Ion-doping replaces certain elements in the perovskite material to enhance stability. A-site doping increases the tolerance factor, while B-site doping with smaller ions substitutes $Pb^{2+}$ and improves phase stability while reducing toxic ions. The addition of surface ligands modifies the surface of QDs, leading to strong binding and reducing non-radiative processes. This enhances the optical performance of the QDs. Coating the QDs with transparent wide-bandgap materials provides protection, reducing degradation and improving

**Table 2**
Detailed PL information including size, emission peak, colour of emission, PLQY and FWHM.

| $CsPbX_3$ QDs | Synthesis Method | Size (nm) | PL Peaks (nm) | Colour of emission | PLQY (%) | FWHM | Ref |
|---|---|---|---|---|---|---|---|
| $CsPbBr_3$ | Modified HI method | 5.5 | ≈490 | green | 95 | 132 | [23] |
| | | 7.3 | ≈520 | green | 90 | 99 | |
| | | 10.1 | 517 | green | 86 | 95 | |
| $CsPbBr_1I_2$ | Conventional and modified HI method | – | 644 | Red | 85 | 34 | [24] |
| $CsPbBr_3$ | | – | 515 | Green | 96 | – | |
| $CsPbBr_{1.3}Cl_{1.7}$ | | – | 463 | Blue | 92 | 17 | |
| $CsPbBr_{1.9}Cl_{1.1}$ | SR technique | 10.66 | 472 | Blue | 7.92 | – | [25] |
| $CsPbBr_{2.1}Cl_{0.9}$ | SR technique | 10.76 | ≈480 | Cyan | 6.72 | – | |
| $CsPbBr_3$ | SR technique | 12.33 | 516 | Green | 53.53 | – | |
| $CsPbBr_{1.7}I_{1.3}$ | SR technique | 12.64 | 575 | Yellow | 2.48 | – | |
| $CsPbBr_{0.9}I_{2.1}$ | SR technique | 22.62 | 638 | Red | 19.86 | – | |
| $CsPbBr_3$ | SR technique | 8.2 | 511 | Green | 78 | 21.2 | [26] |
| $CsPbI_3$ | HI method | 10.9 | 674 | Red | 78 | 33 | [27] |
| $CsPbCl_3$ | HI method | – | 410 | Violet | 7 | 12 | [28] |
| $CsPbBr_{1.5}Cl_{1.5}$ | Post synthesis | – | 467 | Blue | 23 | 14 | |
| | HI | – | 460 | Blue | 30 | 12 | |
| $CsPbBr_3$ | HI method | – | 515 | Green | 93 | 22 | |
| $CsPbBr_{1.5}I_{1.5}$ | Post synthesis | – | 591 | Orange | 70 | 57 | |
| | HI | – | 594 | Orange | 65 | 43 | |
| $CsPbI_3$ | HI method | – | 667 | Red | 83 | 47 | |
| $CsPbBr_3$ | SR technique | 1.1 | 433 | Blue | 74 | 14 | [29] |
| $CsPbBr_3$ | HI method | 14.8 | 517 | Green | 90 | 18.5 | [30] |
| $CsPbBr_3$ | Ultrasonic oscillation method | 13.46 | 526 | Green | 99.2 | 20 | [31] |
| $CsPbBrI_2$ | Ultrasonic oscillation method | – | 626 | Red | – | 38 | |
| $CsPbBr_{1.5}Cl_{1.5}$ | Ultrasonic oscillation method | – | 464 | Blue | – | 19 | |
| $CsPbBr_3$ | LARP Technique | 5 | 513 | Green | 81.4 | 23 | [32] |
| $CsPbBr_3$ | SR technique | 2.8 | 478 | Blue | 87.20 | – | [33] |
| $CsPbBr_3$ | HI method | 8.7 | 501 | Green | – | 27 | [34] |
| $CsPbBr_3$ | HI method | 10.2 | 515 | Green | 92.7 | 19 | [35] |

resistance to water and oxygen. Additionally, this coating helps prevent efficiency reduction caused by aggregation and ion exchange. These modifications significantly improve the stability and photoluminescence quantum yield of PQDs.

Impurity doping has been recognized as a useful technique to alter the structural, optical, and electrical characteristics of $CsPbX_3$ QDs. The $ABX_3$ structure of PQDs consists of three distinct lattice positions, each exerting a different influence on the material. For example, in $CsPbBr_3$, Cs has minimal impact on its electronic structure, while the 4p orbital of Br and the 6p orbital of Pb significantly contribute to the valence and conduction bands, respectively. The excitation and recombination processes occur within an octahedral structure, underscoring its significance for PQD luminescence. Consequently, various ionic doping approaches yield diverse effects on the properties of PQDs [202].

The A-site of $CsPbX_3$ QDs plays a significant role in determining their structure and stability. In terms of the valence distribution within the perovskite lattice, monovalent cations, particularly alkali metals such as $Na^+$ [37], $K^+$ [203], $Rb^+$ [204] and $Li^+$ [204], are commonly employed as A-site dopants. These alkali metals are preferred due to their strong resistance to oxidation, making them ideal candidates for A-site doping. By adjusting the size of the A-site doping elements in perovskite materials, it is possible to apply chemical pressure to the octahedral framework. This pressure induces the tilting of the octahedral structure and displacement of the central cation. As a consequence, distinct optoelectronic properties emerge, giving rise to unique characteristics in the material [205]. The two important fundamental effects are a tunable bandgap and luminescence with adjustable components. In general, depending on the size of the injected cations, A-site doping will slightly widen or narrow the bandgaps. With $CsPbX_3$ as the host, adding larger impurities will reduce the bandgap while adding smaller dopants will raise the bandgap. The initial $CsPbX_3$ nanocrystal's phase structure, which is crucial for the use of photoelectric devices, will not be changed by the partial replacement of Cs by these doping cations [8].

Shi and colleagues [37] investigated the impact of $Na^+$ ion doping on the PL properties and stability of $CsPbBr_3$ QDs. Improved HI synthesis was used to prepare both $CsPbBr_3$ QDs and Na-doped $CsPbBr_3$ QDs (Na: $CsPbBr_3$). $Na^+$ ions replaced $Cs^+$ ions in the $CsPbBr_3$ lattice. Compared to pure $CsPbBr_3$ QDs, the PL efficiency of Na: $CsPbBr_3$ QDs (with a Cs/Na ratio of 1:4) significantly improved, increasing from 52.6 % to 94.2 %. The PL peak and absorption band edge were blue-shifted due to increased $Na^+$ ion doping. Incorporating $Na^+$ ions into the $CsPbBr_3$ lattice resulted in reduced grain size and degradation rate. PL decay plots and radiative recombination rates indicated that the presence of $Na^+$ ions inhibited nonradiative recombination. Stability tests demonstrated that Na: $CsPbBr_3$ QDs maintained high PL intensity even after 30 days under ambient conditions. Furthermore, by performing ion exchange with Cl and I ions, the PL spectra of the QDs could be tuned from blue to red, while maintaining high PLQY, suggesting that $Na^+$ ion-based ion exchange reactions offer an effective approach for both spectral tuning and enhanced stability of $CsPbX_3$ QDs. A straightforward and effective room temperature approach is proposed by Huang and et al. [38] for the synthesis of $Na^+$ ion doped $CsPbBr_3$ QDs, with a thorough investigation into the effects of $Na^+$ doping on their morphology, structure, and optical properties, as well as their performance in final devices. When compared to pure $CsPbBr_3$ QDs, the optimized $Na^+$ doped $CsPbBr_3$ QDs exhibit notable improvements, including a higher PLQY of 94.74 % and a longer lifetime of 31.2 ns? These findings indicate that $Na^+$ doping effectively passivates defects within the $CsPbBr_3$ QDs. Moreover, the resulting QDLED, utilizing $Na^+$ doped $CsPbBr_3$ QDs as the luminescent material, demonstrates impressive performance with a current efficiency of 34.5 cdA-1 and an EQE of 8.97 %. These values are approximately 2.2-fold and 1.8-fold higher, respectively, compared to devices using undoped $CsPbBr_3$ QDs. The results of this study suggest that $Na^+$ doped $CsPbBr_3$ QDs hold promise as a luminescent material for various optoelectronic applications, including QDLEDs. In 2020, Liu et al. [206] made a substantial advancement in the efficient near-infrared emission from Sn–Pb alloyed PQDs ($CsSn_{0.6}Pb_{0.4}I_3$ QDs) by adding $Na^+$ ions. This is the first demonstration of such efficient emission, accompanied by a substantial improvement in PLQY from approximately 0.3 %–28 %. Through X- Ray photon spectroscopy (XPS) analysis, it was observed that $Na^+$ doping has the potential to stabilize $Sn^{2+}$ and $I^-$ ions by enhancing their chemical bonds, thereby suppressing the formation of detrimental trapping states. These findings provide valuable insights into materials design strategies aimed at enhancing the optoelectronic properties of Sn-containing perovskites. In Fig. 9a, the PL spectra of QDs are depicted, both without and with Na doping. The introduction of $Na^+$ ions enhance the band-edge recombination of the QDs, resulting in a significant increase in near-infrared PL emission. As the Na concentration increases, the near-infrared PL emission becomes stronger. When the Na content reaches 0.5 %, the PLQY can reach a value of 28 %. Fig. 9b illustrates the time-resolved photoluminescence (TRPL) spectra, showing that the PL lifetime of Na-doped PQDs is considerably extended compared to non-doped QDs (see Fig. 10).

In order to comprehend the influence of Na ions on $CsSn_{0.6}Pb_{0.4}I_3$ PQDs, specifically their impact on enhanced photoluminescence and subsequent photoluminescence degradation, Jiyang et al. [207] conducted an investigation utilizing first-principles density functional theory (DFT) and molecular dynamics (MD) calculations. Their study focused on evaluating the strength of surface bonds, defect formation energies, and the interaction between surface ligands and perovskite surfaces. In order to partially replace the location of $Cs^+$ ions, Liu and colleagues [203] added $K^+$ ions to the $CsPbCl_3$ lattice. The PLQYs of $CsPbCl_3$ QDs were enhanced from 3.2 % to 10.3 % by varying the $K^+$ ion doping quantity. Zhao et al. [39] effectively modified the lattice of $CsPbCl_3$ QDs by incorporating $Rb^+$ ions, which partially replaced $Cs^+$ ions using a modified HI method. It was intriguing to observe that the PLQY of $CsPbCl_3$ quantum dots significantly improved from 5.7 % to 13 % by optimizing the $Rb^+$ doping concentration. The absorption and emission peaks of the $CsPbCl_3$ quantum dots experienced a blue shift due to the lattice substitution of $Cs^+$ with $Rb^+$. Further investigation into the photoluminescence dynamics revealed that the enhanced PLQY resulted from reduced defects in $CsPbCl_3$: Rb quantum dots. Todorovic and his research group successfully synthesized stable blue-emitting PQDs by incorporating $Rb^+$ ions into the A-site of $CsPbBr_3$ nanocrystals. These materials exhibited impressive PLQYs exceeding 60 % and demonstrated tunable yet stable photoluminescence properties. To further explore their potential applications, they fabricated the first blue-emitting PeLEDs (Perovskite Light-Emitting Diodes) utilizing Rb-doped PQDs. These devices covered a wavelength range from deep-blue (464 nm) to sky-blue (490 nm) and achieved high electroluminescence quantum efficiencies (EQEs) ranging from 0.11 % to 0.87 %, respectively. Importantly, the $Rb_xCs_{1-x}PbBr_3$ PQDs showcased remarkably narrow emission linewidths of 18 nm, demonstrating their high spectral purity. Additionally, these A-site doped QDs exhibited excellent thermal and operational stability, as the occurrence of halide segregation was effectively prevented. Overall, their findings highlighted the potential of A-site doped PQDs, particularly $Rb_xCs_{1-x}PbBr_3$, as promising materials for stable and efficient blue-emitting optoelectronic devices [208].

$Li^+$ doped $CsPbBr_3$ and $CsPbI_3$ QDs were synthesized by Wu et al. [209] in 2021, who also investigated their impact on the nonradiative and radiative recombination processes. Halide vacancies and defects could be passivated by doping with the right concentration of $Li^+$ to minimize nonradiative recombination and enhance phase stability. There are comparatively fewer reports on A-site cation doping when compared to B-site ion doping.

B-site doping has emerged as a highly recognized and effective approach for enhancing the stability and introducing novel optical properties in $CsPbX_3$ PQDs. The intricate relationship between B-site metal dopants and the perovskite host is mostly manifested in the electronic structure and energy band. Due to Pb's critical crystal structure position and irreplaceable electronic structure status, B-site doping

ratios are typically low. Consequently, the optical and electrical characteristics of PQDs can be significantly altered by a small amount of B-site dopants [8]. By adopting the strategy of B-site doping, it becomes possible to reduce the lead content to a certain extent, which holds great importance for PQDs. This strategy not only improves the overall stability of the PQDs but also offers opportunities for exploring and engineering new optical characteristics, thus opening up avenues for their diverse applications in optoelectronics and related fields. $Sn^{2+}$ [210], $Cu^{2+}$ [41], $Zn^{2+}$ [211], $Fe^{2+}$ [46], $Mn^{2+}$ [212], $CO^{2+}$ [213], $Cd^{2+}$ [214], $Sr^{2+}$ [215], $Ni^{2+}$ [89], $Al^{3+}$ [216], $Bi^{3+}$ [217] and lanthanide ions such as $Dy^{3+}$ [218], $Yb^{3+}$ [219], $Pr^{3+}$ [220], $Nd^{3+}$, $Gd^{3+}$, $Ho^{3+}$, $Ce^{3+}$, $Tb^{3+}$, $Eu^{3+}$, $Tm^{3+}$, $Sm^{3+}$ [221] are the commonly used dopants. PQDs provide an excellent platform for facilitating quantum cutting in combination with rare-earth ions. The Mn-doped perovskite stands out among these B-site doping elements due to its efficient bright yellow-orange emission for the white light emission device.

Wu et al. [204] in 2023, employed a strategy to enhance the photophysical properties of $Mn^{2+}$ ion-doped $CsPbCl_3$ PQDs by introducing $Rb^{+}$ ions as dopants during the HI synthesis process. The resulting $CsPbCl_3$: ($Rb^{+}$, $Mn^{2+}$) PQDs exhibited multi-colour emissions, which arose from the combined contribution of the PQD host and the doped $Mn^{2+}$ ions. Notably, the introduction of $Rb^{+}$ ions played a crucial role in modifying the intrinsic defect states and reducing the presence of Mn–Mn or Mn-traps in the co-doped PQDs. Consequently, this led to a substantial enhancement in the PLQYs of $CsPbCl_3$:$Mn^{2+}$ PQDs, increasing from 20.3 % to 71.1 %. Moreover, by utilizing an anion exchange reaction, they achieved white light emission with CIE coordinates of (0.33, 0.29). Jung et al. [32] conducted experimental and theoretical investigations to analyze the impact of substitutional defects on $CsPbBr_3$ QDs. Through ligand-assisted reprecipitation, they introduced trivalent dopants In, Sb, and Bi to create substitutional defects in $CsPbBr_3$. The results showed that increasing the doping concentrations of trivalent metal dopants resulted in a shift of the PL emission peak towards shorter wavelengths. Furthermore, the trivalent metal-doped $CsPbBr_3$ QDs exhibited enhanced PLQY (approximately 10 % improvement) and improved air stability over a 10-day period. The findings provided valuable insights into the influence of substitutional defects on the physical properties of $CsPbBr_3$ QDs, highlighting the positive effect of low dopant concentrations on the photoluminescence quantum yield. Specifically, a doping concentration of 3 mol% In, 3 mol% Sb, and 1 mol % Bi demonstrated the highest efficiency, and QDs with optimal doping concentration showed longer lifetimes and improved stability compared

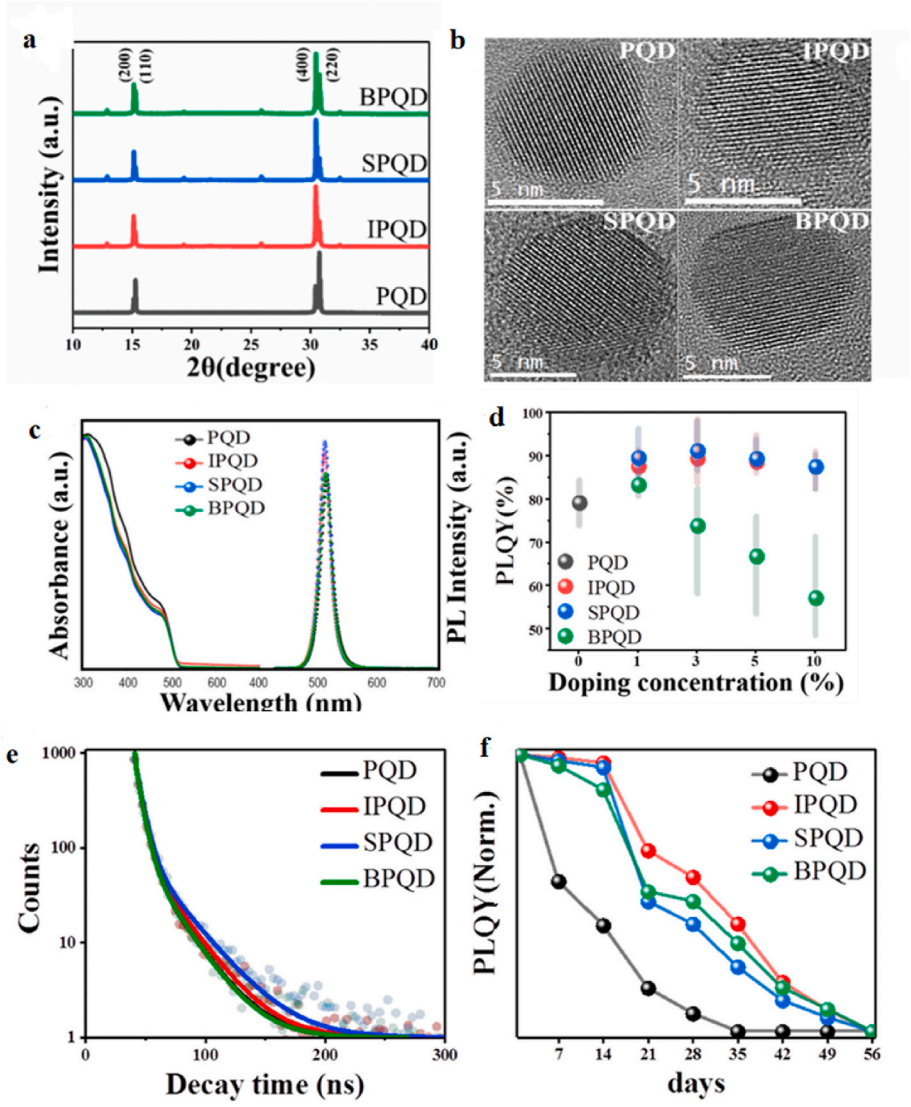


**Fig. 7.** a) X-ray diffraction (XRD) data. b) High-resolution transmission electron microscopy (HR-TEM) image c) Absorbance and PL spectra d) PLQY value averaged from 5 measurements. e) decay curve f) stability of 0 mol% (PQD), 3 mol% In (IPQD), 3 mol% Sb (SPQD), and 1 mol% Bi (BPQD) ion doped $CsPbBr_3$ QDs adapted with open access from Ref. [32].

to non-doped QDs (Fig. 7). The research also confirmed that incorporating trivalent cations reduced the concentration of native donors by elevating the Fermi level, effectively suppressing the vacancy-mediated diffusion process. Chen et al. [212] also reported Mn doped CsPb $(Cl/Br)_3$ Nanocrystals with efficient blue/orange dual emission and it has been shown to be effective as a colour converter in solid-state lighting that is activated by ultraviolet light. The schematic diagram of structure and PL spectra of Mn:$CsPb(Cl_{0.6}Br_{0.4})_3$ nanocrystals, which were synthesized using various ratios of Mn-to-Pb during the feeding process, are presented in Fig. 8a.

In 2022, Ma et al. [159] conducted a systematic investigation on the structural stabilities of Mn-doped $CsPbCl_3$ PQDs at different doping concentrations. Their findings revealed that Mn: $CsPbCl_3$ PQDs exhibit intrinsic stability when the doping concentration is below 25 % or within the range of 40–50 %. However, when the Mn doping concentration falls between 25 and 40 %, the Mn: $CsPbCl_3$ PQDs demonstrated instability. To overcome this issue, they utilized $CsPb_{0.796}Mn_{0.204}Cl_3$ PQDs, which exhibit good stability, to undergo anion exchange reactions with $CsPbBr_3$ PQDs. This process resulted in a wide colour gamut, spanning from blue to orange. Subsequently, they incorporated the Mn: $CsPb(Cl/Br)_3$ PQDs into a polymethyl methacrylate (PMMA) matrix to create colour converters for blue, green, and orange LEDs. These converters were then combined with UV-emitting InGaN chips to fabricate multicolour-emitting LEDs, allowing for a diverse range of colours in the emitted light. In the same year, Room temperature solution-processed doping of $Nd^{3+}$ ions into $CsPbBr_3$ PQDs by W. Duan yielded mixed-cation all-inorganic PQDs with controlled doping ratios [222].

To enhance the PQD's thermal stability and optical characteristics, Bi et al. [41] doped $Cu^{2+}$ ions into them. The produced PQDs demonstrated deep blue PL at 450–460 nm, with a quantum yield of more than 80 % and remarkable thermal stability (Fig. 8 b). In order to effectively facilitate the energy transfer of exciton from the QD core to the $Mn^{2+}$ doped level, Luo et al. [48] synthesized doped $CsPbBr_{2.2}Cl_{0.8}$ QDs with the addition of $Tm^{3+}$ and $Mn^{2+}$. They did this by introducing the $^1G_4$ level of Tm between the conduction band of the QD and the $^4T_1$ level of Mn (Fig. 8c).

The addition of rare-earth ions did not significantly affect the QD's morphology, which remained cubic in shape across all samples. Spectral tuning was achieved by adjusting the rare-earth ion doping levels in the PQDs. The photoluminescence peak shifted towards the blue region, from 515 to 500 nm, while the FWHM remained relatively stable. These changes were primarily attributed to the smaller size of Nd ions compared to Pb ions, resulting in a reduction in lattice constant and an

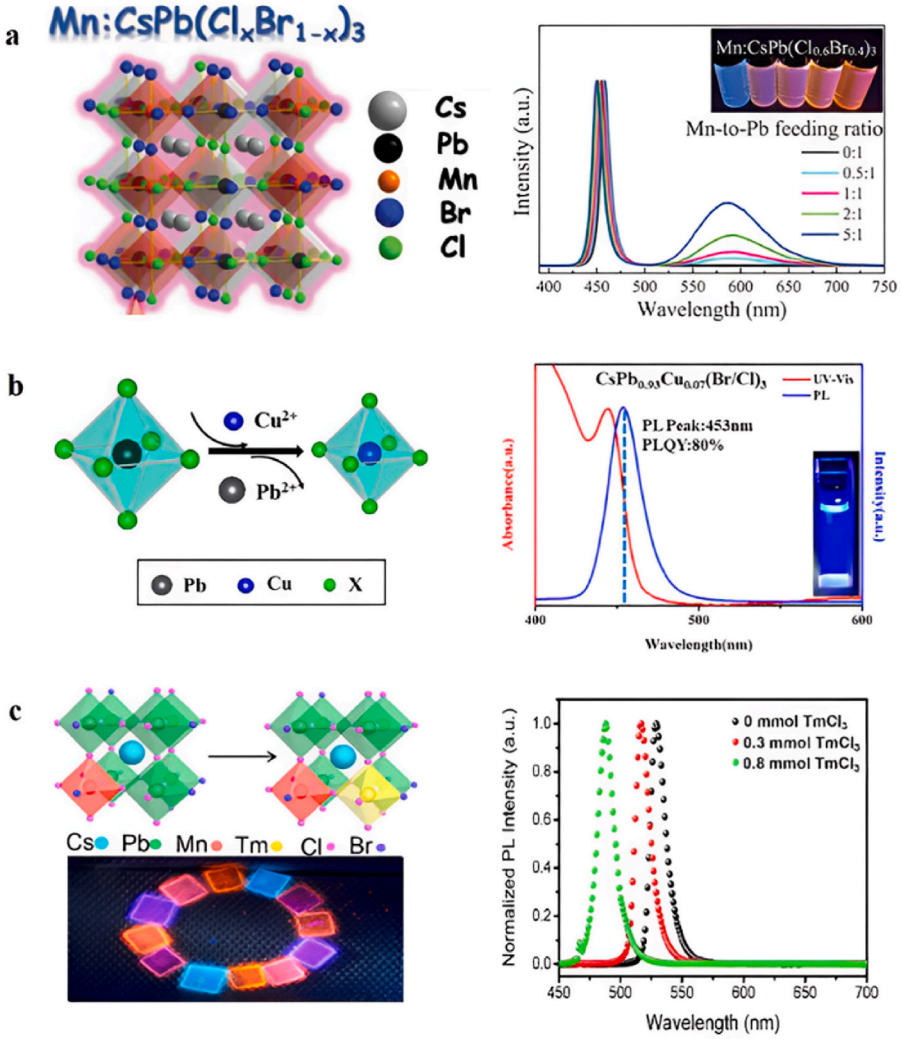


**Fig. 8.** a) $Mn^{2+}$ doping in to $CsPb(C_{0.6}Br_{0.4})_3$ and PL spectra with various Mn-to-Pb feeding ratios. Luminescent photographs of Mn:$CsPb(Cl_{0.6}Br_{0.4})_3$ Nanocrystals in solution under irradiation of 365 nm UV lamp is given in inset. (b) Doping Schematic diagram illustrating the possible mechanism of the formation of $Cu^{2+}$ doped $CsPbX_3$ QDs ($CsPb_{1-x}Cu_xX_3$). Incorporation of smaller divalent $Cu^{2+}$ cations result in contraction of the octahedra. (c) Crystal structure and multicolour films under 365 nm ultraviolet lamp of $Tm^{3+}$ doped $CsPbBr_xCl_{3-x}$ QDs. Adapted from Ref. [118].

increase in the band gap width. The performance of LEDs based on $Nd^{3+}$doped $CsPbBr_3$ QDs was investigated, revealing diminished performance with excessive $Nd^{3+}$ doping. The introduction of rare-earth ions could lead to impurities and foreign phases, which may increase the presence of halogen vacancies (VBr) in the QDs. These vacancies can act as quenching centers, promoting nonradiative energy transfer to trap states and consequently leading to suboptimal performance in perovskite LEDs.

Recently, $Eu^{3+}$doped $CsPbCl_3$ QDs were successfully synthesized by wang et al. [42], using an improved HI technique. This method resulted in QDs with a low $Pb^{2+}$ content and high thermal stability. The introduction of $Eu^{3+}$ not only reduced the toxicity but also maintained the tetragonal crystal structure of the $CsPbCl_3$ host. Under room temperature excitation at 380 nm, the doped QDs exhibited four distinct emission peaks: a main emission at approximately 425 nm (band emission), $Eu^{3+}$ emissions at around 590 nm ($^5D_0 \rightarrow {}^7F_1$ transition), 615 nm ($^5D_0 \rightarrow {}^7F_2$ transition), and 695 nm ($^5D_0 \rightarrow {}^7F_4$ transition). The experimental results demonstrated energy transfer between the $CsPbCl_3$ matrix and $Eu^{3+}$ dopants, allowing for adjustable relative photoluminescence intensity and emission positions of $Eu^{3+}$. Additionally, doping $Eu^{3+}$ ions improved the activation energy, indicating enhanced thermal stability of the $Cs(Pb_{1-x}Eu_x)Cl_3$ PQDs. These successfully doped QDs possess excellent optical properties, paving the way for their future practical applications and the summary of the device performance is given in Table 3.

### 6.2. Surface ligand modification

Exciton recombination is the mechanism by which PQDs produce fluorescence. However, the high surface-volume ratio inherent to PQDs leads to numerous atomic dangling bonds and significant surface defects. These defects act as traps for electrons from the conduction band, resulting in nonradiative recombination and a decrease in PLQY. To address this issue, during the synthesis of QDs, ligands can be added to form bonds with uncoordinated lead and halogen ions present on the surfaces of the QDs. This process helps to reduce surface defects and enhances the PL intensity and stability of the QDs. Ligand modification is widely employed to enhance the photoelectric performance of PQDs. The role of surface ligands is critical in QD synthesis, surface passivation, colloidal stability, and regulation of optoelectronic characteristics [118,223].

In 2015, Kovalenko and colleagues [15] introduced the use of OA and OAm ligands in the synthesis of PQDs. However, these ligands exhibited weak binding to the surface of PQDs, leading to uncontrolled growth and inadequate stability during purification and operation. Moreover, the OA and OAm ligands were susceptible to detachment from the PQD surface after proton exchange, resulting in the degradation of optical properties and colour stability [224]. Furthermore, the insulating nature of long-chain organic ligands hindered charge transmission, limiting the conductivity and practical applications of PQDs, especially in the display field. Therefore, finding suitable ligands to replace long-chain organic ligands is crucial to ensure stability and enhance the potential applications of PQDs [225].

Ligand alternatives commonly used can be categorized into three types based on their covalent bonding: Lewis acids, Lewis bases, and multidentate ligands. The flaws on the surfaces of the $CsPbX_3$ QDs can be removed by the Lewis base by providing a pair of non-bonding electrons to form a bond with $Pb^{2+}$ where the uncoordinated halides on QD surfaces can form bonds with Lewis acids, reducing the surface defect state of $CsPbX_3$ QDs [226]. Trioctylphosphine oxide (TOPO), and diphenylphosphane (DPP) are examples of Lewis bases. Dodecyl benzene sulfonic acid (DBSA), trioctylphosphine (TOP), tributylphosphine (TBP) are examples of lewis acids. At least two coordinating atoms make up multidentate ligands, which have a higher affinity for $CsPbX_3$ QDs. Polyethyleneimine (PEI) is an example for multidentate ligand.

Wu et al. [227] in 2017 demonstrated that the inclusion of TOPO, a highly branched capping ligand, in the conventional OA/OAm system enables the synthesis of monodisperse $CsPbX_3$ QDs with excellent optoelectronic properties at elevated temperatures (up to 260 °C). The addition of TOPO allows for a wide range of QD sizes. Importantly, the incorporation of TOPO significantly enhances the stability of $CsPbX_3$ against ethanol treatment. Af ter 100 min of ethanol treatment, the emission intensity of the TOPO-capped sample only decreases by 5 %, while the non-TOPO-capped Nanocrystals experience a decrease of up to 86 % in emission intensity. Li and co workers [50] developed a straightforward approach to produce highly luminescent and stable $CsPbBr_3$ QDs using a Cs-oleate solution containing organic phosphine ligands such as TOP, DPP, or TBP. The presence of phosphine ligands on the surface of the $CsPbBr_3$ QDs has been confirmed by NMR and XPS spectra. The incorporation of multi-branched phosphine ligands provides steric hindrance, resulting in colloidal QDs that maintain bright PL emission even after four months of storage under ambient conditions. Furthermore, the phosphine-modified $CsPbBr_3$ QDs exhibit enhanced resistance to polar solvents and UV light compared to pristine QDs. Yang

**Table 3**
Summary of the device performance of metal doped $CsPbX_3$ quantum dots.

| Doping | Host | Excitation (nm) | Emission (nm) | FWHM (nm) | PLQY (%) | $\tau$ (ns) | Advantage | Ref |
|---|---|---|---|---|---|---|---|---|
| A- Site doping | | | | | | | | |
| $K^+$ | $CsPbCl_3$ | 365 | 408 | 12.7 | 10.3 | 13.6 | Significant enhancement of quantum efficiency and luminescence intensity | [36] |
| $Na^+$ | $CsPbBr_3$ | 480 | 514 | 20.1 | 94.2 | 32.2 | $CsPbBr_3$ QDs' chemical environment was adjusted to prevent PL quenching. Obtained high PLQYs and the PL in whole visible light. | [37] |
| $Na^+$ | $CsPbBr_3$ | 365 | 526 | – | 94.74 | 31.2 | Enhanced PLQY, external quantum efficiency (EQE) and longer lifetime. | [38] |
| $Rb^+$ | $CsPbCl_3$ | 365 | 420 | – | 13 | 10.2 | Greatly improved PLQY and lifetime | [39] |
| B - site doping | | | | | | | | |
| $Sn^{2+}$ | $CsPbBr_3$ | – | 512.9 | – | 82.77 | 25.26 | Enhanced fluorescence and stability | [40] |
| $Cu^{2+}$ | $CsPbBr_3$ | 365 | 499 | – | 95 | – | Thermal stability increased | [41] |
| $Eu^{3+}$ | $CsPbCl_3$ | 380 | 430,590,616,695 | – | – | – | Enhanced activation energy and thermal stability | [42] |
| $Eu^{3+}$ | $CsPbCl_3$ | 360 | ≈580.16, 593.23, 617, 651.39, 699.26 | – | – | – | The pressure-induced PL enhancement | [43] |
| $Yb^{3+}$ | CsPbBr1·5Cl1.5 | 365 | 990 | – | 90 | 17.79 | Reduction of surface traps and suppression of exciton quenching. | [44] |
| $Nd^+$ | $CsPbBr_3$ | 365 | 459 | – | 90 | 5.27 | Enhancement of the exciton binding energy | [45] |
| $Fe^{2+}$ | $CsPbCl_3$ | – | 401–403 | 13.8–14.6 | 6.2 | 14.6 | Increasing size homogeneity | [46] |
| $Co^{2+}$ | $CsPbCl_3$ | 365 | 516 | 18–20 | 89 | 17.93 | Defect passivation | [47] |
| $Tm^{3+}$ | $CsPbBr_{2.2}Cl_{0.8}$ | 365 | – | – | 54 | 4.8–5 | new energy level introduction | [48] |

et al. [226] employed DBSA as a means to eliminate halogen vacancy defects found on the surfaces of QDs. In contrast, when QDs were prepared using either OAm or OA, a notable decline in PLQY was observed with prolonged washing in ethanol. Additionally, the TRPL lifetime exhibited minimal variation across different washing durations for the $CsPbX_3$ QDs with DBSA ligands, indicating a strong interaction between sulfonate groups and lead ions. In 2020, Huang et al. [228] prepared $CsPbI_3$ QDs capped with dodecyl dimethyl ammonium bromide (DDAB). DDAB was successfully incorporated onto the surface of the QDs, forming a stable combination and effectively passivating surface defects. The introduction of DDAB enabled the $CsPbI_3$ nanocrystals to maintain a PLQY above 80 % for a minimum of 60 days. Yin et al. [229] in the next year used PEI, an amine-based polymer with multidentate ligands, to stabilize and enhance the blue light emission of $CsPbBr_3$ nanosheets. PEI prevented nanosheet aggregation and reduced bromide vacancy defects by interacting with the $PbBr_6$ octahedrons through its alkylamine group. Compared to bare $CsPbBr_3$ nanosheets, those with PEI exhibited stronger and longer-lasting transient absorption, as well as a lower bleach minimum energy. The presence of PEI ligands slowed down the exciton elimination process, as indicated by the slower bleaching recovery kinetics and TRPL spectra.

In addition to the aforementioned three surface ligand modification methods, scientists have put forward various strategies for ligand exchange to enhance the stability of $CsPbX_3$ QDs.

Pan et al. [230] demonstrated a two-step ligand exchange process to passivate $CsPbX_3$ QDs using halide and mixed halide ion pairs. By implementing this process, they were able to create blue and green phosphorescent LEDs based on the passivated $CsPbX_3$ QDs. These phosphorescent LEDs exhibited a sharp electroluminescence (EL) peak with a FWHM of 19 nm, reaching a maximum luminance of 35 cdm-2 for the blue and 330 cd $m^{-2}$ for the green. The phosphorescent LEDs also achieved high EQE of 1.9 % for the blue and 3.0 % for the green, showcasing the potential of all-inorganic lead halide perovskites in achieving efficient and bright phosphorescent LEDs. The study highlighted that the complete ligand exchange process, involving the desorption of protonated OAm ligands and subsequent treatment with halide-ion-pair ligands, improved charge carrier balance and enhanced device EQE. These findings open up avenues for developing high EQE and highly luminescent phosphorescent LEDs using stable inorganic PQDs. Bin-Bin Zhang et al. [231] utilized thionyl halides ($SOCl_2$, $SOBr_2$) as passivating agents for $CsPbCl_3$ QDs in theiir study, deviating from the use of OAm and OA ligands. The introduction of thionyl halides enabled a controlled and gentle reaction with the carboxyl and amine functional groups present on the QD surfaces, facilitating the straightforward exchange of ligands. The modified QDs exhibited a narrow FWHM of 14.6 nm and achieved a blue LED with an EQE of 1.35 %.

Zhu et al. [232] in 2021 conducted a ligand exchange process where in the long-chain ligands, OA and OAm were replaced with DDAB to prepare $CsPbBr_3$ QDs. The QD surfaces displayed a higher binding affinity towards the shorter-chain ligand, DDAB, compared to the long-chain ligands, resulting in a stronger interaction between DDAB and the QDs. The large branched structure of DDAB and its strong affinity with bromide ions ($Br^-$) in the PQDs allowed the dodecyl ammonium cations ($DDA^+$) to effectively passivate surface defect states, resulting in narrow FWHM and high PLQY. The incorporation of DDAB brought about a substantial enhancement in the thermal stability of DDAB-$CsPbX_3$ QDs. This improvement can be attributed to the combined influence of DDAB's notable steric hindrance and the protective effect of the $SiO_2$ core-shell structure. (Fig. 9 c & d). The Table 4 shows various ligands used for enhancing stability and luminescence $CsPbX_3$ QDs.

**Table 4**
Summary of various ligands used for enhancing stability and luminescence of $CsPbX_3$ quantum dots.

| $CsPbX_3$ QDs | Ligands | Luminescence/ Stability | References |
|---|---|---|---|
| $CsPbBr_3$ | DDAB | PLQY 80 %, Increased stability, Narrow FWHM | [49] |
| $CsPbBr_3$ | Phosphine ligands | Bright PL emission even after 4 months stored at ambient condition. | [50] |
| $CsPbBr_3$ | DDAB | Increased PLQY and better stability against ethanol and heat | [51] |
| $CsPbBr_3$ | Thiocyanate ($SN^-$) | PL intensity enhanced by approximately 25 %, EQE increased | [52] |
| $CsPbBr_3$ | Didecyldimethylammonium bromide (DDEAB) | Excellent quantum yield (>90 %) and environmental stability during long-term storage | [53] |
| $CsPbI_3$ | sulfur–oleylamine (S-OLA) | PLQY increased from 52.3 % to 82.4 %, maintained over 80 % of their original PLQY after 20 days, showcasing improved stability against aggregation or degradation. | [54] |
| $CsPbI_3$ | di-*n*-propylamine (DPA) | Higher power conversion efficiency approaching 15 %, better charge transport, and less carrier recombination | [55] |
| $CsPbI_3$ | 2-aminoethanethiol (AET) | Preserve over 95 % of the original PL intensity in water after 1 h and under UV light for 2 h | [56] |
| $CsPbI_3$ | (3-aminopropyl) triethoxysilane APTES | PLQY 84 %, enhanced stability | [57] |
| $CsPbI_3$ | Octylphosphonic acid (OPA) | PLQY 98 %, Enhanced electrical conductivity and EQE, | [58] |

### 6.3. Surface coating

As we discussed earlier, the stability of all-inorganic lead halide PQDs is a major concern due to their tendency to dissolve in polar solvents and their susceptibility to degradation in the presence of moisture, light, and oxygen. To address this issue, researchers have extensively explored surface coating strategies to improve their stability. Coating $CsPbX_3$ QDs with suitable materials can provide a protective barrier, preventing direct contact with environmental factors and reducing the diffusion of Pb ions. These coating materials can be either inorganic or polymer-based. On the other hand, the dynamic characteristics and low lattice energy of PQDs make them prone to dissolution in various polar solvents, including water. To overcome this challenge, researchers have sought ways to completely encapsulate PQDs with inert shell materials. Among different strategies, the coating approach offers a straightforward solution by effectively isolating the PQDs from water and oxygen. Inorganic and polymer and materials can both be used as coatings. In this regard, the widely utilized nontoxic inorganic $SiO_2$ coating method, employing techniques such as Stöber or reverse microemulsion, has found success in traditional quantum dots like lanthanide-doped QDs and magnetic nanocomposites. Notably, $SiO_2$ is an inorganic oxide known for its chemical stability and optical transparency across the visible spectrum. Coating PQDs with $SiO_2$ preserves their optical properties while shielding them from dissolution in polar solvents. Therefore, employing silica coating techniques for $CsPbX_3$ QDs represents a typical approach to enhance their stability and protect their luminescent properties [50,225–227].

Tang's research group [233] successfully employed silica encapsulation to enhance the humidity and thermal stability of $CsPbBr_3$ QDs. Sun et al. [234] synthesized PQD and silica composites by gradually hydrolyzing the organosilicon capping agent in situ. The resulting QD/silica composites displayed excellent PL properties, characterized by narrow line-width and high PLQY. Notably, the air stability of the composites was significantly enhanced. Detailed analysis revealed that the QDs were uniformly embedded within the organic silica matrix. WLEDs constructed using green and red QD/silica composites in a remote configuration exhibited a power efficacy of 61.2 lumens per watt (lm/W) and minimal changes in the emission spectrum even after 10 h of operation. These findings indicate a significant improvement in the performance of PQDs. TEOS (tetraethyl orthosilicate) is currently the widely used silicon source for the synthesis of $SiO_2$ coatings. Hu et al. [235–237] presented a straightforward and convenient method for the in situ growth of silica shells on $CsPbX_3$ QDs without the use of water. In this process, the amorphous $SiO_2$ layer was rapidly formed on the PQDs by injecting the silica precursor tetraethyl orthosilicate (TEOS) at high temperature. The resulting $CsPbBr_3/SiO_2$ composites exhibited enhanced performance compared to pristine $CsPbBr_3$ QDs. These improvements included increased luminous intensity, nonblinking properties, and enhanced optical stability. In a study by Zhang et al. [238] in 2020, the optical properties of $CsPbBr_3@SiO_2$ and $CsPbBr_3$ QDs were comparatively analyzed. The researchers observed that the exciton binding energy of $CsPbBr_3$ QDs increased after silica coating compared to uncoated $CsPbBr_3$ QDs. The optical band gaps of both types of QDs showed continuous broadening with increasing temperature (from 10 to 300 K). Nevertheless, the analysis of the temperature-dependent spectra revealed that the electron-phonon coupling in $CsPbBr_3@SiO_2$ QDs was less pronounced. The introduction of the $SiO_2$ encapsulation layer had a notable influence on both the strength of the electron-phonon coupling effect and the dielectric constant. $SiO_2$ served as an insulating layer, effectively isolating the effects of the substrate and solution on the QDs. Consequently, the electron-phonon coupling effect in $CsPbBr_3@SiO_2$ QDs was reduced. The temperature-dependent time-resolved photoluminescence (TRPL) analysis demonstrated that the PL lifetime of $CsPbBr_3@SiO_2$ QDs increased as the temperature rose, surpassing that of $CsPbBr_3$ QDs when the temperature was elevated from 110 K to room temperature. The enhanced photoluminescence lifetime and reduced phonon effect observed in $CsPbBr_3@SiO_2$ QDs suggested that the silica-coated perovskite materials were well-suited for applications in down-conversion luminescent materials. Furthermore, in a 16-day stability test under ambient air conditions, $CsPbBr_3@SiO_2$ QDs demonstrated superior stability compared to $CsPbBr_3$ QDs.

In 2021, Gao et al. [239] employed TEOS as the silicon source and hydrophobic TOPO as the inhibitor to synthesize $CsPbBr_3@SiO_2$ QDs and the synthesized QDs displayed a remarkable enhancement in PLQY reaching an impressive value of 87 %, as compared to the original QDs. This improvement in PLQY contributed to the overall stability enhancement of the $CsPbBr_3@SiO_2$ QDs (Fig. 10). Nevertheless, the TEOS-based coating process presented difficulties due to the requirement of a harsh alkaline environment. This raised concerns as it could potentially result in the quenching of the QDs.To overcome this, alternative particle powder silicon sources were explored. Metal oxides such as $TiO_2$ (titanium dioxide) and $Al_2O_3$ (alumina) have been investigated for their ability to protect $CsPbX_3$ QDs due to their dense structure and exceptional stability. Loiudice et al. [240] utilized atomic layer deposition (ALD) to deposit alumina as a coating on $CsPbBr_3$ QDs. The obtained composite demonstrated a uniform morphology and composition, featuring an $Al_2O_3$ coating with a thickness of approximately 10 nm. Remarkably, it retained more than 50 % of its PL intensity even when exposed to air or subjected to heating up to 200 °C. In a similar vein, Zhi-Jun Li et al. [241] in the following year, synthesized a $CsPbBr_3@TiO_2$ composite by calcinating a $TiO_2$ precursor at 300 °C. Introducing a $TiO_2$ shell to the $CsPbBr_3$ resulted in a slight enhancement in UV spectrum absorbance, which can be attributed to the UV activity of the core/shell $TiO_2$ surface layer. However, the addition of the $TiO_2$ shell led to a reduction in the PL intensity of $CsPbBr_3@TiO_2$, suggesting the presence of a new nonradiative pathway within the core/shell nanocrystals. This phenomenon could potentially be explained by electron transfer from the conduction band of $CsPbBr_3$ to the $TiO_2$ shell. However, it is worth noting that the $TiO_2$ shell layer demonstrated excellent protective properties, as the PQDs remained stable in water for a minimum period of three months without undergoing degradation. Inorganic salts have been also explored as coating materials to enhance the stability of PQDs. Wei et al. [242] integrated $CsPbBr_3$ QDs into $CaF_2$

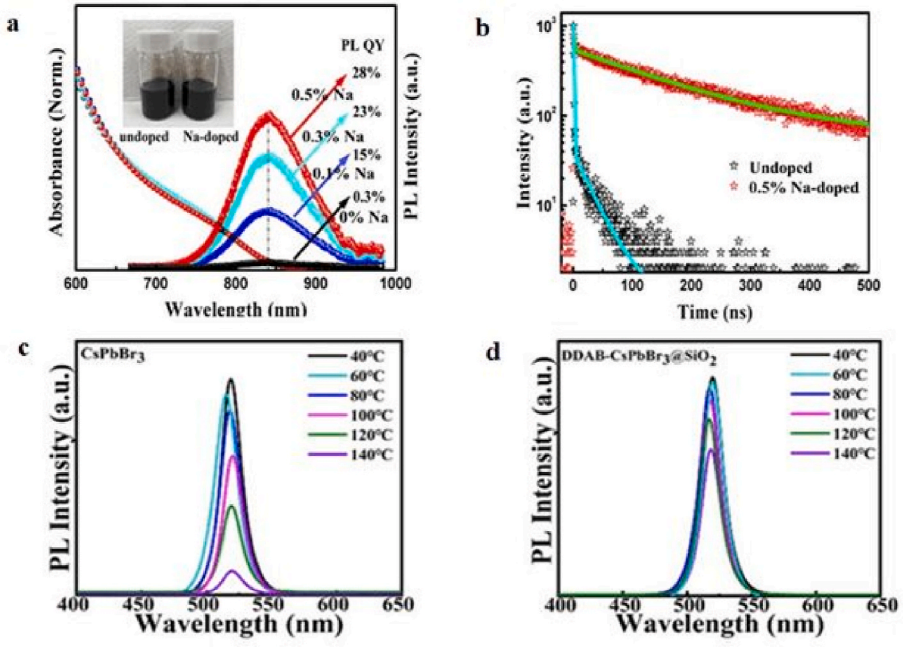


**Fig. 9.** a) UV–vis and PL spectra of $Na^+$doped and undoped QDs. b) TRPL decay of the QDs c) and d) PL spectra of annealed $CsPbBr_3$ and DDAB-$CsPbBr_3@SiO_2$ QD films for 10 min at various temperatures adapted from [220].

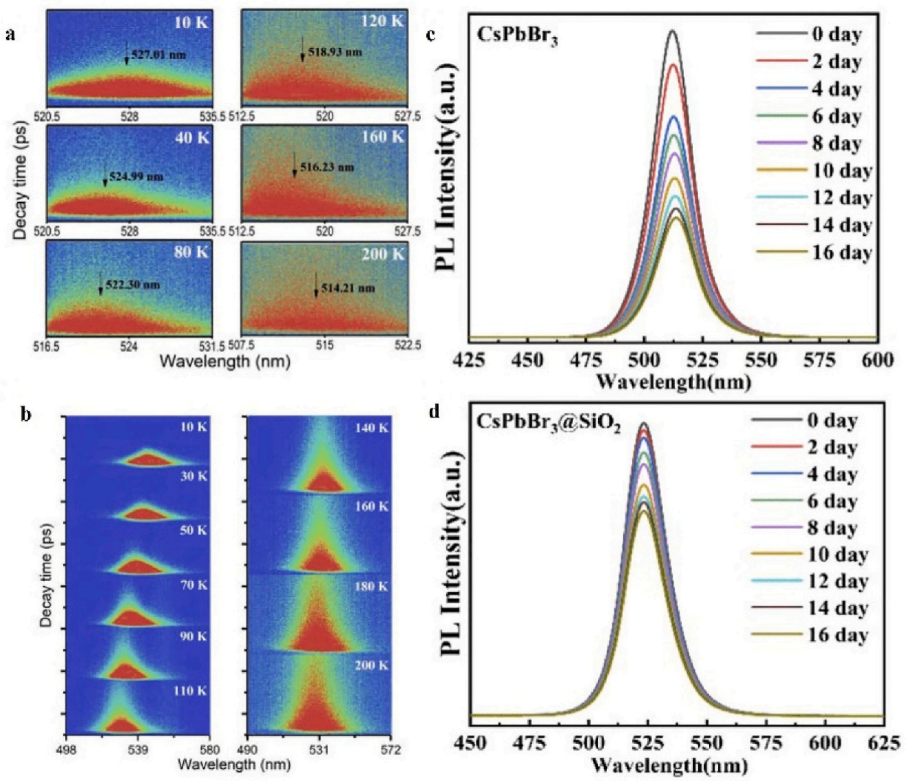


**Fig. 10.** Time-resolved photoluminescence of (a) $CsPbBr_3$ QDs and (b) $CsPbBr_3@SiO_2$ QDs at various temperatures. PL spectra of (c) $CsPbBr_3$ QDs and (d) $CsPbBr_3@SiO_2$ QDs recorded at various time intervals adapted with open access from Ref. [220].

nanoparticles, which significantly improved stability against moisture, light radiation, and anion exchange.

Polymer coatings offer various benefits such as high flexibility, ease of processing, and a low photo-absorption coefficient. These coatings can effectively envelop $CsPbX_3$ QDs by forming tightly packed polymer chains. This enhanced interaction between the polymer ligand and QDs creates a protective barrier, improving the QDs' resistance to water and oxygen. Additionally, polymer coatings help mitigate issues such as fluorescence quenching, potential toxic $Pb^{2+}$ contamination, and QDs aggregation. Furthermore, the application of polymer coatings significantly enhances the thermal and moisture stabilities of the QDs [220]. Cai et al. [243] introduced a simple and efficient method for synthesizing water-resistant $CsPbBr_3$ PQDs loaded polymethyl methacrylate (PMMA) composite microspheres ($CsPbBr_3$@PMMA). The synthesis involved precipitation polymerization of methyl methacrylate in hexane in the presence of $CsPbBr_3$ PQDs and a stabilizer. The resulting $CsPbBr_3$@PMMA microspheres exhibited tunable sizes and a narrow size distribution, with the PQDs uniformly dispersed within the PMMA microspheres. This successful incorporation is attributed to strong coordination interactions between Pb ions on the PQD surface and carbonyl groups (C═O) from PMMA. By employing this mechanism, multicolour composite microspheres can be easily prepared by incorporating different $CsPbX_3$ (X = Cl, Br, I) PQDs into blank PMMA microspheres. The PMMA microspheres effectively protect the embedded $CsPbBr_3$ PQDs, enhancing their water resistance and storage stability. Additionally, the researchers demonstrated the fabrication of a wide-colour-gamut WLED by combining green-emitting $CsPbBr_3$@PMMA composite microspheres with red-emitting $K_2SiF_6$:$Mn^{4+}$ and a blue LED. This LED configuration shows potential for application as backlights in liquid crystal displays. Xu et al. [244] in 2020 employed poly maleic anhydride-*alt*-1-octadicene (PMAO) as a coating material for $CsPbX_3$ QDs. The PMAO layer functioned as a protective barrier by engaging with the surface ligands of the PQDs through its anhydride group. TRPL measurements revealed a prolonged PL lifetime for $CsPbX_3$/PMAO QDs, indicating an enhancement in their photoluminescence properties. Transient absorption spectroscopy results indicated that PMAO could slow down the relaxation of intra-band hot excitons and the recombination of excitons in $CsPbX_3$ QDs. Furthermore, the PL quantum yields of green $CsPbBr_3$ QDs and red $CsPbBr_{0.6}I_{2.4}$ QDs were enhanced after PMAO coating. A WLED device was created by combining green $CsPbBr_3$/PMAO QDs and red $CsPbBr_{0.6}I_{2.4}$/PMAO QDs with a blue GaN chip. This integration resulted in enhanced stability compared to using the original PQDs alone. The glass embedding method is a viable approach to enhance the stability of $CsPbX_3$ QDs during their synthesis. Aryal et al. [245] incorporated $CsPbBr_3$ QDs into a glass matrix using the conventional melt-quenching technique. The resulting glasses containing $CsPbBr_3$-embedded QDs exhibited stable photoluminescence emission, with no changes in their emission peaks and full-width at half-maximum, for a duration of at least six months under ambient conditions.

Surface treatments play a pivotal role in enhancing the photoluminescence properties and stability of $CsPbX_3$ quantum dots. Recently, Guo et al. [246] introduced a novel approach to enhance the environmental stability of $CsPbX_3$ QDs. By incorporating 4-sulfamoyl benzoic acid (4-SABA) during synthesis for surface modification and utilizing a layered $SiO_2$ substrate for encapsulation, the resulting 4-SABA-$CsPbBr_3/SiO_2$ composites demonstrated a remarkable photoluminescence quantum yield of 96 % and a notable improvement in stability to water and ethanol. Haque et al. [247] reported surface treatment of strongly confined $CsPbBr_3$ QDs with sodium thiocyanate demonstrated enhanced PLQY. The investigation extends to the single-particle level, highlighting that embedding both treated and untreated QDs in a polystyrene matrix not only shields them from environmental deterioration but also contributes to the blinking process through favourable band alignment. This emphasizes the critical role of surface treatment in improving the stability and optical properties of

quantum dots, especially in the context of single-particle behaviour. Eb et al. [248] reported effective control of QD size and the stabilization of the $CsPbI_3$ crystal phase through guanidinium iodide (GAI) treatment. GAI suppressed halide defects through multiple hydrogen bonding on the QD surface, resulting in enhanced ambient photoluminescence and photostability compared to pristine QDs. Notably, $CsPbI_3$ QD LEDs exhibit exceptional external quantum efficiency (22.5 %) and extended operational stability (over 10 h) due to the synergistic effects of precise size control and GAI treatment. Table 5 summarizes the coatings on CsPbX3 QDs with various materials and the advantages of it.

## 7. Applications

### 7.1. QDLED application

PQDs offer significant advantages over bulk perovskite materials in terms of strong exciton confinement, making them promising next-generation optical materials for a range of lighting applications [56, 57]. The rapid growth of QDLED necessitates research into more effective emitters, like PQDs. High radiative recombination, high defect tolerance, and good optical qualities are some of the attributes that have made them a rising star among QDLED emitters. There have been numerous studies done on PQDLED to improve performance through composition design, surface engineering, and device structure change. Since the first CdSe QD-based QDLEDs were published in 1994, a number of different QD candidates, including CdS, CdTe, InP@ZnSeS, and Cu-doped ZnInS, have been reported as prospective emitting materials for QDLEDs. Evidently, wurtzite or zinc blende Cd-based QDs have been the only widely used QDLED materials studied during the past 20 years [146].

$CsPbX_3$ QDs possess desirable properties such as long-range charge transport [249,235], tunable emission wavelength in full visible range by halide anion composition (X site = Cl for blue emission, Br for green emission, or I for red emission) or size of QDs, cost-effectiveness, and ease of processing at relatively low temperatures. Specifically, $CsPbBr_3$ QDs demonstrate a high PLQY of at least 70 % and a relatively short PL lifetime [250,251] One of the important characteristics of LHP-QDs is their narrow FWHM emission, which is superior to that of typical organic emitters (fluorescent and phosphorescent materials) or Cd-based core-shell QDs at wavelengths of 15 nm for blue, 20 nm for green, and 30 nm for red, respectively [252–254]. These characteristics make $CsPbBr_3$ QDs highly attractive for applications in displays, white light emission, visible light communications, and other lighting technologies.

$CsPbX_3$ QDs play a pivotal role in both electroluminescent and photoluminescent displays. Electroluminescent displays, typically powered by an electron current, leverage Quantum Dots for direct emission. On the other hand, photoluminescent displays rely on down-conversion luminescent materials, including Quantum Dots, which are seamlessly incorporated into various components such as light sources, backlight elements, functional films, or display panels. The characteristics of these luminescent materials significantly impact display performance, necessitating high luminescence efficiency, colour purity, and stability [118]. By distinctly addressing the use of these QDs for electroluminescence and their role as phosphors for photoluminescence, a more comprehensive understanding of their applications in LED technology can be achieved.

#### 7.1.1. Photoluminescence QDLEDs

Colloidal QDs have emerged as favourable emissive substances to substitute organic or molecular phosphors in phosphor converted LEDs. In 2015, Song et al. [146] demonstrated the fabrication of blue, green, and yellow QDLEDs based on all-inorganic $CsPbX_3$ PQDs with narrow emission spectra for the first time. By varying the anion composition and content, the colour of the QDLEDs could be tuned from blue to orange. The QDLEDs exhibited high luminance values, reaching 742 cd $m^{-2}$ for

**Table: 5**
A brief summary of the different surface coating materials utilized in $CsPbX_3$ quantum dots and their advantages.

| $CsPbX_3$ QDs | Coating material | Advantages | References |
|---|---|---|---|
| *Inorganic coating* | | | |
| $CsPbBr_3$ | $SiO_2$ aerogel | Improved water stability. Maintains 83 % PL intensity after five days of water dispersion. | [59] |
| $CsPbBr_3$ | $SiO_2$ | PLQY 73 %, Luminescence stability enhanced by about 40 %. | [60] |
| $CsPbBr_3$ | $SiO_x$ -$AlO_x$ | Enhanced PL intensity by photoactivation | [61] |
| $CsPbI_3$ | $SiO_2$ | PLQY 97.5 %, Improved stability against air, heat, and ethanol | [62] |
| $CsPbBr_3$ | $SiO_2$ | Enhanced chemical stability, PLQY 71.6 %, 84 % of the original PL intensity was retained following an 80-min heating period at 60 °C. | [63] |
| $CsPbBr_3$ | $SiO_2$ | Better thermal stability and long PL lifetime | [64] |
| $CsPbBr_3$ | Sn– $TiO_2$ | long-term stability in water system, enhanced photocatalytic activity, demonstrating 96.6 % degradation efficiency | [65] |
| $CsPbI_3$ | $TiO_2$ | Significant improvement in stability against toluene, water ultrasonication, and light | [66] |
| $CsPbBr_{3-x}I_x$ | ZnS | Enhanced photostability, more tunable | [67] |
| $CsPbBr_3$ | Mesoporous Silica | PLQY 70 %, Increased stability and prevent ion exchange. | [68] |
| *Polymer coating* | | | |
| $CsPbBr_3$ | PMMA | Enhanced stability against water, heat, and photoirradiation stimuli | [69] |
| $CsPbBr_3$ | PMMA | Exceptional stability retaining 80 %, 87 %, 53 %, 59 %, and 64 % of its initial luminous intensity after exposure to UV light for 12 days, LED irradiation for 10 days, heating at 60 °C for 10 days, humidity, and ethanol soaking for 3 h | [70] |
| $CsPbBr_3$ | PMMA | Enhanced stability, PLQY increased from 60.2 % to 90.1 %. | [71] |
| $CsPbBr_3$ | PMMA | Excellent phase purity, homogenous size distribution, and a uniform shape in the QD. Improved stability | [72] |
| $CsPbBr_3$ | Polypyrrole (PPy) | improves water stability, allowing for the preservation of structure and morphology even after 30 days immersion in water. | [73] |
| $CsPbBr_3$ | PMMA | PLQY≈ 82.7 % and FWHM ≈18.6 nm, long-term stability to UV irradiation, heat, and water | [74] |
| $CsPbI_3$ | Poly (isobutylene-*alt*-maleic anhydride) (PIMA) | PLQY above 90 %, Highly photo-thermal resistant | [75] |
| $CsPb(Br/I)_3$ | PMMA | Enhanced luminescence and better water resistance. | [76] |
| $CsPbI_3$ | poly-3-hexylthiophene | Enhanced stability and promotes efficient charge extraction and transport in QDs | [77] |

blue, 946 cd $m^{-2}$ for green, and 528 cd $m^{-2}$ for orange QDLEDs, with corresponding EQE of 0.07 %, 0.12 %, and 0.09 % respectively. These findings highlight the potential of all-inorganic perovskite $CsPbX_3$ QDs as a promising family of photoelectric materials for various optoelectronic applications. In a similar, In their study, Du et al. [255] accomplished the synthesis of superior $CsPbBr_3$ PQDs at ambient temperature, employing CsBr as a precursor. Through anion exchange reactions, the emission spectra of the QDs could be finely adjusted across the entire visible spectrum. Utilizing these $CsPbBr_3$ QDs, an LED device was successfully fabricated, demonstrating an EQE of 0.06 %. By employing anion exchange reactions, the emission spectra of the QDs could be tuned across the entire visible spectral range. The fabricated LED device using $CsPbBr_3$ QDs achieved an EQE of 0.06 %. High-performing perovskite $CsPbBr_3$ green QDLEDs were produced by Fang et al. [256] by adjusting the charge injection equilibrium and implementing a bilayered structure for electron transport. The devices obtained from this approach demonstrated vibrant green emission with FWHM of 18 nm and a turn-on voltage below the bandgap at 2.0 V. as well as a record efficiency (EQE of 21.63 %) and exceptional repeatability. More significantly, compared to the control device, the device with better charge injection balance offers good operational stability with a nearly 20-fold improvement. Li et al. [257] developed a surface ligand engineering method to improve the performance of $CsPbBr_3$ QDLEDs. By controlling the ligand density on the QD surfaces through a recyclable treatment, they achieved a significant enhancement in the EQE of the QDLED device. Additionally, they introduced phenethylamine (PEA) as a short conjugation molecular ligand to replace long insulating ligands on $CsPbX_3$ QDs, resulting in improved carrier injection and transport. The incorporation of PEA led to near-unity PLQYs for $CsPbBr_3$ and $CsPbI_3$ QDs and higher luminance in QDLEDs. Furthermore, the EQE of $CsPbI_3$ QDLEDs reached an impressive 14.08 %, representing one of the highest reported efficiencies for red perovskite LEDs.

In 2022, Zang et al. [258] introduced, a fluorinated aromatic ammonium bromide compound, specifically fluorophenethyl ammonium bromide (FPEABr), during the synthesis of $CsPbBr_3$ QDs. The effects of fluorination positions (ortho, meta, and para) on the benzene ring are systematically investigated to evaluate their impact on the optical properties and stability of $CsPbBr_3$. The results demonstrate successful adsorption of the short fluorinated aromatic alkyl ammonium chain onto the QD surface, leading to a significant reduction in bromine vacancy defects. As a result, stable $CsPbBr_3$ QDs with a high PLQY exceeding 90 % are achieved using pFPEABr. Moreover, the short ligand chains improve carrier transport in the $CsPbBr_3$ QD film, and surface treatment enhances the maximum luminance of the corresponding perovskite QDLEDs from 531 to 1278 cdm-2. This surface ligand engineering strategy employing FPEABr, particularly pFPEABr, presents a promising direction for the future development of high-performance QDLEDs. At ambient temperature, Wu et al. [259] produced $Mn^{2+}$-doped $CsPbX_3$ QDs with $SiO_2$-coated surfaces that showed high PLQYs. The $CsPb_{0.7}Mn_{0.3}Br_{0.75}Cl_{2.25}@SiO_2$ QDs' orange-yellow PL displayed great temperature and moisture stabilities, and their PLQY was also rather high. A UV LED chip (365 nm) was coated with high-quality orange--yellow QDs to fabricate a WLED device, as shown in Fig. 11 a and b. After 16 h of continuous operation, there was no discernible change in the light intensity.

The performance of LEDs using RT-QDs is inferior to those using HI-

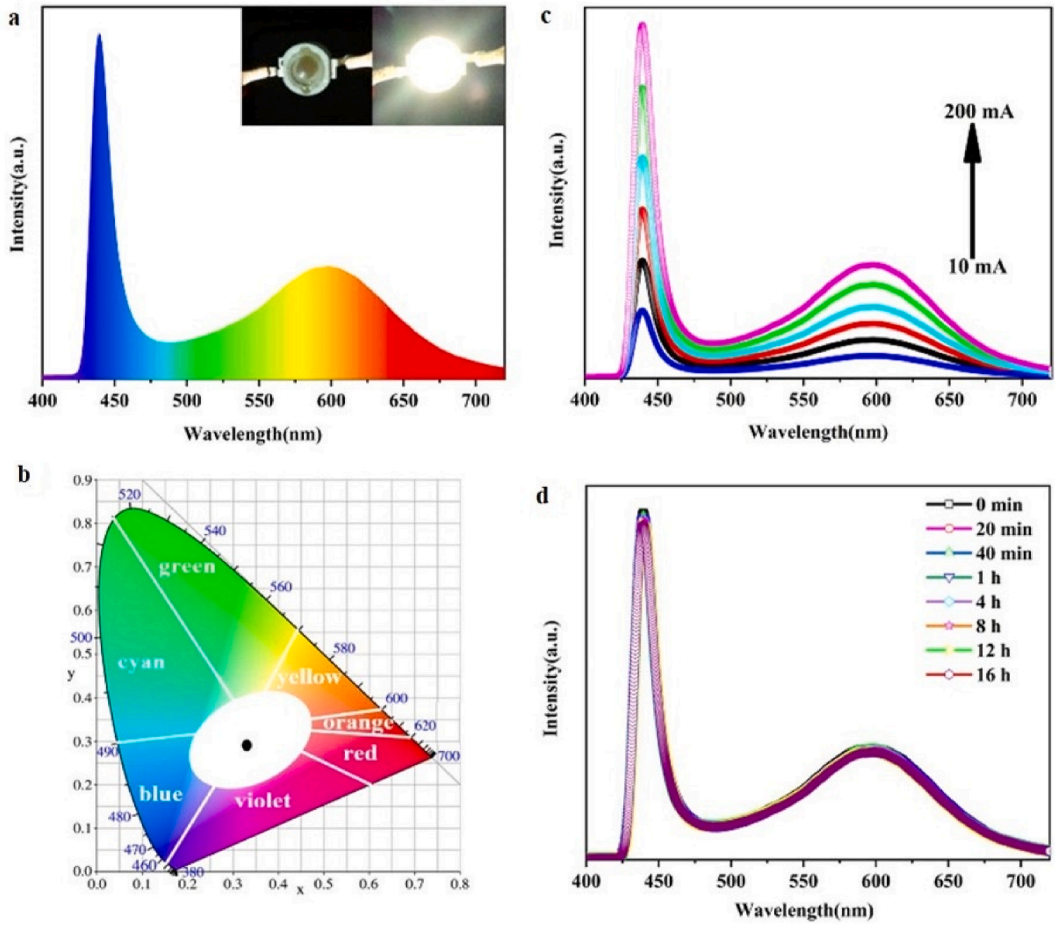


**Fig. 11.** a) White emission spectrum at a driving current of 20 mA b) CIE chromaticity diagram of the device c) Connection between the working current and the WLED emission spectrum d) WLED PL spectra recorded at various times adapted with open access from Ref. [220].

QDs. While ligand removal techniques are commonly employed to improve LED performance, it is insufficient for RT-QDs. Additional steps involving ligand engineering and annealing are required to effectively remove excess ligands from RT-QD films without causing QD coalescence. Any surface defects induced by annealing can be addressed through subsequent photoactivation. Furthermore, using solution processable inorganic charge transport layers can reduce LED fabrication costs. An inverted LED configuration utilizing a metal oxide electron transport layer and an RT-QD emitting layer was fabricated by Moyen and his research group [260], achieved a maximum current efficiency of 17.61 cdA-1 and a maximum luminance of 22,825 cdm-2. Tien et al. [31] utilized ultrasonic oscillation-synthesized $CsPbX_3$ QDs as the active layer in blue, green, and red LED devices. However, the achieved LEDs demonstrated a relatively low EQE. In a similar vein, Yun et al. [261] utilized $CsPbBr_3$ QDs to fabricate LEDs. To avoid potential harm caused by polar solvents in the conventional spin coating process, the researchers employed a low-temperature atomic layer deposition (ALD) technique. This allowed them to deposit electron transfer layers consisting of $Al_2O_3$ and ZnO, thus preventing any associated damage.

WLEDs based on $CsPbBr_3$ QDs offer a wide colour adjustment range and good lighting application features. WLEDs frequently combine blue LED chips with red commercially available phosphor coatings and green PQDs. Significant advancements have been made in $CsPbX_3$ QD-based WLEDs in recent years. Yan et al. [262] developed a technique to enhance the brightness and stability of $CsPbBr_3$ QDs by introducing $Sn^{2+}$ ions at room temperature for the fabrication of WLEDs. By doping the QDs with 20 % $Sn^{2+}$, they achieved a PLQY of 82.77 %. WLEDs using these QDs with 20 % $Sn^{2+}$ doping exhibited excellent colour rendering properties, with an enhanced colour rendering index (CRI) of 89 and a correlated colour temperature (CCT) of approximately 3954 K. Tang et al. [263] fabricated a WLED by using the ultrathin, core–shell structured $SiO_2$ coated $Mn^{2+}$ doped $CsPbX_3$ QDs via one facile reverse microemulsion method at room temperature. By using a multibranched capping ligand called trioctylphosphine oxide, the breakage of $CsPbMnX_3$ core QDs caused by silane hydrolysis was effectively prevented. A silica shell with a controlled thickness of up to 2 nm was successfully formed around the $CsPbMnX_3$ QDs, resulting in high PLQY of 50.5 % and improved thermal stability and water resistance. When mixed with $CsPbBr_3$ QDs emitting green light, the $CsPbMnX_3@SiO_2$ QDs emitting yellow light showed no ion exchange effect, enabling the generation of white light emission. Consequently, a WLED was created by combining a blue on-chip LED device with the aforementioned perovskite mixture. The resulting WLED exhibited a high luminous efficiency of 68.4 lm/W and a high colour-rendering index of 91. A liquid-type LED configuration utilizing all-inorganic $CsPbX_3$ QDs has been reported by Wang et al. The researchers developed a liquid-type encapsulation structure by combining a blue LED with $CsPbX_3$ QDs synthesized using a HI method. These QDs were utilized as a liquid-type colour-conversion layer that was securely enclosed within a glass slab. This liquid-type colour conversion layer offers the advantage of preserving the high PLQY of the QDs while safeguarding them from environmental factors such as heat, moisture, and air. The resulting green, yellow, orange, and red-emitting LEDs exhibited a remarkable EQE of 14.6 %. Notably, the liquid-type LEDs exhibited superior colour stability compared to solid-state LEDs. Addressing the long-term stability concerns of $CsPbX_3$ QDs, researchers have explored the incorporation of QDs into mesoporous silica (MS) for the synthesis of LEDs.

### 7.1.2. Electroluminescence QDLEDs

Wang et al. [264] reported an improvement in the brightness of $CsPbBr_3$ electroluminescence QDLEDs by optimizing PEDOT:PSS (poly (3,4-ethylenedioxythiophene):poly (styrene sulfonate) films. Despite PEDOT:PSS being a common hole-transport material in QDLEDs, its low conductivity negatively affects device performance. The authors introduced a surface-annealing method using toluene and ethylene glycol, significantly enhancing conductivity compared to traditional air annealing. The modified PEDOT:PSS films led to a smoother surface, improved conductivity, and, consequently, a 48 % increase in luminance (31,140 cd $m^{-2}$) and a 25 % rise in power efficiency (13.4 lm/W) in $CsPbBr_3$ QDLEDs. Chen et al. [265] reported the advancements in blue electroluminescent QDLEDs, which hold promise for display applications due to their vi brant colour saturation, high brightness, tunability, and cost-effectiveness. Despite remarkable progress in red and green QD-LEDs, the performance of their blue counterparts still trails behind. The review delves into recent developments in blue QD-LEDs, covering Cd-based, perovskite-based LEDs, and heavy-metal-free QDLEDs. They highlighted notable efficiency improvements in Cd-based blue QD-LEDs, reaching approximately 20 %, achieved through strategic optimizations. Additionally, perovskite LEDs, especially those incorporating quasi-2D organic–inorganic perovskites, demonstrate an impressive external quantum efficiency exceeding 11 %. The review also encapsulates advancements in heavy-metal-free blue QD-LEDs utilizing ZnSe, InP, Cu-based QDs, and carbon dots, showcasing promising developments despite performance gaps. In conclusion, Chen et al. discuss challenges and propose potential directions to accelerate further progress in the realm of blue QD-LEDs. Surface lignd engineering is crucial to improving perovskite QDLED performance. Surface capping ligands can increase PQD stability by removing surface trap states, but they also create an insulating coating that prevents charge injection and transport inside the light-emitting layer of perovskite QDLEDs. Hence, proper surface ligand modification aids in improving perovskite QDLED performance. To address the limitations posed by long insulating ligands such as OA and OLA on the surface of QDs, the addition of octylphosphonic acid (OPA) with a shorter carbon chain was implemented by Lu et al. [58] during the synthesis of PQDs. By partially replacing OA ligands with OPA, the electrical conductivity of the QDs was improved while mitigating the negative effects caused by the loss of ligands. The strong interaction between OPA and Pb atoms enabled effective passivation of under-coordinated Pb atoms on the surface of $CsPbI_3$ QDs, resulting in enhanced fluorescence quantum efficiency close to unity and improved solution stability. Additionally, the introduction of shorter chain OPA ligands led to an increase in the electrical conductivity of the QD films from $5.3 \times 10^{-4}$ to $1.1 \times 10^{-3}$ S/m. Through these improvements, highly efficient red perovskite QDLEDs were achieved, exhibiting a peak EQE of 12.6 % and a maximum luminance of 10,171 cd $m^{-2}$ in a top-emitting device structure. This represented a nearly three-fold enhancement in luminance compared to LEDs based on pristine $CsPbI_3$ QDs. Zhu et al. [232] conducted a study on $CsPbX_3$ QDs using a short chain ligand called DDAB through ligand-exchange for the fabrication of WLED. The modification with DDAB resulted in an increase in the PLQY of $CsPbBr_3$ QDs solution from 75.79 % to 82.21 %. To enhance their properties further, the researchers prepared $SiO_2$-coated DDAB-$CsPbBr_3$ QDs by encapsulating them through tetramethoxysilane (TMOS) hydrolysis. These $SiO_2$-coated QDs exhibited a longer photoluminescence lifetime, improved thermal stability, and resistance to water. Additionally, DDAB-$CsPbBr_1I_2@SiO_2$ QDs were synthesized, and a high-efficiency white LED device was developed by combining green light-emitting DDAB-$CsPbBr_3@SiO_2$ QDs and red light-emitting DDAB-$CsPbBr_1I_2@SiO_2$ QDs as down-conversion luminescent materials on a commercial blue GaN chip. The resulted white LED emitted bright white light and demonstrated good electroluminescence stability, with a colour coordinate of (0.35, 0.348) and a colour temperature of 5274 K at an injection current of 30 mA. The performance comparison of LEDs based on CsPbX3 QDs is given in Table 6.

Green $CsPbBr_3$ QDs and orange-red $SiO_2$ wrapped Mn dopped $CsPbCl_3$ QDs are used by Chen and co workers [239] to create WLED devices. With a forward current of 20 mA and a high luminous efficiency of 77.59 lm/W, the as-obtained white LED device simulates brilliant natural light with a CCT value of 3950 K and a corresponding CRI of 82. After 24 h of operation, the electroluminescence spectra exhibits almost no fluctuation. In 2023, Chu et al. [53] developed a WLED by combining green $CsPbBr_3$ QDs passivated with didecyldimethylammonium

**Table 6**
Performance comparison of the LEDs based on $CsPbX_3$ QDs.

| $CsPbX_3$ QDs | Luminous colour | EL peak/PL peak $\lambda_{max}$ (nm) | Max. EQE (%) | Current efficiency $CE_{max}$ (Cd/A) | Turn on Voltage (V) | Max. L (cd $m^{-2}$) | Ref |
|---|---|---|---|---|---|---|---|
| $CsPbBr_xI_{3-x}$ | Red | 640 | 16.7 | – | 1.7 | 13,730 | [78] |
| $Na^+/Cu^{2+}$: $CsPbBr_3$ | Blue | 485 | 4.52 | – | 2.4 | 7161 | [79] |
| $CsPbBr_3$ | Green | 519 | 10.5 | 36.1 | 2.2 | 13,649 | [80] |
| $CsPbBr_3$ | Green | 518 | 0.091 | 0.29 | – | 2439 | [81] |
| Al:$CsPb(Br/Cl)_3$ | Deep Blue | 463 | 1.38 | – | 5 | 120 | [82] |
| $CsPbBr_3$ with $ZnBr_3$ | Green | 518 | 6.43 | 21.1 | – | 96,392 | [83] |
| $CsPb(Br/Cl)_3$ | Blue | 483 | 4 | – | – | 1251 | [84] |
| $CsPbBr_3$ | Green | 515 | – | 21.60 | 4 | 11,777 | [85] |
| $CsPbBr_3$/CdS | Green | 516 | 0.4 | 0.3 | 4 | 354 | [86] |
| FA: $CsPb(Cl_{0.5}Br_{0.5})_3$ | Blue | 474 | 5.01 | – | 5 | 1452 | [87] |
| PEA- $CsPb(Cl/Br)_3$ | Blue | 470 | 2.15 | 6 | – | 620 | [88] |
| $Ni^{2+}$: $CsPbCl_xBr_{3-x}$ | Blue | 470 | 2.4 | – | 5 | 612 | [89] |
| $Na^+$: $CsPbBr_3$ | Green | 516 | 8.97 | 34.5 | 2.5 | 20,190 | [38] |
| $In^{3+}$: $CsPb(Br_xCl_{1-x})$ | Red | 639 | 11.2 | – | – | 423 | [90] |
| $CsPbI_3$ | Red | 630 | 6.4 | 5.2 | 5 | 1037 | [91] |
| $CsPbBr_3$ | Green | 516 | 1.71 | 4.25 | – | 5711 | [92] |
| $CsPbBr_3$ | Green | 517 | 5.7 | 19.9 | 2.3 | 46,000 | [30] |
| $CsPbI_3$ | Red | 682 | 12.6 | – | 2 | 10,171 | [58] |
| $CsPbI_3$ | Red | 660 | 0.25 | 0.84 | – | 217 | [93] |
| $CsPbBr_3$ | Green | 510 | 2.09 | 6.28 | – | 1889 | |
| $CsPbBr_1Cl_2$ | Blue | 484 | 0.044 | 0.11 | – | 36 | |

bromide (DDEAB) and red DDEAB-$CsPbBr_1I_2$ QDs with blue commercial GaN chips. The resulting WLEDs exhibited a wide colour gamut (NTSC 123 %) and demonstrated excellent electroluminescence stability, lasting for more than 12 h.

### 7.2. Solar cell applications

Solar energy, harnessed through efficient solar cells, offers a sustainable and environmentally friendly solution to global energy needs by directly converting sunlight into electricity with minimal losses and greenhouse gas emissions. PQD's structural, electrical, and optical characteristics make them ideally suited for the production of solar cells and other energy storage technologies. In 2016, Sanehira and colleagues [266] proposed the first PQD solar cell, which had a high open-circuit voltage of 1.23 V, a 10.77 % efficiency, and outstanding air stability. This PQD solar cell was very competitive with its polycrystalline thin-film equivalents. Because of the outstanding characteristics of perovskites and the clever surface modification strategies of colloidal PQDs, PQD solar cells achieved a record efficiency of 13.4 % in 2017, exceeding all previously reported QD solar cells [267–269]. Since then, PQD solar cells have garnered more research interest and have attained the highest certified efficiency of 16.6 %, suggesting their enormous potential for producing stable and effective perovskite solar cells.

The PQD solar cell device consists of multiple layers, including a conductive oxide front layer (FTO, ITO), a PQD absorber layer between electron transport materials (($TiO_2$, $SnO_2$), and a hole transport layer (Spiro-OMeTAD, $PTB_7$, PTAA, $P_3HT$) as shown in Fig. 12 a. The absorber layer in a photovoltaic device plays a crucial role in determining its performance. The choice of material for the absorber layer depends on parameters such as film thickness, bandgap, doping concentration,

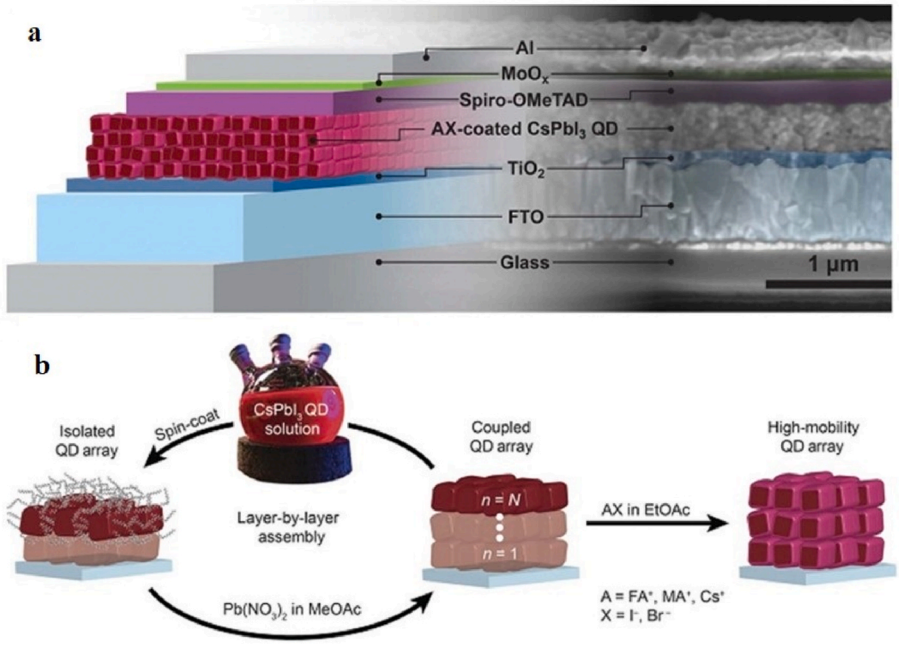


**Fig. 12.** a) An illustration depicting the working principle of QD solar cells b) The growth process of the $CsPbI_3$ QD absorber layer is demonstrated through the spin coating technique adapted from Ref. [270] CC BY-NC 3.0.

defects density, and operating temperature [245,246].

Different types of absorbers have been used, including dye molecules in dye-sensitized solar cells (DSSCs) and polymers with tunable bandgaps. However, these materials have limitations such as limited wavelength range, liquid phase dependence, low crystallinity, and shorter carrier diffusion length, which ultimately lead to lower efficiency. On the other hand, perovskite materials, particularly all-inorganic PQDs, possess desirable characteristics for an absorber layer and have demonstrated high power conversion efficiencies (PCE) of over 16 % in a relatively short period of time. There are two main device architectures, conventional and inverted, depending on current flow and illumination. The mechanism of the device architecture using a simple layer-by-layer approach is depicted in Fig. 12b. The choice of hole-transporting materials (HTMs) is an ongoing area of research due to stability and cost issues. 2,2,7,7-tetrakis (N,N-di-methoxy-phenyl amine)-9,9-spirobifluorene (Spiro-OMeTAD), commonly used, has limitations, but doping and oxidation can improve its properties [113].

Among various PQDs, Solar cells of $CsPbX_3$ QDs have garnered increased attention for their exceptional resilience to high temperatures, moisture, and UV light, while exhibiting a noteworthy improvement in power conversion efficiency, making them highly promising for solar energy applications [271]. Nowadays, $CsPbI_3$, $CsPbI_2Br$, $CsPbIBr_2$, and $CsPbBr_3$ are the most widely used inorganic perovskite solar cells. A good choice for solar energy harvesting is the $CsPbI_3$ material, which has a tiny band gap. Black α- $CsPbI_3$ has been extensively researched for its potential in solar energy applications. Its bandgap of 1.73 eV aligns well with the solar spectrum, making it an ideal candidate. However, the efficiency of devices based on this crystalline composition is currently limited [272–275]. This limitation stems from the low temperature phase transition to yellow δ-$CsPbI_3$, which has a larger bandgap of 2.82 eV, carrier mobility below 0.1 $cm2V^{-1}s^{-1}$ and inferior optical properties. However, when heated to 360 °C, δ-$CsPbI_3$ will change from the yellow phase to the black phase, allowing the bandgap to drop to 1.73eV and the mobility to rise to 25 $cm2V^{-1}s^{-1}$ making it more suitable for solar cell applications [60–62].

In a study conducted by Luo et al. [276], they successfully fabricated a $CsPbI_3$ solar cell under fully open-air conditions. They achieved this by stabilizing the black phase of α-$CsPbI_3$ using hydrochloric acid and isopropanol treatment. The α-$CsPbI_3$ black phase exhibited notable stability in ambient conditions for a duration of 72 h, providing ample time for the successful completion of the device fabrication process. The solar cell was designed with the architecture of FTO/$TiO_2$/α-$CsPbI_3$/spiro-MeOTAD/Ag and achieved a PCE of 4.13 %. It is worth noting that mesoporous $TiO_2$ (*m*-$TiO_2$) is recognized as one of the most effective electron transport materials for photovoltaic applications.

Yuan and his coworkers [277] recently achieved $CsPbI_3$ QD solar cells with an optimum efficiency of 12.55 %. In their research, they utilized a range of polymeric HTMs without the need for dopants. By employing polymer HTMs in $CsPbI_3$ QD solar cells, the researchers were able to enhance device stability and eliminate the complex doping and oxidation processes typically required by conventional HTM, Spiro-OMeTAD.

Huang et al. [278] successfully developed high-efficiency solar cells by employing B-site doping in $CsPbI_3$ quantum dots to stabilize the cubic structure. This strategic approach was undertaken with the aim of advancing the development of efficient solar cell technologies. They employed $Mn^{2+}$ and $Zn^{2+}$ ions as dopants in their study to decrease the lattice constant of $CsPbI_3$ quantum dots, thus increasing the Goldschmidt tolerance factor and the binding energy between Pb and I ions. The findings indicated that substituting smaller metal ions into the crystal lattice of $CsPbI_3$ enhanced the stability of the crystal structure, making it more resistant to phase transitions induced by crystal size increase during the purification process. Additionally, the results demonstrated that B-site doping reduced the defect density in the quantum dots by minimizing lattice distortion and improving crystal quality. Consequently, the solar cells based on doped quantum dots exhibited a high efficiency of 13.5 %, surpassing that of the control devices.

Zang et al. [279] also reported fabrication of solar cells using Zinc doped $CsPbI_3$ QDs demonstrate better efficiency and stability compared to solar cells using pristine $CsPbI_3$ QDs, achieving a record PCE exceeding 16 %. The improved performance can be attributed to the lower density of defect states in the Zn:$CsPbI_3$ QDs and the reduced recombination of charges in the solar cell device. This research introduces novel concepts for developing highly efficient PQD solar cell devices by employing strategic material engineering techniques.

Shi et al. [280] utilized Yb-doped $CsPbI_3$ QDs with a doping level of 20 % to enhance PLQY, thermal stability, and carrier transport. These improved properties were then applied to design a solar cell device with a compositional structure of FTO/$TiO_2$/Yb-$CsPbI_3$ QDs/$PTB_7$/$MoO_3$/Ag. The resulting solar cell achieved a noteworthy PCE of 13.12 %.

Bi et al. [281] reported high performance solar cell based on stable $CsPb_{1-x}Zn_xI_3$ colloidal QDs with ultralow density of trap states by introducing $ZnCl_2$ into precursor solution. The addition of $ZnCl_2$ facilitates the occupation of iodide vacancies by $Cl^-$ ions, reducing non-radiative recombination in the QDs. This enhancement leads to the production of stable colloidal QDs with an extremely low trap density. The champion solar cell, based on $CsPb_{0.93}Zn_{0.07}I_3$ colloidal QDs, demonstrated a PCE approaching 15 % and these solar cells exhibited significantly improved stability under ambient conditions, even without the need for any encapsulation.

In 2020, Zhang and his research group [282] proposed a straightforward and effective method for enhancing the performance of $CsPbBr_3$ QD solar cells. The method involves the use of guanidinium thiocyanate (GASCN) salt to eliminate long-chain insulating ligands and passivate the QD surface during device fabrication. The resulting solar cells, employing PTAA or PTB7 as the hole transport layer, achieved impressive PCE of 5.01 % and 4.28 %, respectively. Notably, these $CsPbBr_3$ PQD solar cells exhibited remarkable stability, a high open-circuit voltage of 1.65 V, excellent transmittance beyond 500 nm, and a high CRI approaching 90 %. These advantageous characteristics are typically challenging to achieve in thin-film $CsPbBr_3$-based solar cells. The researchers anticipate that further advancements in the efficiency of $CsPbBr_3$ QD solar cells could enable their widespread use in applications such as solar windows for greenhouses and hydrogen generation facilitated by perovskite solar cells.

In the next year they have successfully developed a novel $CsPbI_3$ QD solar cell with a P/N homojunction structure [283]. This was the first time that n-type and p-type QDs were combined in this manner. By implementing the QD homojunction, a wide depletion region was formed within the active layer. This facilitated the rapid separation, transport, and extraction of carriers due to the enhanced built-in electric field, while also reducing carrier recombination. The resulting $CsPbI_3$ QD solar cell with the P/N homojunction exhibited exceptional tolerance to variations in thickness, surpassing both the control device and previously reported QD photovoltaics. Remarkably, a record-breaking PCE of 15.29 % was achieved, and the QD device consistently maintained high PCE values exceeding 12 %, even with an extremely thick active layer film measuring 1.2 μm.

In 2023, Lu et al. [284] introduced a humidity-assisted polymerization approach for the production of $CsPbI_3$ perovskite solar cells in ambient air, irrespective of humidity levels. They achieved this by incorporating a polymerizable additive called mercaptopropylme-methyldimethoxysilane (MMDS). During the formation of the $CsPbI_3$ film, the MMDS additive reacted with and consumed water present in the humid air. Subsequently, it underwent polymerization to form a water-resistant polymer, which effectively prevented further degradation caused by water. This innovative technique enabled the fabrication of perovskite solarcells with device efficiencies exceeding 18 % even in ambient air with relative humidity ranging from 40 % to 80 %.

Akin et al. [285] in their research, successfully obtained highly stable

perovskite solar cells with an impressive efficiency of up to 21 % using $CsPbX_3$ QDs. To enhance the performance of the device, the researchers incorporated a thin layer of mixed halide perovskite $CsPbBr_{1.85}I_{1.15}$ QDs as an interfacial layer. This layer effectively mitigated interfacial recombination by passivating defects near or at the perovskite/hole transport material interface. The wide bandgap of the QD layer acted as a barrier, reducing recombination and preventing the electron from flowing back into the hole transport layer. The solar cells demonstrated remarkable resistance to both humidity and light exposure, maintaining 91 % of their efficiency even after being subjected to these conditions for a continuous period of 30 days.

To enhance the stability and photovoltaic properties of $CsPbI_2Br$-based perovskite solar cells, Jinag and his research group [286] have employed a co-modification strategy involving the use of an ionic liquid (IL) 1-butyl-3-methylimidazolium tetrafluoroborate (BMIMBF4) and $CsPbBr_3$ QDs. The introduction of IL improved the particle size of the perovskite, effectively passivated defects, and extended the carrier lifetime in $CsPbI_2Br$ films. Additionally, the incorporation of an ultrathin $CsPbBr_3$ QD interlayer between the electron transport layer and the perovskite film acted as a barrier, preventing the ingress of water molecules and enhancing the moisture resistance and structural stability of the device. Through optimization, the $CsPbI_2Br$-IL/QD PSCs demonstrated remarkable durability, maintaining over 70 % of their initial PCE even after exposure to air for 60 h. This improved stability can be attributed to the chemical passivation provided by ILs and the vapor barrier effect of QDs.

Lin et al. [287] introduced black phosphorus QDs (BPQDs) as an effective interfacial modification layer in all-inorganic perovskite solar cells. The utilization of BPQDs in all-inorganic perovskite solar cells serves to mitigate non radiative recombination losses and enhance electron extraction efficiency. The incorporation of BPQDs in $CsPbI_2Br$-based devices has led to the achievement of a notable PCE of up to 12.2 %. It is worth noting that such high-efficiency $CsPbI_2Br$-based Perovskite solar cells, which undergo full low-temperature processing, are relatively uncommon in the field.

Qi et al. [288] have developed a strategic interfacial modulation technique to enhance the performance of carbon-based $CsPbIBr_2$ planar solar cells. By incorporating PbS QDs as an interfacial layer, they achieved significant improvements in the solar cell performance through three distinct roles: enhancing the crystallization quality of $CsPbIBr_2$, reducing charge recombination, and facilitating carrier transfer at the interface. This interfacial modification resulted in a remarkable boost in the conversion efficiency, increasing it from 7.00 % to 9.09 %. These findings contribute to the development of efficient and stable inorganic perovskite solar cells, with the potential for reproducibility and scalability advancements.

In their study, Hoffman et al. [289] observed an improvement in the PCE of QD based solar cells compared to those without QDs. The researchers synthesized lead-free perovskite $CsSnBr_2I$ quantum dots with adjustable bandgaps by manipulating the ratio of Br to I. Subsequently, these QDs were utilized as a layer at the interface to facilitate hole extraction in perovskite solar cells based on $CsPbBr_3$ resulting in a PCE of 9.13 %.

### 7.3. Application in nano lasers

Quantum dot lasers, known as the third generation of semiconductor lasers, have garnered significant attention due to their distinct properties. A laser is an optical amplification device that consists of three main components: a gain medium, a pump source, and optical resonators. The gain medium is a controlled material that amplifies the pump beam through stimulated emission. In a simplified three-level optical-gain model, electrons are excited to a higher energy state, resulting in population inversion. When the pump energy exceeds the bandgap energy, stimulated emission occurs, leading to amplified emission. In a laser cavity, emitted photons are reflected and amplified as they pass through the gain medium, generating laser action (Fig. 13 a,b). As we discussed earlier, with the help of three-dimensional quantum confinement, QDs have well-defined densities of states and powerful oscillation capabilities, resulting in emission wavelengths that can be adjusted according to their size. These attributes make QDs highly suitable for efficient lasing with low thresholds and insensitivity to temperature, while also providing an optimal nanoresonator cavity. PQDs have been recognized as low-threshold, temperature-insensitive gain media and ideal resonator cavities for high-performance lasers. Amplified spontaneous emission was observed in $CsPbX_3$ PQDs, and subsequent demonstrations showed wavelength-tunable random lasers. PQD lasers operate in whispering-gallery (W-G) mode and Fabry-Pérot (F–P) mode. W-G mode lasers use concave surfaces or microspheres as optical resonant cavities, while F–P cavities consist of parallel mirrors and a gain medium. Researchers have achieved single-mode lasing and improved stability by modifying ligands, controlling nucleation processes, and optimizing resonant cavities. PQD lasers have shown promising applications, including vertical cavity surface emitting lasers (VCSELs) with low thresholds and stable device operation. PQDs, including $CsPbX_3$, have emerged as promising candidates for laser applications, serves as an excellent gain material, offering a comparably low threshold and enhanced stability for stimulated emission. In contrast, conventional PQDs like $MAPbX_3$ suffer from unstable electrical properties when exposed to air. Additionally, the accumulation of heat during lasing leads to changes in the properties of PQDs. These challenges make it challenging to operate lasing processes in a normal air environment at room temperature. To overcome these issues, the $CsPbX_3$ quantum dot group has been introduced, demonstrating notable advantages such as tunable wavelength, low threshold, and stability in typical air environments [290].

Zhou et al. [98] developed a single-mode laser with a quality factor Q of 3000 by depositing $CsPbX_3$ PQDs on individual submicron ZnO rods. By adjusting the size of the microcavity, they were able to produce single-mode lasing throughout the whole visible spectrum (Fig. 13 d,e & f). To create random lasers, Kovalenko et al. [292] coated $CsPbX_3$ PQDs on spherical microresonators (Fig. 13 g). A VCSEL with a low threshold of 9 $\mu Jcm^{-2}$ was created by Wang et al. [293] utilizing $CsPbBr_3$ PQDs and highly reflecting distributed Bragg reflectors (DBRs). Later, Huang et al. [95] developed a $CsPbBr_3$ PQD VCSEL with well-designed resonant cavities, reaching an ultra-low laser threshold of 0.39 $\mu Jcm^{-2}$, as well as stable device performance over 5 h/1.8 $\times$ $10^7$ optical pulse excitations in ambient circumstances shown in Fig. 5 h & i.

Zhang et al. [294] developed $CsPbX_3$ QD glasses with the potential for stable, flexible, and adjustable multi-colour laser materials. They cover a wide range of adjustable optical performance and achieve upconversion emissions across the visible spectra. Detailed investigations into their two-photon absorption mechanism were conducted, and narrowing of emission spectra was observed at lower temperatures. The $CsPbCl_{1.5}Br_{1.5}$ QD glass, with the largest exciton binding energy, shows promise for achieving amplified spontaneous emission and future lasing applications.

In the realm of laser applications, Wang et al. [295] presented a novel approach involving the manipulation of photoluminescence in metal halide $CsPbX_3$ PQDs (green $CsPbBr_3$ and red $CsPbBr_{1.5}I_{1.5}$) embedded within a glass medium. This manipulation is achieved by real-time tuning of local temperature fields, facilitated by the efficient photothermal material $CsYb_2F_7$@glass. Leveraging the protective nature of the inorganic glass matrix and the low exciton binding energy of PQDs, they successfully achieved stable and reversible full-spectral emissions of PQDs through ON/OFF control, triggered by stimulation from a commercially available 980 nm laser.

In a study by Wang et al. [296], they synthesized small-sized $CsPbBr_3$ QDs of approximately 9 nm and demonstrated remarkable properties of low-threshold, wavelength-tunable, and highly stable stimulated emission at room temperature, even in the presence of atmospheric conditions. The stimulation mechanism was attributed to the presence of

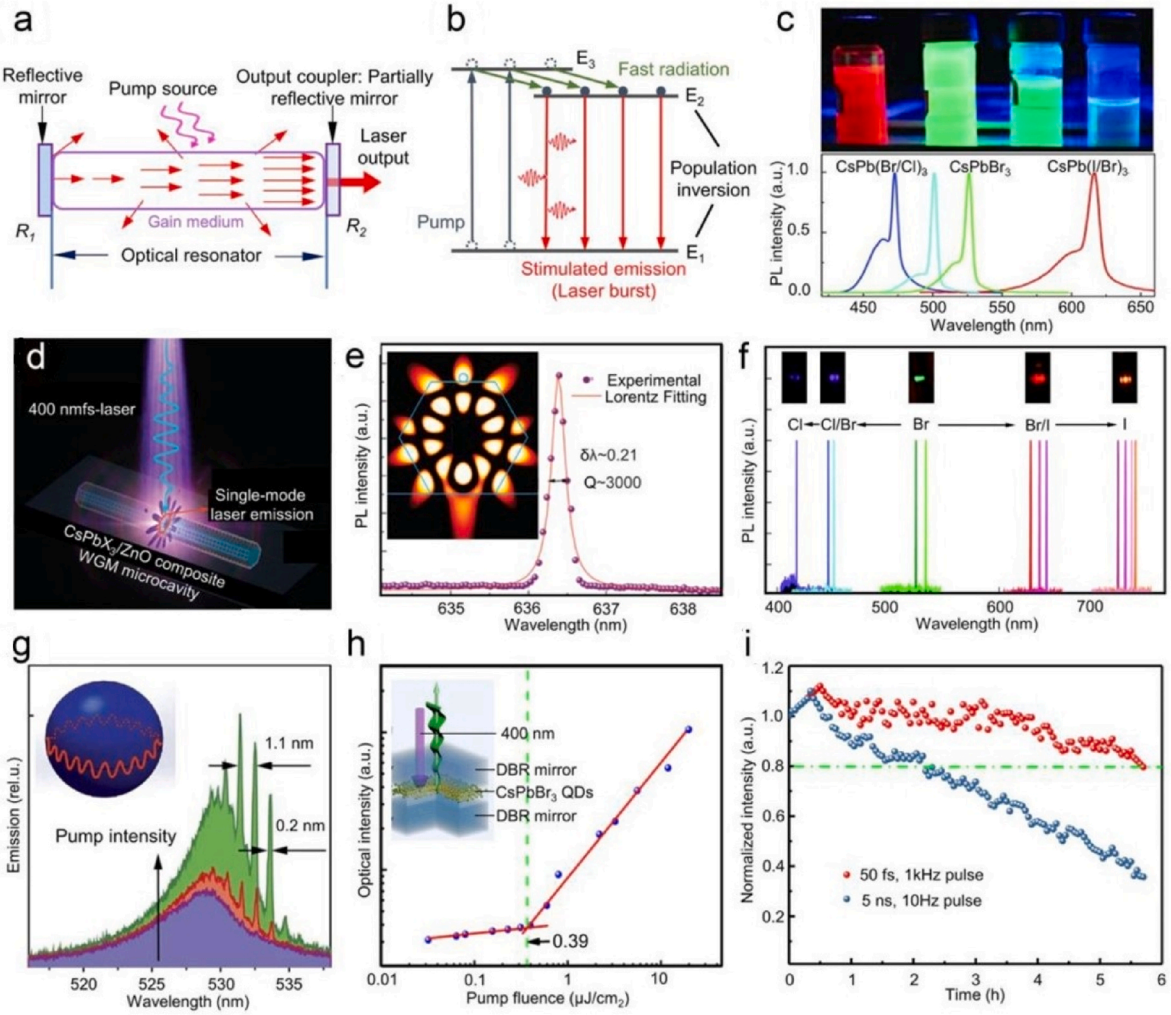


**Fig. 13.** A schematic diagram representing a) device structure for lasers b) population inversion in lasers c) Stimulated PL emission of $CsPb(Br/Cl)_3$, $CsPbBr_3$, and $CsPb(I/Br)_3$ PQDs with corresponding images (upper) d) Gallery mode (WGM) microcavity based on a composite of $CsPb(Br_{0.5}I_{0.5})_3$ PQDs and ZnO. The microcavity is pumped with a femtosecond laser at a wavelength of 400 nm, and it is placed on a silicon substrate. e) Lorentz fitting of a laser oscillation mode with an inset image of a numerical simulation on the standing wave field distributions of a composite microcavity made of $CsPb(Br_{0.5}I_{0.5})_3$ PQDs and ZnO. f) $CsPbX_3$ PQDs single-mode lasers with a broad wavelength tuning range, 417–723 nm. The photos in the insets show the PL emission from a single $CsPbX_3$ PQDs/ZnO composite microcavity. g) A 15 mm-diameter microsphere resonator with a $CsPbBr_3$ PQD film on top evolved from PL to WGM lasing with increasing pump intensity. h) The output intensity vs the input pump fluence with a schematic representation (inset) of a $CsPbBr_3$ PQD VCSEL displaying lasing with a threshold of 0.39 μJ/cm$^2$. i) Measurements of the $CsPbBr_3$ PQD VCSEL's stability under 50 fs and 5 ns pulsed stimulation at ambient temperature adopted from Ref. [291] with open access under **CC BY-NC-ND 4.0**.

biexcitons with a high binding energy, while the physical cause of the stimulated emission was associated with a combination of low threshold, high PLQY, large absorption cross-section, and a significant shift in the emission peak (known as Stokes shift) [297]. The researchers also achieved the ability to tune the wavelength of the stimulated emission across the entire visible spectrum by manipulating the size of the QDs or adjusting the compositional stoichiometry. Notably, the stimulated emission intensity remained at 90 % of its initial value even after subjecting the $CsPbBr_3$ QDs to an exceptionally high number of laser shots ($1.6 \times 10^7$), indicating their exceptional photostability.

Hsieh et al. [298] conducted an experiment where they achieved continuous-wave lasing from a single $CsPbBr_3$ QD within a plasmonic gap-mode nanocavity. They observed a remarkably low lasing threshold of 1.9 $Wcm^{-2}$ at a temperature of 120 K. The nanocavity's ultrasmall volume (0.002 $\lambda^3$) contributed to an enhanced interaction between light and matter, enabling efficient nanolasing. This successful demonstration of a $CsPbBr_3$ single QD nanolaser presents a promising approach for implementing lasing in highly compact on-chip optoelectronic devices. In another study by Tang et al. [299], they investigated the fluorescence properties of single $CsPbX_3$ QDs synthesized using the HI method. The researchers found that these QDs exhibited amplified stimulated emission with superior optical gain and a low laser threshold. Additionally, by modifying the pumping configuration, the authors also observed random lasing behaviour in the $CsPbX_3$ QDs. Furthermore, Zhang et al. [300] reported the occurrence of random lasing in $CsPbBr_3$ QDs prepared via the hot injection method under ambient conditions. Their findings align with previous research, highlighting the potential of $CsPbBr_3$ QDs for random lasing applications. Summary of lasers lased on the $CsPbX_3$ QDs is shown in Table 7.

### 7.4. Application in electronics

Perovskite-based field-effect transistors (FETs) and light-stimulated neuromorphic devices have recently garnered significant attention in the scientific community due to their remarkable characteristics, including the ability to tune the bandgap, shallow defect levels, ambipolar charge transport, and rapid ion migration. FETs are widely used electronic devices consisting of three terminals: the source, drain, and gate. In the context of inorganic PQDs, they are often employed as the charge transport channel layer in FETs, which function as voltage-

**Table: 7**
summary of lasers based on $CsPbX_3$ QDs.

| Material | Cavity type | Pump source (Wavelength, repetition rate, pulse width) | Threshold (ASE or lasing) | Temperature | Reference |
|---|---|---|---|---|---|
| $CsPbBr_3$ | Random | 400 nm, 250 fs?75 KHz | 65 μJ/cm$^2$ | Room temperature | [94] |
| $CsPbBr_3$ | VCSEL | 400 nm, 50 fs, 1 KHz | 0.39 μJ/cm$^2$ | Room temperature | [95] |
| $CsPbBr_3$ | Random | 400 nm, 100 fs?1 KHz | 0.97 μJ/cm$^2$ | Room temperature | [96] |
| $CsPbBr_3$ | WGM | 800 nm, 50 fs, 1 KHz | 88.49 μJ/cm$^2$ | Room temperature | [97] |
| $CsPb(Br_{0.5}I_{0.5})_3$ | WGM | 400 nm, 40 fs, 10 KHz | 11.7 μJ/cm$^2$ | 77 K | [98] |
| $CsPbBr_3$ | Random | 800 nm, 1 kHz, pulse width: 130 fs | 471 μJ/cm$^2$ | Room temperature | [99] |
| $CsPbBr_3$ | Gap plsmon nano cavity | 400 nm, 100 fs ,80 MHz | 1.9 W/cm$^2$ | 120 K | [100] |
| $CsPbBr_3$ | Random | 498 nm, 800fs | 0.138 μJ/cm$^2$ | – | [101] |
| $CsPbBr_3$ | WGM | 800 nm, 35 fs, 1 KHz | 430 μJ/cm$^2$ | Room temperature | [102] |
| $CsPbBr_3$ | – | 5 nm, 70–80ps, 15 Hz | 22.25 μJ/cm$^2$ | Room temperature | [103] |
| $CsPbCl_3$ | WGM | – | 11.5 μJ/cm$^2$ | Room temperature | [104] |

controlled electrical switches. In this configuration, the source and drain electrodes are directly in contact with the perovskite layer, while the gate electrode is separated by a dielectric layer. By applying a voltage bias to the gate, the current flow between the source and drain can be reversibly controlled, thereby modulating the conductivity of the perovskite layer. Initially, the incorporation of inorganic PQDs with organic semiconductors is commonly practiced to enhance charge separation efficiency and achieve high photoresponsivity [301]. In 2017, Chen et al. [302] fabricated a top contact/bottom gate (TC/BG) FET using a thin film that combined $CsPbBr_3$ QDs with dinaphtho-[2,3-b:2′, 3′-f]thieno [3,2-b]thiophen (DNTT). The device demonstrated a high photoresponsivity of $1.7 \times 10^4$ A $W^{-1}$ and an ON/OFF ratio of $8.1 \times 10^4$. These hybrid phototransistors, combining inorganic PQDs with organic semiconductors, showcased remarkable stability even after 100 days of storage in ambient air. Furthermore, $CsPbBr_3$ QDs were room temperature doped with $Ag^+$ and used in FETs by Zhou et al. [303]. This study proposed that the Fermi level drops down to the valence band to create a p-type character when $Ag^+$ partially substitutes $Pb^{2+}$ in $CsPbBr_3$ QDs. Hence, compared to its undoped counterpart, the $Ag^+$-doped $CsPbBr_3$ QDs-based FET displayed a three-order improvement in hole mobility, which was attributed to phonon screening and suppressed ion transportation. For the achievement of robust neuromorphic computing with simple device integration and low energy consumption, artificial synaptic devices incorporating several excitation modes have recently attracted significant interest. As a result, $CsPbBr_3$ QD-based optoelectronic synaptic transistors were created [304]. As the light-absorbing and charge transport layer of the light-simulated synaptic transistors, Wang et al. [305] reported on a solution approach to blend $CsPbBr_3$ QDs with poly (3,3-didodecylquarterthiophene) (PQT-12) in early 2019. For computing inspired by the human brain, Periyal et al. [306] created a sensitive neuromorphic transistor employing an amorphous indium gallium zinc oxide (IGZO) semiconductor and $CsPbBr_3$ QDs as the active material. This transistor responds to light inputs at wavelengths of 445 nm and 525 nm and enables near-linear programming, a feature required for deep learning accelerators in artificial neural networks.

In recent years, the speed of memory has lagged behind the rapidly increasing processing speed, leading to a phenomenon known as the "Memory Wall". To address this issue, new device architectures such as resistive switching random access memory (RRAM) with faster switching speed and lower energy consumption compared to present solid-state storage technologies have been developed. Due to their abundance of low formation energy ionic point defects like interstitials, substitutions, and vacancies, PQDs are suited for RRAM applications. RRAM also called memristor, including inorganic PQDs as the active layer, offers excellent scalability, easy fabrication, long data retention, and nanosecond speed. It operates based on reversible resistance switching between high and low states using external voltages. This technology shows promise for applications in neuromorphic systems, logic operations, and data storage, providing a potential solution to bridge the gap between memory performance and processor speed [80–85].

An ITO/PMMA/$CsPbBr_3$ QDs/PMMA/Ag structured RRAM device was fabricated by Wang's group [307–313] using $CsPbBr_3$ QDs as the active layer. Here, the migration of Ag ions and Br defects in QDs is caused by the external electric field and light irradiation, which is linked to the production and annihilation of conductive flaments that result in resistive switching. In this work, the RRAM device also served as a "OR" logic gate, combining electric field and light as input signals. The scientists also discovered that increasing the light intensity might effectively lower the set/reset voltages. After the $CsPbBr_3$ QDs-based RRAM was connected with a p-channel transistor, an equivalent RRAM-gate FET flash memory was demonstrated. Chen et al. [314] developed a simplified sandwich structure for $CsPbX_3$-based RRAM using a solution-processed method. The resistive switching behaviour of this device is attributed to the formation and rupture of conducting filaments created by bromine vacancies under an electric field. The memory device exhibited light-assisted multilevel storage, with a long data retention time of 1000 s and high reproducibility. It achieved an impressive ON/OFF ratio of approximately $10^7$ with a low reading voltage of −0.3 V. Another interesting advancement is the work of Yen et al. [315], who demonstrated an $CsPbX_3$ QD light-emitting memory (LEM). Their single device, consisting of Ag/PMMA/$CsPbBr_3$ QDs/ITO, can switch between RRAM and a light-emitting electrochemical cell on a sub-millisecond scale by modulating its bias polarity. The RRAM function enables electrical reading of encoded data, while the light-emitting memory function allows for parallel, non-contact optical reading at a speed of 5 kHz.

### 7.5. *Application in scintillation and radiation imaging*

Since X-rays were discovered, many fields, including biomedicine, material science, and industrial production, have used X-ray imaging techniques for non-destructive detection. X-ray scintillators are capable of efficiently turning X-rays into visible light. With the advent of new optoelectronic devices, X-ray detectors coupled with different scintillators have improved X-ray imaging and tomography [316]. Metal halide perovskites have recently gained prominence as outstanding scintillating materials for ionizing high-quality X-ray imaging. These compounds feature elements with elevated atomic numbers, resulting in a high attenuation coefficient. Their exceptional optoelectronic properties, adaptable chemical composition, and straightforward, cost-effective fabrication processes collectively position them as the preferred material for scintillators [317]. Ma et al. successfully developed a glass-ceramic scintillator by incorporating Europium (Eu) into a $CsPbX_3$ QDs matrix, aiming to eliminate scintillation scattering and improve operational stability. The presence of Eu facilitated the crystallization of $CsPbBr_3$ QDs, resulting in their uniform distribution throughout the matrix and enabling high-resolution X-ray imaging at 15 line pairs per millimetre. $CsPbBr_3$: Eu glass-ceramic scintillators also demonstrated enhanced operational and environmental stability [318]. Lu et al. developed a room-temperature, solution-based method for crafting a self-assembled $CsPbBr_3$ scintillator film with uniform thickness, displaying a linear response ideal for X-ray photon conversion. The

film's stability in hard X-ray microtomography opens avenues for cost-effective and flexible X-ray detectors in three-dimensional high--resolution imaging for applications in biomedicine and material science. Furthermore, the created $CsPbBr_3$ film scintillator demonstrated notable Contrast-to-Noise Ratio (CNR) advantages, averaging 45 %, and a spatial resolution (SR) of at least 8.1 μm, underscoring its superiority over traditional P43 powder scintillators in commercial use [319]. Hu et al. reported the fabrication of a liquid scintillator comprising perovskite quantum dots (QDs), 2,5-diphenyloxazole (PPO), and the high-refractive index solvent α-bremnaphthalene. This design, featuring pixelated and thickness-adjustable scintillators, resulted in a $CsPbBr_3$ QDs/PPO liquid scintillator-based X-ray detector with a remarkable detection limit of 79.1 $\mu Gys^{-1}$ and a spatial resolution of 4.6 lp $mm^{-1}$. The detector exhibited excellent radiation tolerance (>34 h) and stability under ambient conditions (>160 h). The versatility of this strategy extended to other liquid scintillators, such as $CsPbCl_3$ QDs and Mn-doped $CsPbCl_3$ QDs. The combined attributes of high sensitivity, spatial resolution, stability, ease of fabrication and maintenance, and a reusable substrate matrix positioned these liquid scintillators as promising candidates for practical applications in X-ray medical imaging [320].

## 8. Summary and outlooks

The $CsPbX_3$ quantum dot stands as a remarkable nanomaterial with a well-defined structure and outstanding structural and optical properties. This review provides a comprehensive overview of the $CsPbX_3$ QDs, focusing on it's structure, synthesis methods, properties, various strategies for improving properties and current applications. $CsPbX_3$ QDs has shown great potential for commercialization, particularly in the fields of light-harvesting and energy transfer. However, there is still a lack of understanding regarding the fundamental aspects of crystal design, which hinders the development of stable PQDs. Unanswered questions about the stability, optical properties, and electronic behaviour of cesium lead halides need to be addressed through ongoing research to unlock the full potential of these materials.

Firstly, the toxicity of lead halide perovskite is a significant concern that must be addressed. The presence of lead, a heavy metal ion, poses risks to human health and the environment. To mitigate this issue, suitable encapsulation techniques are necessary to minimize the toxicity of lead halide perovskite. For instance, when the perovskite is encapsulated within a polymer, the lead concentration is reduced to levels comparable to tap water when exposed to moisture. An additional approach to address the toxicity concern is the advancement of lead-free halide perovskite materials, wherein non-toxic elements like Sn, Bi, Sb, Cu, and Ge can replace the hazardous lead component. Notably, the partial substitution method ensures that the QDs retain their original shape and optical properties, including the distinctive features of sharp absorption and emission. However, it is important to acknowledge that complete lead-free perovskites still encounter stability challenges in ambient environments, emphasizing the need for continued research to overcome these limitations.

Secondly, The instability of the internal structure poses a significant challenge to the commercialization of $CsPbX_3$ QDs. Commonly used capping ligands, such as OA and OLA, are removed during post-treatment processes, resulting in structural breakdown. Studies have shown that doping transition elements, lanthanides, and other metals within the perovskite lattice can enhance lattice stability under ambient air conditions, offering new possibilities for optoelectronic device applications. However, excessive doping may distort the crystal structure of perovskite materials. As we discussed, various approaches have been explored to improve the stability of perovskite. But still, the long-term structural instability of $CsPbX_3$ QDs in ambient environments remains a major hurdle.

The remarkable optical properties and quantum confinement effect displayed by $CsPbX_3$ QDs have paved the way for exciting advancements in lighting and photonic applications. It is anticipated that the scientific interest in pure-colour and white-light generation using $CsPbX_3$ will continue to grow, potentially leading to significant commercial opportunities. The combination of theoretical calculations and experimental studies in $CsPbX_3$ holds great promise for enhancing crystal synthesis techniques and optimizing device performance. While there is still a long way to go for all-inorganic perovskites since they have the potential to play crucial roles in photovoltaics and contribute to advancements in human well-being.

## CRediT authorship contribution statement

**Aryamol Stephen:** Writing – review & editing, Writing – original draft, Methodology, Investigation, Formal analysis, Data curation, Conceptualization. **A. Biju:** Supervision, Resources. **Sona C. P:** Validation, Investigation, Data curation. **Jayaram Peediyekkal:** Writing – review & editing, Supervision, Software, Resources.

## Declaration of competing interest

The authors declare that they have no known competing financial interests or personal relationships that could have appeared to influence the work reported in this paper.

## Data availability

Data will be made available on request.

## References

[1] Y. Shirasaki, G.J. Supran, M.G. Bawendi, V. Bulović, Emergence of colloidal quantum-dot light-emitting technologies, Nat. Photonics 7 (1) (Jan. 2013) 13–23, https://doi.org/10.1038/nphoton.2012.328.
[2] T. Miyasaka, Lead halide perovskites in thin film photovoltaics: background and perspectives, Bull. Chem. Soc. Jpn. 91 (7) (Jul. 2018) 1058–1068, https://doi.org/10.1246/bcsj.20180071.
[3] M. Irshad, et al., Photocatalysis and perovskite oxide-based materials: a remedy for a clean and sustainable future, RSC Adv. 12 (12) (2022) 7009–7039, https://doi.org/10.1039/D1RA08185C.
[4] J.G. Bednorz, K.A. Moller, Possible highT c superconductivity in the Ba?La?Cu?O system, Z. Phys. B Condens. Matter. 64 (2) (Jun. 1986) 189–193, https://doi.org/10.1007/BF01303701.
[5] V. Bansal, P. Poddar, A. Ahmad, M. Sastry, Room-temperature biosynthesis of ferroelectric barium titanate nanoparticles, J. Am. Chem. Soc. 128 (36) (Sep. 2006) 11958–11963, https://doi.org/10.1021/ja063011m.
[6] S. Jin, T.H. Tiefel, M. McCormack, R.A. Fastnacht, R. Ramesh, L.H. Chen, Thousandfold change in resistivity in magnetoresistive La-Ca-Mn-O films, Science 264 (5157) (Apr. 1994) 413–415, https://doi.org/10.1126/science.264.5157.413.
[7] S. Ananthakumar, J.R. Kumar, S.M. Babu, Cesium lead halide ($CsPbX_3$, X = Cl, Br, I) perovskite quantum dots-synthesis, properties, and applications: a review of their present status, J. Photon. Energy 6 (4) (Oct. 2016) 042001, https://doi.org/10.1117/1.JPE.6.042001.
[8] L. Xu, S. Yuan, H. Zeng, J. Song, A comprehensive review of doping in perovskite nanocrystals/quantum dots: evolution of structure, electronics, optics, and light-emitting diodes, Mater. Today Nano 6 (Jun. 2019) 100036, https://doi.org/10.1016/j.mtnano.2019.100036.
[9] Q. Chen, et al., Under the spotlight: the organic–inorganic hybrid halide perovskite for optoelectronic applications, Nano Today 10 (3) (Jun. 2015) 355–396, https://doi.org/10.1016/j.nantod.2015.04.009.
[10] A. Swarnkar, R. Chulliyil, V.K. Ravi, M. Irfanullah, A. Chowdhury, A. Nag, Colloidal $CsPbBr_3$ perovskite nanocrystals: luminescence beyond traditional quantum dots, Angew. Chem. Int. Ed. 54 (51) (Dec. 2015) 15424–15428, https://doi.org/10.1002/anie.201508276.
[11] C.R. Kagan, D.B. Mitzi, C.D. Dimitrakopoulos, Organic-inorganic hybrid materials as semiconducting channels in thin-film field-effect transistors, Science 286 (5441) (Oct. 1999) 945–947, https://doi.org/10.1126/science.286.5441.945.
[12] S. Mei, et al., Facile synthesis and optical properties of CsPbX3/ZIF-8 composites for wide-color-gamut display, Nanomaterials 9 (6) (May 2019) 832, https://doi.org/10.3390/nano9060832.
[13] Q. Van Le, M. Park, W. Sohn, H.W. Jang, S.Y. Kim, Investigation of energy levels and crystal structures of cesium lead halides and their application in full-color light-emitting diodes, Adv. Electron. Mater. 3 (1) (Jan. 2017) 1600448, https://doi.org/10.1002/aelm.201600448.
[14] M.V. Kovalenko, L. Protesescu, M.I. Bodnarchuk, Properties and potential optoelectronic applications of lead halide perovskite nanocrystals, Science 358 (6364) (Nov. 2017) 745–750, https://doi.org/10.1126/science.aam7093.

[15] L. Protesescu, et al., Nanocrystals of cesium lead halide perovskites ($CsPbX_3$, X = Cl, Br, and I): novel optoelectronic materials showing bright emission with wide color gamut, Nano Lett. 15 (6) (Jun. 2015) 3692–3696, https://doi.org/10.1021/nl5048779.

[16] L. Protesescu, et al., Nanocrystals of cesium lead halide perovskites ($CsPbX_3$, X = Cl, Br, and I): novel optoelectronic materials showing bright emission with wide color gamut, Nano Lett. 15 (6) (Jun. 2015) 3692–3696, https://doi.org/10.1021/nl5048779.

[17] Y. Tong, et al., Highly luminescent cesium lead halide perovskite nanocrystals with tunable composition and thickness by ultrasonication, Angew. Chem. Int. Ed. 55 (44) (Oct. 2016) 13887–13892, https://doi.org/10.1002/anie.201605909.

[18] Y. Hu, S. Cao, P. Qiu, M. Yu, H. Wei, All–inorganic perovskite quantum dot–based blue light–emitting diodes: recent advances and strategies, Nanomaterials 12 (24) (Dec. 2022) 4372, https://doi.org/10.3390/nano12244372.

[19] X. Li, et al., $CsPbX_3$ quantum dots for lighting and displays: room-temperature synthesis, photoluminescence superiorities, underlying origins and white light-emitting diodes, Adv. Funct. Mater. 26 (15) (Apr. 2016) 2435–2445, https://doi.org/10.1002/adfm.201600109.

[20] A. Jana, M. Mittal, A. Singla, S. Sapra, Solvent-free, mechanochemical syntheses of bulk trihalide perovskites and their nanoparticles, Chem. Commun. 53 (21) (2017) 3046–3049, https://doi.org/10.1039/C7CC00666G.

[21] L. Protesescu, S. Yakunin, O. Nazarenko, D.N. Dirin, M.V. Kovalenko, Low-cost synthesis of highly luminescent colloidal lead halide perovskite nanocrystals by wet ball milling, ACS Appl. Nano Mater. 1 (3) (Mar. 2018) 1300–1308, https://doi.org/10.1021/acsanm.8b00038.

[22] F. Palazon, Y. El Ajjouri, P. Sebastia-Luna, S. Lauciello, L. Manna, H.J. Bolink, Mechanochemical synthesis of inorganic halide perovskites: evolution of phase-purity, morphology, and photoluminescence, J. Mater. Chem. C 7 (37) (2019) 11406–11410, https://doi.org/10.1039/C9TC03778K.

[23] A. Shinde, R. Gahlaut, S. Mahamuni, Low-temperature photoluminescence studies of $CsPbBr_3$ quantum dots, J. Phys. Chem. C 121 (27) (Jul. 2017) 14872–14878, https://doi.org/10.1021/acs.jpcc.7b02982.

[24] D. Yang, et al., Surface halogen compensation for robust performance enhancements of $CsPbX_3$ perovskite quantum dots, Adv. Opt. Mater. 7 (11) (Jun. 2019) 1900276, https://doi.org/10.1002/adom.201900276.

[25] R. Han, et al., Facile synthesis of CsPbX3 perovskite quantum dots via an open-air solution strategy, J. Electron. Mater. 52 (5) (May 2023) 3173–3179, https://doi.org/10.1007/s11664-023-10299-9.

[26] H. Gao, et al., Synthesis and photoluminescence properties of CsPbBr3 quantum dots by using para-xylene as the anti-solvent, J. Lumin. 215 (Nov. 2019) 116584, https://doi.org/10.1016/j.jlumin.2019.116584.

[27] G. Yuan, C. Ritchie, M. Ritter, S. Murphy, D.E. Gómez, P. Mulvaney, The degradation and blinking of single $CsPbI_3$ perovskite quantum dots, J. Phys. Chem. C 122 (25) (Jun. 2018) 13407–13415, https://doi.org/10.1021/acs.jpcc.7b11168.

[28] C. Bi, S. Wang, W. Wen, J. Yuan, G. Cao, J. Tian, Room-temperature construction of mixed-halide perovskite quantum dots with high photoluminescence quantum yield, J. Phys. Chem. C 122 (9) (Mar. 2018) 5151–5160, https://doi.org/10.1021/acs.jpcc.7b12607.

[29] H. Yang, et al., Blue emitting CsPbBr3 perovskite quantum dot inks obtained from sustained release tablets, Nano Res. 12 (12) (Dec. 2019) 3129–3134, https://doi.org/10.1007/s12274-019-2566-6.

[30] H. Yu, et al., Green light-emitting devices based on perovskite CsPbBr3 quantum dots, Front. Chem. 6 (2018) 381, https://doi.org/10.3389/fchem.2018.00381.

[31] Chen Tien, Lee, Tseng, Dong, Lin, High-quality all-inorganic perovskite CsPbBr3 quantum dots emitter prepared by a simple purified method and applications of light-emitting diodes, Energies 12 (18) (Sep. 2019) 3507, https://doi.org/10.3390/en12183507.

[32] S. Jung, et al., Enhancement of photoluminescence quantum yield and stability in CsPbBr3 perovskite quantum dots by trivalent doping, Nanomaterials 10 (4) (Apr. 2020) 710, https://doi.org/10.3390/nano10040710.

[33] B. Shu, et al., Highly efficient and blue-emitting $CsPbBr_3$ quantum dots synthesized by two-step supersaturated recrystallization, Nanotechnology 32 (14) (Apr. 2021) 145712, https://doi.org/10.1088/1361-6528/abcc21.

[34] H. Chen, A. Guo, J. Zhu, L. Cheng, Q. Wang, Tunable photoluminescence of CsPbBr3 perovskite quantum dots for their physical research, Appl. Surf. Sci. 465 (Jan. 2019) 656–664, https://doi.org/10.1016/j.apsusc.2018.08.211.

[35] Y. Kuang, et al., Regulated exciton dynamics and optical properties of single perovskite $CsPbBr_3$ quantum dots by diluting surface ligands, J. Phys. Chem. C 124 (43) (Oct. 2020) 23905–23912, https://doi.org/10.1021/acs.jpcc.0c05784.

[36] Y. Liu, et al., Considerably enhanced exciton emission of $CsPbCl_3$ perovskite quantum dots by the introduction of potassium and lanthanide ions, Nanoscale 10 (29) (2018) 14067–14072, https://doi.org/10.1039/C8NR03581D.

[37] W. Shi, Y. Zhao, C. Xie, P. Yang, Na-doping CsPbBr3 quantum dots prepared via ion exchange for bright and stable blue-to-red photoluminescence, J. Lumin. 233 (May 2021) 117886, https://doi.org/10.1016/j.jlumin.2021.117886.

[38] Y. Huang, et al., Sodium doping for enhanced performance by highly efficient $CsPbBr_3$ quantum dot-based electroluminescent light-emitting diodes, J. Mater. Chem. C 10 (10) (2022) 3729–3737, https://doi.org/10.1039/D1TC05997A.

[39] Z. Zhao, et al., Enhancing the exciton emission of CsPbCl3 perovskite quantum dots by incorporation of Rb+ ions, Mater. Res. Bull. 112 (Apr. 2019) 142–146, https://doi.org/10.1016/j.materresbull.2018.12.004.

[40] D. Yan, Q. Mo, S. Zhao, W. Cai, Z. Zang, Room temperature synthesis of $Sn^{2+}$ doped highly luminescent $CsPbBr_3$ quantum dots for high CRI white light-emitting diodes, Nanoscale 13 (21) (2021) 9740–9746, https://doi.org/10.1039/D1NR01492G.

[41] C. Bi, S. Wang, Q. Li, S.V. Kershaw, J. Tian, A.L. Rogach, Thermally stable copper (II)-Doped cesium lead halide perovskite quantum dots with strong blue emission, J. Phys. Chem. Lett. 10 (5) (Mar. 2019) 943–952, https://doi.org/10.1021/acs.jpclett.9b00290.

[42] W. Wang, S. Song, P. Lv, J. Li, B. Cao, Z. Liu, Thermally stable rare-earth Eu3+-doped CsPbCl3 perovskite quantum dots with controllable blue emission, J. Lumin. 260 (Aug. 2023) 119894, https://doi.org/10.1016/j.jlumin.2023.119894.

[43] X. Jing, et al., Enhanced photoluminescence and photoresponsiveness of $Eu^{3+}$ ions-doped $CsPbCl_3$ perovskite quantum dots under high pressure, Adv. Funct. Mater. 31 (31) (Aug. 2021) 2100930, https://doi.org/10.1002/adfm.202100930.

[44] S. Zhao, Y. Zhang, Z. Zang, Room-temperature doping of ytterbium into efficient near-infrared emission $CsPbBr_{1.5}Cl_{1.5}$ perovskite quantum dots, Chem. Commun. 56 (43) (2020) 5811–5814, https://doi.org/10.1039/D0CC01193B.

[45] Y. Xie, et al., Highly efficient blue-emitting $CsPbBr_3$ perovskite nanocrystals through neodymium doping, Adv. Sci. 7 (20) (Oct. 2020) 2001698, https://doi.org/10.1002/advs.202001698.

[46] Y. Hu, X. Zhang, C. Yang, J. Li, L. Wang, $Fe^{2+}$ doped in $CsPbCl_3$ perovskite nanocrystals: impact on the luminescence and magnetic properties, RSC Adv. 9 (57) (2019) 33017–33022, https://doi.org/10.1039/C9RA07069A.

[47] H. Yang, et al., Enhancing the light-emitting performance and stability in $CsPbBr_3$ perovskite quantum dots via simultaneous doping and surface passivation, J. Mater. Chem. C 8 (41) (2020) 14439–14445, https://doi.org/10.1039/D0TC03510F.

[48] C. Luo, W. Li, J. Fu, W. Yang, Constructing gradient energy levels to promote exciton energy transfer for photoluminescence controllability of all-inorganic perovskites and application in single-component WLEDs, Chem. Mater. 31 (15) (Aug. 2019) 5616–5624, https://doi.org/10.1021/acs.chemmater.9b01392.

[49] L. Zhu, C. Wu, S. Riaz, J. Dai, Stable silica coated DDAB-CsPbX3 quantum dots and their application for white light-emitting diodes, J. Lumin. 233 (May 2021) 117884, https://doi.org/10.1016/j.jlumin.2021.117884.

[50] Y. Li, X. Wang, W. Xue, W. Wang, W. Zhu, L. Zhao, Highly luminescent and stable CsPbBr3 perovskite quantum dots modified by phosphine ligands, Nano Res. 12 (4) (Apr. 2019) 785–789, https://doi.org/10.1007/s12274-019-2289-8.

[51] X. Li, et al., Highly stable CsPbBr3 quantum dots by silica-coating and ligand modification for white light-emitting diodes and visible light communication, Chem. Eng. J. 419 (Sep. 2021) 129551, https://doi.org/10.1016/j.cej.2021.129551.

[52] Z. Bao, W. Wang, H.-Y. Tsai, H.-C. Wang, S. Chen, R.-S. Liu, Photo-/electro-luminescence enhancement of $CsPbX_3$ (X = Cl, Br, or I) perovskite quantum dots via thiocyanate surface modification, J. Mater. Chem. C 8 (3) (2020) 1065–1071, https://doi.org/10.1039/C9TC05448K.

[53] P.-L. Chu, W.-L. Huang, S.-Y. Chu, Passivation of surface defects by X-type short-chain ligands for high quantum yield and stable $CsPbX_3$ quantum dots synthesis and application in WLEDs, ACS Appl. Opt. Mater. 1 (1) (Jan. 2023) 513–522, https://doi.org/10.1021/acsaom.2c00151.

[54] K.A. Huynh, et al., Ligand-assisted sulfide surface treatment of $CsPbI_3$ perovskite quantum dots to increase photoluminescence and recovery, ACS Photonics 8 (7) (Jul. 2021) 1979–1987, https://doi.org/10.1021/acsphotonics.0c01952.

[55] Y. Wang, et al., Surface ligand management aided by a secondary amine enables increased synthesis yield of $CsPbI_3$ perovskite quantum dots and high photovoltaic performance, Adv. Mater. 32 (32) (Aug. 2020) 2000449, https://doi.org/10.1002/adma.202000449.

[56] C. Bi, S.V. Kershaw, A.L. Rogach, J. Tian, Improved stability and photodetector performance of $CsPbI_3$ perovskite quantum dots by ligand exchange with aminoethanethiol, Adv. Funct. Mater. 29 (29) (Jul. 2019) 1902446, https://doi.org/10.1002/adfm.201902446.

[57] K. He, et al., Stable luminescent $CsPbI_3$ quantum dots passivated by (3-aminopropyl)triethoxysilane, Langmuir 36 (34) (Sep. 2020) 10210–10217, https://doi.org/10.1021/acs.langmuir.0c01688.

[58] M. Lu, et al., Surface ligand engineering-assisted CsPbI3 quantum dots enable bright and efficient red light-emitting diodes with a top-emitting structure, Chem. Eng. J. 404 (Jan. 2021) 126563, https://doi.org/10.1016/j.cej.2020.126563.

[59] P. Xiong, Y. Gong, X. Yang, Y. Zhu, C. Chen, J. Shen, Effect of hydrophobic silica aerogels in-situ on encapsulation the stability of CsPbBr3 quantum dots for white light-emitting diodes, J. Alloys Compd. 938 (Mar. 2023) 168541, https://doi.org/10.1016/j.jallcom.2022.168541.

[60] X. Wu, K. Yin, M. Yang, Y. Hu, H. Peng, Green synthesis of highly luminescent $CsPbBr_3$ quantum dots through silica coating and post-treatment with ligands, Flex. Print. Electron. 8 (3) (Sep. 2023) 035008, https://doi.org/10.1088/2058-8585/acedbe.

[61] H. Won, J.-H. Kim, J. Jung, D.-H. Kim, A comparative study on the optical and structural degradation behaviors and enhanced stability of CsPbBr3 embedded in oxide barriers, Solid State Sci. 136 (Feb. 2023) 107087, https://doi.org/10.1016/j.solidstatesciences.2022.107087.

[62] Z. Pan, et al., Highly stable CsPbI3 perovskite quantum dots enabled by single SiO2 coating toward down-conversion light-emitting diodes, Appl. Sci. 13 (13) (Jun. 2023) 7529, https://doi.org/10.3390/app13137529.

[63] Q. Mo, et al., Room temperature synthesis of stable silica-coated $CsPbBr_3$ quantum dots for amplified spontaneous emission, Photon. Res. 8 (10) (Oct. 2020) 1605, https://doi.org/10.1364/PRJ.399845.

[64] C. Zhang, et al., Exciton photoluminescence of $CsPbBr_3$ @$SiO_2$ quantum dots and its application as a phosphor material in light-emitting devices, Opt. Mater. Express 10 (4) (Apr. 2020) 1007, https://doi.org/10.1364/OME.389847.

[65] H. Li, et al., Core-shell structuredCsPbBr3/Sn-TiO2 nanocrystals for visible-light-driven photocatalyst in aqueous solution, Appl. Surf. Sci. 599 (Oct. 2022) 153937, https://doi.org/10.1016/j.apsusc.2022.153937.

[66] P. Nuket, Y. Akaishi, G. Yoshimura, T. Kida, P. Vas-Umnuay, In-situ TiO2-Coated CsPbBr3 quantum dots with enhanced stability, photoluminescence quantum yields, and charge transport properties, Ceram. Int. 48 (21) (Nov. 2022) 32504–32512, https://doi.org/10.1016/j.ceramint.2022.07.196.

[67] W. Chen, et al., Enhanced stability and tunable photoluminescence in perovskite $CsPbX_3$/ZnS quantum dot heterostructure, Small 13 (21) (Jun. 2017) 1604085, https://doi.org/10.1002/smll.201604085.

[68] H. Wang, et al., Mesoporous silica particles integrated with all-inorganic $CsPbBr_3$ perovskite quantum-dot nanocomposites (MP-PQDs) with high stability and wide color gamut used for backlight display, Angew. Chem. Int. Ed. 55 (28) (Jul. 2016) 7924–7929, https://doi.org/10.1002/anie.201603698.

[69] Y. Chen, Z.Y. Zhang, G.P. Wang, Perovskite quantum-dot-doped PMMA matrix enables natural light anticounterfeiting and passive displays, ACS Appl. Nano Mater. 6 (22) (Nov. 2023) 21037–21047, https://doi.org/10.1021/acsanm.3c03979.

[70] W. Liu, et al., Luminescence, stability, and applications of CsPbBr3 quantum dot/polymethyl methacrylate composites prepared by a solvent- and ligand-free ball milling method, Opt. Mater. 136 (Feb. 2023) 113398, https://doi.org/10.1016/j.optmat.2022.113398.

[71] J. Wang, et al., Improvement of the stability and optical properties of CsPbBr3 QDs, Nanomaterials 13 (16) (Aug. 2023) 2372, https://doi.org/10.3390/nano13162372.

[72] S.M.H. Qaid, H.M. Ghaithan, K.K. AlHarbi, B.A. Al-Asbahi, A.S. Aldwayyan, Enhancement of light amplification of CsPbBr3 perovskite quantum dot films via surface encapsulation by PMMA polymer, Polymers 13 (15) (Aug. 2021) 2574, https://doi.org/10.3390/polym13152574.

[73] Z. Zhang, et al., Encapsulation of CsPbBr3 perovskite quantum dots into PPy conducting polymer: exceptional water stability and enhanced charge transport property, Appl. Surf. Sci. 526 (Oct. 2020) 146735, https://doi.org/10.1016/j.apsusc.2020.146735.

[74] Z. Wang, et al., One-step polymeric melt encapsulation method to prepare $CsPbBr_3$ perovskite quantum dots/polymethyl methacrylate composite with high performance, Adv. Funct. Mater. 31 (22) (May 2021) 2010009, https://doi.org/10.1002/adfm.202010009.

[75] H. Li, et al., In-situ reacted multiple-anchoring ligands to produce highly photo-thermal resistant CsPbI3 quantum dots for display backlights, Chem. Eng. J. 454 (Feb. 2023) 140038, https://doi.org/10.1016/j.cej.2022.140038.

[76] J. Zhu, et al., Highly efficient and stable inorganic perovskite quantum dots by embedding into a polymer matrix, ChemNanoMat 5 (3) (Mar. 2019) 346–351, https://doi.org/10.1002/cnma.201800357.

[77] J. Zhang, G. Zhang, Y. Liao, Z. Pan, H. Rao, X. Zhong, Interfacial energy-level alignment via poly-3-hexylthiophene-CsPbI3 quantum dots hybrid hole conductor for efficient carbon-based CsPbI2Br solar cells, Chem. Eng. J. 453 (Feb. 2023) 139842, https://doi.org/10.1016/j.cej.2022.139842.

[78] P. Lu, et al., Bright and spectrally stable pure-red CsPb(Br/I)3 quantum dot LEDs realized by synchronous device structure and ligand engineering, Nano Energy 108 (Apr. 2023) 108208, https://doi.org/10.1016/j.nanoen.2023.108208.

[79] X. Zhou, et al., A and B sites dual substitution by Na+ and Cu2+ co-doping in CsPbBr3 quantum dots to achieve bright and stable blue light emitting diodes, Spectrochim. Acta. A. Mol. Biomol. Spectrosc. 300 (Nov. 2023) 122773, https://doi.org/10.1016/j.saa.2023.122773.

[80] C. Zhao, et al., Multifunctional short-chain 2-thiophenealkylammonium bromide ligand-assisted perovskite quantum dots for efficient light-emitting diodes, ACS Appl. Mater. Interfaces 15 (33) (Aug. 2023) 40080–40087, https://doi.org/10.1021/acsami.3c08008.

[81] H.J. Kwak, C. Kiguye, M. Gong, J.H. Park, G.-H. Kim, J.Y. Kim, Enhanced performance of inverted perovskite quantum dot light-emitting diode using electron suppression layer and surface morphology control, Materials 16 (22) (Nov. 2023) 7171, https://doi.org/10.3390/ma16227171.

[82] L. Yang, et al., Improving anion-exchange efficiency and spectrum stability of perovskite quantum dots via an $Al^{3+}$ bonding-doping synergistic effect, Nanoscale 15 (12) (2023) 5696–5704, https://doi.org/10.1039/D2NR07091J.

[83] Y.-Y. Zhao, et al., Improved performance of CsPbBr3 light-emitting diodes based on zinc bromide passivated quantum dots, Org. Electron. 116 (May 2023) 106775, https://doi.org/10.1016/j.orgel.2023.106775.

[84] L. Ma, et al., Bidentate oxalate ion enhancing water-resistant stability and exciton recombination behavior of blue CsPb(Br/Cl)3 quantum dots, Chem. Eng. J. 474 (Oct. 2023) 145732, https://doi.org/10.1016/j.cej.2023.145732.

[85] J. Wang, et al., Effective defect passivation of $CsPbBr_3$ quantum dots using gallium cations toward the fabrication of bright perovskite LEDs, J. Mater. Chem. C 9 (34) (2021) 11324–11330, https://doi.org/10.1039/D1TC01077H.

[86] X. Tang, J. Yang, S. Li, W. Chen, Z. Hu, J. Qiu, CsPbBr3/CdS core/shell structure quantum dots for inverted light-emitting diodes application, Front. Chem. 7 (Jul. 2019) 499, https://doi.org/10.3389/fchem.2019.00499.

[87] L. Gao, et al., High efficiency pure blue perovskite quantum dot light-emitting diodes based on formamidinium manipulating carrier dynamics and electron state filling, Light Sci. Appl. 11 (1) (Dec. 2022) 346, https://doi.org/10.1038/s41377-022-00992-5.

[88] H. Shao, et al., High brightness blue light-emitting diodes based on $CsPb(Cl/Br)_3$ perovskite QDs with phenethylammonium chloride passivation, Nanoscale 12 (21) (2020) 11728–11734, https://doi.org/10.1039/D0NR02597F.

[89] G. Pan, et al., Bright blue light emission of $Ni^{2+}$ ion-doped $CsPbCl_xBr_{3-x}$ perovskite quantum dots enabling efficient light-emitting devices, ACS Appl. Mater. Interfaces 12 (12) (Mar. 2020) 14195–14202, https://doi.org/10.1021/acsami.0c01074.

[90] X. Zhou, et al., Near-unity quantum yield and superior stable indium-doped $CsPbBr_xI_{3-x}$ perovskite quantum dots for pure red light-emitting diodes, Adv. Opt. Mater. 10 (2) (Jan. 2022) 2101517, https://doi.org/10.1002/adom.202101517.

[91] Y.-F. Lan, et al., Spectrally stable and efficient pure red $CsPbI_3$ quantum dot light-emitting diodes enabled by sequential ligand post-treatment strategy, Nano Lett. 21 (20) (Oct. 2021) 8756–8763, https://doi.org/10.1021/acs.nanolett.1c03011.

[92] L. Yang, B. Fu, X. Li, H. Chen, L. Li, Poly(vinylidene fluoride)-passivated $CsPbBr_3$ perovskite quantum dots with near-unity photoluminescence quantum yield and superior stability, J. Mater. Chem. C 9 (6) (2021) 1983–1991, https://doi.org/10.1039/D0TC05103A.

[93] Y.-H. Suh, T. Kim, J.W. Choi, C.-L. Lee, J. Park, High-performance $CsPbX_3$ perovskite quantum-dot light-emitting devices via solid-state ligand exchange, ACS Appl. Nano Mater. 1 (2) (Feb. 2018) 488–496, https://doi.org/10.1021/acsanm.7b00212.

[94] D. Xing, et al., Metallic nanowire coupled $CsPbBr_3$ quantum dots plasmonic nanolaser, Adv. Funct. Mater. 31 (28) (Jul. 2021) 2102375, https://doi.org/10.1002/adfm.202102375.

[95] C.-Y. Huang, et al., $CsPbBr_3$ perovskite quantum dot vertical cavity lasers with low threshold and high stability, ACS Photonics 4 (9) (Sep. 2017) 2281–2289, https://doi.org/10.1021/acsphotonics.7b00520.

[96] X. Tang, et al., Room temperature single-photon emission and lasing for all-inorganic colloidal perovskite quantum dots, Nano Energy 28 (Oct. 2016) 462–468, https://doi.org/10.1016/j.nanoen.2016.08.062.

[97] D. Yan, T. Shi, Z. Zang, S. Zhao, J. Du, Y. Leng, Stable and low-threshold whispering-gallery-mode lasing from modified CsPbBr3 perovskite quantum dots@SiO2 sphere, Chem. Eng. J. 401 (Dec. 2020) 126066, https://doi.org/10.1016/j.cej.2020.126066.

[98] C. Zhou, et al., Broad-band lead halide perovskite quantum dot single-mode lasers, J. Mater. Chem. C 8 (39) (2020) 13642–13647, https://doi.org/10.1039/D0TC02551H.

[99] T. Fan, J. Lü, Y. Chen, W. Yuan, Y. Huang, Random lasing in cesium lead bromine perovskite quantum dots film, J. Mater. Sci. Mater. Electron. 30 (2) (Jan. 2019) 1084–1088, https://doi.org/10.1007/s10854-018-0377-2.

[100] Y.-H. Hsieh, et al., Perovskite quantum dot lasing in a gap-plasmon nanocavity with ultralow threshold, ACS Nano 14 (9) (Sep. 2020) 11670–11676, https://doi.org/10.1021/acsnano.0c04224.

[101] H. Zhang, et al., Amplified spontaneous emission and random lasing using $CsPbBr_3$ quantum dot glass through controlling crystallization, Chem. Commun. 56 (19) (2020) 2853–2856, https://doi.org/10.1039/C9CC07676J.

[102] Z. Liu, et al., Stable and enhanced frequency up-converted lasing from $CsPbBr_3$ quantum dots embedded in silica sphere, Opt Express 27 (7) (Apr. 2019) 9459, https://doi.org/10.1364/OE.27.009459.

[103] S.M.H. Qaid, H.M. Ghaithan, B.A. Al-Asbahi, A. Alqasem, A.S. Aldwayyan, Fabrication of thin films from powdered cesium lead bromide ($CsPbBr_3$) perovskite quantum dots for coherent green light emission, ACS Omega 5 (46) (Nov. 2020) 30111–30122, https://doi.org/10.1021/acsomega.0c04517.

[104] L. Zhang, et al., Ultrafast antisolvent growth of single-crystalline $CsPbCl_3$ microcavity for low-threshold room temperature blue lasing, ACS Appl. Mater. Interfaces 14 (18) (May 2022) 21356–21362, https://doi.org/10.1021/acsami.2c02811.

[105] S. Karmakar, T.K. Das, N. Kalarikkal, A. Saha, A simplified approach for the aqueous synthesis of luminescent CdSe/ZnS core/shell quantum dots and their applications in ultrasensitive determination of the biomarker 3-nitro- l -tyrosine, Langmuir 38 (51) (Dec. 2022) 15995–16003, https://doi.org/10.1021/acs.langmuir.2c02459.

[106] H. Hao, H.-L. Hu, Y. Liu, F.-L. Jiang, Trioctylphosphine- and octanethiol-induced photoluminescence recovery of CdSe/ZnS quantum dots after dilution–quenching: implications for quantum dot films, ACS Appl. Nano Mater. 6 (4) (Feb. 2023) 3085–3094, https://doi.org/10.1021/acsanm.3c00200.

[107] C. Yang, et al., Efficient, stable, and photoluminescence intermittency-free CdSe-based quantum dots in the full-color range, ACS Photonics 8 (8) (Aug. 2021) 2538–2547, https://doi.org/10.1021/acsphotonics.1c00831.

[108] Z. Piao, et al., Recent advances in metal chalcogenide quantum dots: from material design to biomedical applications, Adv. Funct. Mater. 32 (44) (Oct. 2022) 2207662, https://doi.org/10.1002/adfm.202207662.

[109] C.-H. Lu, G.V. Biesold-McGee, Y. Liu, Z. Kang, Z. Lin, Doping and ion substitution in colloidal metal halide perovskite nanocrystals, Chem. Soc. Rev. 49 (14) (2020) 4953–5007, https://doi.org/10.1039/C9CS00790C.

[110] S.F. Hoefler, G. Trimmel, T. Rath, Progress on lead-free metal halide perovskites for photovoltaic applications: a review, Monatsh. Chem. - Chem. Mon. 148 (5) (May 2017) 795–826, https://doi.org/10.1007/s00706-017-1933-9.

[111] L. Xu, et al., Synthesis of stable and phase-adjustable $CsPbBr_3$ @$Cs_4PbBr_6$ nanocrystals via novel anion–cation reactions, Nanoscale Adv. 1 (3) (2019) 980–988, https://doi.org/10.1039/C8NA00291F.

[112] K. Surana, R.M. Mehra, B. Bhattacharya, H.-W. Rhee, A.R. Polu, P.K. Singh, A comprehensive study of chalcogenide quantum dot sensitized solar cells with a new solar cell exceeding 1 V output, Renew. Sustain. Energy Rev. 52 (Dec. 2015) 1083–1092, https://doi.org/10.1016/j.rser.2015.07.133.

[113] J. Khan, I. Ullah, J. Yuan, $CsPbI_3$ perovskite quantum dot solar cells: opportunities, progress and challenges, Mater. Adv. 3 (4) (2022) 1931–1952, https://doi.org/10.1039/D1MA01075A.

[114] J. Xu, R. Ouyang, X. Zhong, X. Fang, X. Xu, X. Wang, Alkali metal and alkaline earth metal perovskites for oxidative coupling of methane and oxidative

dehydrogenation of ethane, Mol. Catal. 547 (Aug. 2023) 113386, https://doi.org/10.1016/j.mcat.2023.113386.
[115] J.A. Flores-Livas, R. Sarmiento-Pérez, S. Botti, S. Goedecker, M.A.L. Marques, Rare-earth magnetic nitride perovskites, J. Phys. Mater. 2 (2) (Mar. 2019) 025003, https://doi.org/10.1088/2515-7639/ab083e.
[116] K. Hasnat, N. Kamel, D. Moudir, Y. Mouheb, S. Kamariz, A. Arabi, Ftir and Raman spectroscopic study of a complex perovskite: Ca $_{0.91-X}$ Ce $_{0.09}$ Rb $_{0.04}$ Cs $_{x}$ [(Zr $_{0.50}$ Ti $_{0.45}$)Al $_{0.05}$ ]O $_{3}$ , X=0.2 to 0.4, dedicated for radioactive waste confinement, Adv. Mater. Sci. 20 (2) (Jun. 2020) 81–94, https://doi.org/10.2478/adms-2020-0012.
[117] X. Xu, X. Wang, Perovskite nano-heterojunctions: synthesis, structures, properties, challenges, and prospects, Small Struct. 1 (1) (Oct. 2020) 2000009, https://doi.org/10.1002/sstr.202000009.
[118] X. Ren, et al., Perovskite quantum dots for emerging displays: recent progress and perspectives, Nanomaterials 12 (13) (Jun. 2022) 2243, https://doi.org/10.3390/nano12132243.
[119] C.-Y. Huang, et al., Inorganic halide perovskite quantum dots: a versatile nanomaterial platform for electronic applications, Nano-Micro Lett. 15 (1) (Dec. 2023) 16, https://doi.org/10.1007/s40820-022-00983-6.
[120] W. Travis, E.N.K. Glover, H. Bronstein, D.O. Scanlon, R.G. Palgrave, On the application of the tolerance factor to inorganic and hybrid halide perovskites: a revised system, Chem. Sci. 7 (7) (2016) 4548–4556, https://doi.org/10.1039/C5SC04845A.
[121] C.C. Stoumpos, M.G. Kanatzidis, The renaissance of halide perovskites and their evolution as emerging semiconductors, Acc. Chem. Res. 48 (10) (Oct. 2015) 2791–2802, https://doi.org/10.1021/acs.accounts.5b00229.
[122] Y. Fu, et al., Incorporating large A cations into lead iodide perovskite cages: relaxed Goldschmidt tolerance factor and impact on exciton–phonon interaction, ACS Cent. Sci. 5 (8) (Aug. 2019) 1377–1386, https://doi.org/10.1021/acscentsci.9b00367.
[123] Y. Zhao, C. Wang, X. Hu, J. Fan, Recent progress in CsPbX $_{3}$ perovskite nanocrystals for enhanced stability and photocatalytic applications, ChemNanoMat 7 (7) (Jul. 2021) 789–804, https://doi.org/10.1002/cnma.202100094.
[124] G.K. Grandhi, K. Mokurala, J.H. Han, H. Bin Cho, J.Y. Han, W.B. Im, Recent advances and challenges in obtaining stable CsPbX $_{3}$ (X = Cl, Br, and I) nanocrystals toward white light-emitting applications, ECS J. Solid State Sci. Technol. 10 (10) (Oct. 2021) 106001, https://doi.org/10.1149/2162-8777/ac28e4.
[125] M.A. Green, A. Ho-Baillie, H.J. Snaith, The emergence of perovskite solar cells, Nat. Photonics 8 (7) (Jul. 2014) 506–514, https://doi.org/10.1038/nphoton.2014.134.
[126] C. Li, X. Lu, W. Ding, L. Feng, Y. Gao, Z. Guo, Formability of ABX3 (X = F, Cl, Br, I) halide perovskites, Acta Crystallogr. B 64 (Pt 6) (Dec. 2008) 702–707, https://doi.org/10.1107/S0108768108032734.
[127] F. Ünlü, et al., Understanding the interplay of stability and efficiency in A-site engineered lead halide perovskites, Apl. Mater. 8 (7) (Jul. 2020) 070901, https://doi.org/10.1063/5.0011851.
[128] T. Miyasaka, A. Kulkarni, G.M. Kim, S. Öz, A.K. Jena, Perovskite solar cells: can we go organic-free, lead-free, and dopant-free? Adv. Energy Mater. 10 (13) (Apr. 2020) 1902500 https://doi.org/10.1002/aenm.201902500.
[129] R.J. Sutton, et al., Cubic or orthorhombic? Revealing the crystal structure of metastable black-phase CsPbI $_{3}$ by theory and experiment, ACS Energy Lett. 3 (8) (Aug. 2018) 1787–1794, https://doi.org/10.1021/acsenergylett.8b00672.
[130] S. Shahrokhi, et al., Anomalous structural evolution and glassy lattice in mixed-halide hybrid perovskites, Small 18 (21) (May 2022) 2200847, https://doi.org/10.1002/smll.202200847.
[131] N.A.N. Ouedraogo, et al., Stability of all-inorganic perovskite solar cells, Nano Energy 67 (Jan. 2020) 104249, https://doi.org/10.1016/j.nanoen.2019.104249.
[132] D.B. Straus, S. Guo, R.J. Cava, Kinetically stable single crystals of perovskite-phase CsPbI $_{3}$, J. Am. Chem. Soc. 141 (29) (Jul. 2019) 11435–11439, https://doi.org/10.1021/jacs.9b06055.
[133] S. Masi, A.F. Gualdrón-Reyes, I. Mora-Seró, Stabilization of black perovskite phase in FAPbI $_{3}$ and CsPbI $_{3}$, ACS Energy Lett. 5 (6) (Jun. 2020) 1974–1985, https://doi.org/10.1021/acsenergylett.0c00801.
[134] J. Chen, et al., Efficient and bright white light-emitting diodes based on single-layer heterophase halide perovskites, Nat. Photonics 15 (3) (Mar. 2021) 238–244, https://doi.org/10.1038/s41566-020-00743-1.
[135] C.C. Stoumpos, et al., Crystal growth of the perovskite semiconductor CsPbBr $_{3}$ : a new material for high-energy radiation detection, Cryst. Growth Des. 13 (7) (Jul. 2013) 2722–2727, https://doi.org/10.1021/cg400645t.
[136] Chr Kn, Møller, "crystal structure and photoconductivity of cæsium plumbohalides,", Nature 182 (4647) (Nov. 1958) https://doi.org/10.1038/1821436a0, 1436–1436.
[137] R.J. Sutton, et al., Bandgap-tunable cesium lead halide perovskites with high thermal stability for efficient solar cells, Adv. Energy Mater. 6 (8) (Apr. 2016) 1502458, https://doi.org/10.1002/aenm.201502458.
[138] M. Kulbak, D. Cahen, G. Hodes, How important is the organic part of lead halide perovskite photovoltaic cells? Efficient CsPbBr $_{3}$ cells, J. Phys. Chem. Lett. 6 (13) (Jul. 2015) 2452–2456, https://doi.org/10.1021/acs.jpclett.5b00968.
[139] J.-F. Liao, H.-S. Rao, B.-X. Chen, D.-B. Kuang, C.-Y. Su, Dimension engineering on cesium lead iodide for efficient and stable perovskite solar cells, J. Mater. Chem. A 5 (5) (2017) 2066–2072, https://doi.org/10.1039/C6TA09582H.
[140] G.E. Eperon, et al., Inorganic caesium lead iodide perovskite solar cells, J. Mater. Chem. A 3 (39) (2015) 19688–19695, https://doi.org/10.1039/C5TA06398A.
[141] W. Ahmad, J. Khan, G. Niu, J. Tang, Inorganic CsPbI $_{3}$ perovskite-based solar cells: a choice for a tandem device, Sol. RRL 1 (7) (Jul. 2017) 1700048, https://doi.org/10.1002/solr.201700048.
[142] Y. Hu, et al., Bismuth incorporation stabilized α-CsPbI $_{3}$ for fully inorganic perovskite solar cells, ACS Energy Lett. 2 (10) (Oct. 2017) 2219–2227, https://doi.org/10.1021/acsenergylett.7b00508.
[143] J. Shamsi, A.S. Urban, M. Imran, L. De Trizio, L. Manna, Metal halide perovskite nanocrystals: synthesis, post-synthesis modifications, and their optical properties, Chem. Rev. 119 (5) (Mar. 2019) 3296–3348, https://doi.org/10.1021/acs.chemrev.8b00644.
[144] C.B. Murray, D.J. Norris, M.G. Bawendi, Synthesis and characterization of nearly monodisperse CdE (E = sulfur, selenium, tellurium) semiconductor nanocrystallites, J. Am. Chem. Soc. 115 (19) (Sep. 1993) 8706–8715, https://doi.org/10.1021/ja00072a025.
[145] Y.-S. Park, S. Guo, N.S. Makarov, V.I. Klimov, Room temperature single-photon emission from individual perovskite quantum dots, ACS Nano 9 (10) (Oct. 2015) 10386–10393, https://doi.org/10.1021/acsnano.5b04584.
[146] J. Song, J. Li, X. Li, L. Xu, Y. Dong, H. Zeng, Quantum dot light-emitting diodes based on inorganic perovskite cesium lead halides (CsPbX3), Adv. Mater. (2015), https://doi.org/10.1002/ADMA.201502567.
[147] D. Yan, et al., Highly efficient emission and high-CRI warm white light-emitting diodes from ligand-modified CsPbBr$_3$ quantum dots, Opto-Electron. Adv. 5 (1) (2022), https://doi.org/10.29026/oea.2022.200075, 200075–200075.
[148] E. Hassanabadi, et al., Ligand & band gap engineering: tailoring the protocol synthesis for achieving high-quality CsPbI $_{3}$ quantum dots, Nanoscale 12 (26) (2020) 14194–14203, https://doi.org/10.1039/D0NR03180A.
[149] S. Thapa, et al., Long-term ambient air-stable cubic CsPbBr $_{3}$ perovskite quantum dots using molecular bromine, Nanoscale Adv. 1 (9) (2019) 3388–3391, https://doi.org/10.1039/C9NA00486F.
[150] Q. Zhang, Y. Yin, All-inorganic metal halide perovskite nanocrystals: opportunities and challenges, ACS Cent. Sci. 4 (6) (Jun. 2018) 668–679, https://doi.org/10.1021/acscentsci.8b00201.
[151] A.S. Sadhu, Y.-M. Huang, L.-Y. Chen, H.-C. Kuo, C.-C. Lin, Recent advances in colloidal quantum dots or perovskite quantum dots as a luminescent downshifting layer embedded on solar cells, Nanomaterials 12 (6) (Mar. 2022) 985, https://doi.org/10.3390/nano12060985.
[152] W. Zheng, et al., Near-infrared-triggered photon upconversion tuning in all-inorganic cesium lead halide perovskite quantum dots, Nat. Commun. 9 (1) (Aug. 2018) 3462, https://doi.org/10.1038/s41467-018-05947-2.
[153] B. Chaudhary, Y.K. Kshetri, H.-S. Kim, S.W. Lee, T.-H. Kim, Current status on synthesis, properties and applications of CsPbX $_{3}$ (X = Cl, Br, I) perovskite quantum dots/nanocrystals, Nanotechnology 32 (50) (Dec. 2021) 502007, https://doi.org/10.1088/1361-6528/ac2537.
[154] X. Xu, et al., Ultrasonication-assisted ambient-air synthesis of monodispersed blue-emitting CsPbBr $_{3}$ quantum dots for white light emission, ACS Appl. Nano Mater. 2 (11) (Nov. 2019) 6874–6879, https://doi.org/10.1021/acsanm.9b01315.
[155] K. Umemoto, et al., Separation of mono-dispersed CH $_{3}$ NH $_{3}$ PbBr $_{3}$ perovskite quantum dots via dissolution of nanocrystals, CrystEngComm 20 (44) (2018) 7053–7057, https://doi.org/10.1039/C8CE01239C.
[156] H. Shao, et al., Highly efficient and stable blue-emitting CsPbBr $_{3}$ @SiO $_{2}$ nanospheres through low temperature synthesis for nanoprinting and WLED, Nanotechnology 29 (28) (Jul. 2018) 285706, https://doi.org/10.1088/1361-6528/aac00b.
[157] J. De Roo, et al., Highly dynamic ligand binding and light absorption coefficient of cesium lead bromide perovskite nanocrystals, ACS Nano 10 (2) (Feb. 2016) 2071–2081, https://doi.org/10.1021/acsnano.5b06295.
[158] N. Oshita, et al., A facile reprecipitation method of Quantum-confined CsPbBr $_{3}$ perovskite quantum dots for narrow-band deep-blue emission, Appl. Phys. Express 15 (6) (Jun. 2022) 065002, https://doi.org/10.35848/1882-0786/ac6c19.
[159] K. Ma, et al., Stable and multicolor solid-state luminescence of Mn doped CsPb (Cl/Br)3 perovskite quantum dots and its application in light-emitting diodes, J. Lumin. 243 (Mar. 2022) 118622, https://doi.org/10.1016/j.jlumin.2021.118622.
[160] A. Jana, M. Mittal, A. Singla, S. Sapra, Solvent-free, mechanochemical syntheses of bulk trihalide perovskites and their nanoparticles, Chem. Commun. 53 (21) (2017) 3046–3049, https://doi.org/10.1039/C7CC00666G.
[161] Z.-Y. Zhu, et al., Solvent-free mechanosynthesis of composition-tunable cesium lead halide perovskite quantum dots, J. Phys. Chem. Lett. 8 (7) (Apr. 2017) 1610–1614, https://doi.org/10.1021/acs.jpclett.7b00431.
[162] L. Protesescu, S. Yakunin, O. Nazarenko, D.N. Dirin, M.V. Kovalenko, Low-cost synthesis of highly luminescent colloidal lead halide perovskite nanocrystals by wet ball milling, ACS Appl. Nano Mater. 1 (3) (Mar. 2018) 1300–1308, https://doi.org/10.1021/acsanm.8b00038.
[163] C.A. López, et al., Crystal structure features of CsPbBr $_{3}$ perovskite prepared by mechanochemical synthesis, ACS Omega 5 (11) (Mar. 2020) 5931–5938, https://doi.org/10.1021/acsomega.9b04248.
[164] W. Liu, et al., Luminescence, stability, and applications of CsPbBr3 quantum dot/polymethyl methacrylate composites prepared by a solvent- and ligand-free ball milling method, Opt. Mater. 136 (Feb. 2023) 113398, https://doi.org/10.1016/j.optmat.2022.113398.
[165] J. Kim, et al., Improving the stability of ball-milled lead halide perovskites via ethanol/water-induced phase transition, Nanomaterials 12 (6) (Mar. 2022) 920, https://doi.org/10.3390/nano12060920.

[166] J. Butkus, et al., The evolution of quantum confinement in $CsPbBr_3$ perovskite nanocrystals, Chem. Mater. 29 (8) (Apr. 2017) 3644–3652, https://doi.org/10.1021/acs.chemmater.7b00478.

[167] J. Shamsi, A.S. Urban, M. Imran, L. De Trizio, L. Manna, Metal halide perovskite nanocrystals: synthesis, post-synthesis modifications, and their optical properties, Chem. Rev. 119 (5) (Mar. 2019) 3296–3348, https://doi.org/10.1021/acs.chemrev.8b00644.

[168] Y. Li, X. Luo, Y. Liu, X. Lu, K. Wu, Size- and composition-dependent exciton spin relaxation in lead halide perovskite quantum dots, ACS Energy Lett. 5 (5) (May 2020) 1701–1708, https://doi.org/10.1021/acsenergylett.0c00525.

[169] M. Gao, et al., Scaling laws of exciton recombination kinetics in low dimensional halide perovskite nanostructures, J. Am. Chem. Soc. 142 (19) (May 2020) 8871–8879, https://doi.org/10.1021/jacs.0c02000.

[170] X. Peng, An essay on synthetic chemistry of colloidal nanocrystals, Nano Res. 2 (6) (Jun. 2009) 425–447, https://doi.org/10.1007/s12274-009-9047-2.

[171] J. Kang, L.-W. Wang, High defect tolerance in lead halide perovskite $CsPbBr_3$, J. Phys. Chem. Lett. 8 (2) (Jan. 2017) 489–493, https://doi.org/10.1021/acs.jpclett.6b02800.

[172] H. Huang, M.I. Bodnarchuk, S.V. Kershaw, M.V. Kovalenko, A.L. Rogach, Lead halide perovskite nanocrystals in the research spotlight: stability and defect tolerance, ACS Energy Lett. 2 (9) (Sep. 2017) 2071–2083, https://doi.org/10.1021/acsenergylett.7b00547.

[173] A. Pan, et al., Insight into the ligand-mediated synthesis of colloidal $CsPbBr_3$ perovskite nanocrystals: the role of organic acid, base, and cesium precursors, ACS Nano 10 (8) (Aug. 2016) 7943, https://doi.org/10.1021/acsnano.6b03863. –7954.

[174] F. Zhang, et al., Ligand-controlled formation and photoluminescence properties of $CH_3NH_3PbBr_3$ nanocubes and nanowires, ChemNanoMat 3 (5) (May 2017) 303–310, https://doi.org/10.1002/cnma.201700034.

[175] M. Liu, A. Matuhina, H. Zhang, P. Vivo, Advances in the stability of halide perovskite nanocrystals, Materials 12 (22) (Nov. 2019) 3733, https://doi.org/10.3390/ma12223733.

[176] L. Peng, et al., Arm growth and facet modulation in perovskite nanocrystals, J. Am. Chem. Soc. 141 (40) (Oct. 2019) 16160–16168, https://doi.org/10.1021/jacs.9b09157.

[177] W. Zhai, et al., Solvothermal synthesis of ultrathin cesium lead halide perovskite nanoplatelets with tunable lateral sizes and their reversible transformation into $Cs_4PbBr_6$ nanocrystals, Chem. Mater. 30 (11) (Jun. 2018) 3714–3721, https://doi.org/10.1021/acs.chemmater.8b00612.

[178] Y. Dong, T. Qiao, D. Kim, D. Parobek, D. Rossi, D.H. Son, Precise control of quantum confinement in cesium lead halide perovskite quantum dots via thermodynamic equilibrium, Nano Lett. 18 (6) (Jun. 2018) 3716–3722, https://doi.org/10.1021/acs.nanolett.8b00861.

[179] Q.A. Akkerman, et al., Solution synthesis approach to colloidal cesium lead halide perovskite nanoplatelets with monolayer-level thickness control, J. Am. Chem. Soc. 138 (3) (Jan. 2016) 1010–1016, https://doi.org/10.1021/jacs.5b12124.

[180] J. Li, et al., Ultrafast optical nonlinearity of blue-emitting perovskite nanocrystals, Photon. Res. 6 (6) (Jun. 2018) 554, https://doi.org/10.1364/PRJ.6.000554.

[181] F. Xu, et al., Quantum size effect and surface defect passivation in size-controlled CsPbBr3 quantum dots, J. Alloys Compd. 831 (Aug. 2020) 154834, https://doi.org/10.1016/j.jallcom.2020.154834.

[182] P. Sharma, S. Ganti, N. Bhate, Effect of surfaces on the size-dependent elastic state of nano-inhomogeneities, Appl. Phys. Lett. 82 (4) (Jan. 2003) 535–537, https://doi.org/10.1063/1.1539929.

[183] L. Polavarapu, B. Nickel, J. Feldmann, A.S. Urban, Advances in quantum-confined perovskite nanocrystals for optoelectronics, Adv. Energy Mater. 7 (16) (Aug. 2017) 1700267, https://doi.org/10.1002/aenm.201700267.

[184] S.M.H. Qaid, B.A. Al-Asbahi, H.M. Ghaithan, M.S. AlSalhi, A.S. Al Dwayyan, Optical and structural properties of CsPbBr3 perovskite quantum dots/PFO polymer composite thin films, J. Colloid Interface Sci. 563 (Mar. 2020) 426–434, https://doi.org/10.1016/j.jcis.2019.12.094.

[185] P. Ramasamy, D.-H. Lim, B. Kim, S.-H. Lee, M.-S. Lee, J.-S. Lee, All-inorganic cesium lead halide perovskite nanocrystals for photodetector applications, Chem. Commun. 52 (10) (2016) 2067–2070, https://doi.org/10.1039/C5CC08643D.

[186] F. Hu, et al., Superior optical properties of perovskite nanocrystals as single photon emitters, ACS Nano 9 (12) (Dec. 2015) 12410–12416, https://doi.org/10.1021/acsnano.5b05769.

[187] J. Liu, R. Papadakis, H. Li, Experimental observation of size-dependent behavior in surface energy of gold nanoparticles through atomic force microscope, Appl. Phys. Lett. 113 (8) (Aug. 2018) 083108, https://doi.org/10.1063/1.5046736.

[188] S.M.H. Qaid, M.N. Khan, A. Alqasem, M. Hezam, A. Aldwayyan, Restraining effect of film thickness on the behaviour of amplified spontaneous emission from methylammonium lead iodide perovskite, IET Optoelectron. 13 (1) (Feb. 2019) 2–6, https://doi.org/10.1049/iet-opt.2018.5035.

[189] S. Masi, et al., Growing perovskite into polymers for easy-processable optoelectronic devices, Sci. Rep. 5 (1) (Jan. 2015) 7725, https://doi.org/10.1038/srep07725.

[190] V.K. Ravi, G.B. Markad, A. Nag, Band edge energies and excitonic transition probabilities of colloidal $CsPbX_3$ (X = Cl, Br, I) perovskite nanocrystals, ACS Energy Lett. 1 (4) (Oct. 2016) 665–671, https://doi.org/10.1021/acsenergylett.6b00337.

[191] N.S. Makarov, S. Guo, O. Isaienko, W. Liu, I. Robel, V.I. Klimov, Spectral and dynamical properties of single excitons, biexcitons, and trions in cesium–lead-halide perovskite quantum dots, Nano Lett. 16 (4) (Apr. 2016) 2349–2362, https://doi.org/10.1021/acs.nanolett.5b05077.

[192] D.J. Clark, C.C. Stoumpos, F.O. Saouma, M.G. Kanatzidis, J.I. Jang, Polarization-selective three-photon absorption and subsequent photoluminescence in CsPbBr 3 single crystal at room temperature, Phys. Rev. B 93 (19) (May 2016) 195202, https://doi.org/10.1103/PhysRevB.93.195202.

[193] G.R. Yettapu, et al., Terahertz conductivity within colloidal $CsPbBr_3$ perovskite nanocrystals: remarkably high carrier mobilities and large diffusion lengths, Nano Lett. 16 (8) (Aug. 2016) 4838–4848, https://doi.org/10.1021/acs.nanolett.6b01168.

[194] W.-G. Lu, et al., Nonlinear optical properties of colloidal $CH_3NH_3PbBr_3$ and $CsPbBr_3$ quantum dots: a comparison study using Z-scan technique, Adv. Opt. Mater. 4 (11) (Nov. 2016) 1732–1737, https://doi.org/10.1002/adom.201600322.

[195] S. Sarkar, S. Banerjee, A. Swarnkar, P. Mandal, Effect of capping ligand engineering on transport properties and carrier dynamics in cubic $CsPbI_3$ nanocrystal film, J. Phys. Chem. C 125 (19) (May 2021) 10539–10548, https://doi.org/10.1021/acs.jpcc.1c02350.

[196] S. Gutiérrez Álvarez, et al., Charge carrier diffusion dynamics in multisized quaternary alkylammonium-capped $CsPbBr_3$ perovskite nanocrystal solids, ACS Appl. Mater. Interfaces 13 (37) (Sep. 2021) 44742, https://doi.org/10.1021/acsami.1c11676. –44750.

[197] D.K. Chaudhary, A. Ghosh, Md Y. Ali, S. Bhattacharyya, Charge transport between coaxial polymer nanorods and grafted all-inorganic perovskite nanocrystals for hybrid organic solar cells with enhanced photoconversion efficiency, J. Phys. Chem. C 124 (1) (Jan. 2020) 246–255, https://doi.org/10.1021/acs.jpcc.9b11303.

[198] Y. Kang, S. Han, Intrinsic carrier mobility of cesium lead halide perovskites, Phys. Rev. Appl. 10 (4) (Oct. 2018) 044013, https://doi.org/10.1103/PhysRevApplied.10.044013.

[199] Y. Su, et al., Highly controllable and efficient synthesis of mixed-halide $CsPbX_3$ (X = Cl, Br, I) perovskite QDs toward the tunability of entire visible light, ACS Appl. Mater. Interfaces 9 (38) (Sep. 2017) 33020–33028, https://doi.org/10.1021/acsami.7b10612.

[200] Y. Song, et al., Temperature-dependent photoluminescence of cesium lead halide perovskite ($CsPbX_3$, X = Br, Cl, I) quantum dots, Mater. Res. Express 6 (11) (Oct. 2019) 115064, https://doi.org/10.1088/2053-1591/ab4911.

[201] W. Song, B. Zhang, W. Zhou, J. Zhang, L. Yu, S. Lian, Suppression of thermal quenching for $CsPbX_3$ (X = Cl, Br, and I) quantum dots via the hollow structure of $SrTiO_3$ and light-emitting diode applications, Inorg. Chem. 61 (49) (Dec. 2022) 19899–19906, https://doi.org/10.1021/acs.inorgchem.2c03141.

[202] X. Li, et al., All inorganic halide perovskites nanosystem: synthesis, structural features, optical properties and optoelectronic applications, Small 13 (9) (Mar. 2017) 1603996, https://doi.org/10.1002/smll.201603996.

[203] Y. Liu, et al., Considerably enhanced exciton emission of $CsPbCl_3$ perovskite quantum dots by the introduction of potassium and lanthanide ions, Nanoscale 10 (29) (2018) 14067–14072, https://doi.org/10.1039/C8NR03581D.

[204] N. Wu, et al., Rubidium ions doping to improve the photoluminescence properties of Mn doped $CsPbCl_3$ perovskite quantum dots, Nanotechnology 34 (14) (Apr. 2023) 145701, https://doi.org/10.1088/1361-6528/ac9b62.

[205] J. Lin, L. Gomez, C. de Weerd, Y. Fujiwara, T. Gregorkiewicz, K. Suenaga, Direct observation of band structure modifications in nanocrystals of $CsPbBr_3$ perovskite, Nano Lett. 16 (11) (Nov. 2016) 7198–7202, https://doi.org/10.1021/acs.nanolett.6b03552.

[206] F. Liu, et al., Near-infrared emission from tin–lead (Sn–Pb) alloyed perovskite quantum dots by sodium doping, Angew. Chem. Int. Ed. 59 (22) (May 2020) 8421–8424, https://doi.org/10.1002/anie.201916020.

[207] J. Jiang, F. Liu, Q. Shen, S. Tao, The role of sodium in stabilizing tin–lead (Sn–Pb) alloyed perovskite quantum dots, J. Mater. Chem. A 9 (20) (2021) 12087–12098, https://doi.org/10.1039/D1TA00955A.

[208] P. Todorović, et al., Spectrally tunable and stable electroluminescence enabled by rubidium doping of $CsPbBr_3$ nanocrystals, Adv. Opt. Mater. 7 (24) (Dec. 2019) 1901440, https://doi.org/10.1002/adom.201901440.

[209] H. Wu, et al., The dual-defect passivation role of lithium bromide doping in reducing the nonradiative loss in $CsPbX_3$ (X = Br and I) quantum dots, Inorg. Chem. Front. 8 (3) (2021) 658–668, https://doi.org/10.1039/D0QI01262A.

[210] K.R. Pradeep, S. Chakraborty, R. Viswanatha, Stability of Sn based inorganic perovskite quantum dots, Mater. Res. Express 6 (11) (Nov. 2019) 114004, https://doi.org/10.1088/2053-1591/ab5121.

[211] H. Xu, et al., Lead-free bright blue light-emitting cesium halide nanocrystals by zinc doping, RSC Adv. 11 (4) (2021) 2437–2445, https://doi.org/10.1039/D0RA09705E.

[212] D. Chen, et al., Halogen-hot-injection synthesis of Mn-doped $CsPb(Cl/Br)_3$ nanocrystals with blue/orange dual-color luminescence and high photoluminescence quantum yield, Adv. Opt. Mater. 7 (23) (Dec. 2019) 1901082, https://doi.org/10.1002/adom.201901082.

[213] A.A. Bhat, S.A. Khandy, I. Islam, R. Tomar, Optical, electrochemical and photocatalytic properties of cobalt doped CsPbCl3 nanostructures: a one-pot synthesis approach, Sci. Rep. 11 (1) (Aug. 2021) 16473, https://doi.org/10.1038/s41598-021-95088-2.

[214] I.D. Skurlov, et al., Improved one- and multiple-photon excited photoluminescence from Cd2+-doped CsPbBr3 perovskite NCs, Nanomaterials 12 (1) (Jan. 2022) 151, https://doi.org/10.3390/nano12010151.

[215] Y. Xu, et al., Strontium-doped $CsPbI_3$ quantum dots as an interfacial layer for efficient inorganic perovskite solar cells, Sol. RRL 5 (12) (Dec. 2021) 2100669, https://doi.org/10.1002/solr.202100669.

[216] F. Zeng, Y. Tan, W. Hu, X. Tang, X. Zhang, H. Yin, A facile strategy to synthesize high colour purity blue luminescence aluminium-doped CsPbBr3 perovskite

quantum dots, J. Lumin. 245 (May 2022) 118788, https://doi.org/10.1016/j.jlumin.2022.118788.
[217] Y. Zhou, J. Chen, O.M. Bakr, H.-T. Sun, Metal-doped lead halide perovskites: synthesis, properties, and optoelectronic applications, Chem. Mater. 30 (19) (Oct. 2018) 6589–6613, https://doi.org/10.1021/acs.chemmater.8b02989.
[218] Y. Zhu, et al., Stable Dy-doped CsPbBr3 quantum dot glass with enhanced optical performance, J. Non-Cryst. Solids 575 (Jan. 2022) 121224, https://doi.org/10.1016/j.jnoncrysol.2021.121224.
[219] J. Shi, et al., Efficient and stable CsPbI $_3$ perovskite quantum dots enabled by in situ ytterbium doping for photovoltaic applications, J. Mater. Chem. A 7 (36) (2019) 20936–20944, https://doi.org/10.1039/C9TA07143A.
[220] Y. Wu, et al., Strategies of improving CsPbX3 perovskite quantum dots optical performance, Front. Mater. 9 (Mar. 2022) 845977, https://doi.org/10.3389/fmats.2022.845977.
[221] R. Sun, D. Zhou, H. Song, Rare earth doping in perovskite luminescent nanocrystals and photoelectric devices, Nano Sel. 3 (3) (Mar. 2022) 531–554, https://doi.org/10.1002/nano.202100187.
[222] W. Duan, L. Hu, W. Zhao, X. Zhang, Rare-earth ion-doped perovskite quantum dots: synthesis and optoelectronic properties, J. Mater. Sci. Mater. Electron. 33 (24) (Aug. 2022) 19019–19025, https://doi.org/10.1007/s10854-022-08737-1.
[223] Q. Zhong, et al., L-type ligand-assisted acid-free synthesis of CsPbBr $_3$ nanocrystals with near-unity photoluminescence quantum yield and high stability, Nano Lett. 19 (6) (Jun. 2019) 4151–4157, https://doi.org/10.1021/acs.nanolett.9b01666.
[224] Z. Liu, et al., Ligand mediated transformation of cesium lead bromide perovskite nanocrystals to lead depleted Cs $_4$ PbBr $_6$ nanocrystals, J. Am. Chem. Soc. 139 (15) (Apr. 2017) 5309–5312, https://doi.org/10.1021/jacs.7b01409.
[225] Y. Liu, et al., Ligands for CsPbBr3 perovskite quantum dots: the stronger the better? Chem. Eng. J. 453 (Feb. 2023) 139904 https://doi.org/10.1016/j.cej.2022.139904.
[226] D. Yang, et al., CsPbBr $_3$ quantum dots 2.0: benzenesulfonic acid equivalent ligand awakens complete purification, Adv. Mater. (Jun. 2019) 1900767, https://doi.org/10.1002/adma.201900767.
[227] L. Wu, et al., Improving the stability and size tunability of cesium lead halide perovskite nanocrystals using trioctylphosphine oxide as the capping ligand, Langmuir 33 (44) (Nov. 2017) 12689–12696, https://doi.org/10.1021/acs.langmuir.7b02963.
[228] Y. Huang, W. Luan, M. Liu, L. Turyanska, DDAB-assisted synthesis of iodine-rich CsPbI $_3$ perovskite nanocrystals with improved stability in multiple environments, J. Mater. Chem. C 8 (7) (2020) 2381–2387, https://doi.org/10.1039/C9TC06566K.
[229] W. Yin, et al., Multidentate ligand polyethylenimine enables bright color-saturated blue light-emitting diodes based on CsPbBr $_3$ nanoplatelets, ACS Energy Lett. 6 (2) (Feb. 2021) 477–484, https://doi.org/10.1021/acsenergylett.0c02651.
[230] J. Pan, et al., Highly efficient perovskite-quantum-dot light-emitting diodes by surface engineering, Adv. Mater. 28 (39) (Oct. 2016) 8718–8725, https://doi.org/10.1002/adma.201600784.
[231] B.-B. Zhang, et al., General mild reaction creates highly luminescent organic-ligand-lacking halide perovskite nanocrystals for efficient light-emitting diodes, J. Am. Chem. Soc. 141 (38) (Sep. 2019) 15423–15432, https://doi.org/10.1021/jacs.9b08140.
[232] L. Zhu, C. Wu, S. Riaz, J. Dai, Stable silica coated DDAB-CsPbX3 quantum dots and their application for white light-emitting diodes, J. Lumin. 233 (May 2021) 117884, https://doi.org/10.1016/j.jlumin.2021.117884.
[233] X. Tang, et al., Ultrathin, core–shell structured SiO $_2$ coated Mn $^{2+}$ -doped perovskite quantum dots for bright white light-emitting diodes, Small 15 (19) (May 2019) 1900484, https://doi.org/10.1002/smll.201900484.
[234] C. Sun, et al., Efficient and stable white LEDs with silica-coated inorganic perovskite quantum dots, Adv. Mater. 28 (45) (Dec. 2016) 10088–10094, https://doi.org/10.1002/adma.201603081.
[235] Z. Hu, et al., Enhanced two-photon-pumped emission from in situ synthesized nonblinking CsPbBr $_3$/SiO $_2$ nanocrystals with excellent stability, Adv. Opt. Mater. 6 (3) (Feb. 2018) 1700997, https://doi.org/10.1002/adom.201700997.
[236] J. Ziegler, et al., Silica-coated InP/ZnS nanocrystals as converter material in white LEDs, Adv. Mater. 20 (21) (Nov. 2008) 4068–4073, https://doi.org/10.1002/adma.200800724.
[237] H. Xie, E. Chen, Y. Ye, S. Xu, T. Guo, Interfacial optimization of quantum dot and silica hybrid nanocomposite for simultaneous enhancement of fluorescence retention and stability, Appl. Phys. Lett. 117 (17) (Oct. 2020) 171101, https://doi.org/10.1063/5.0026314.
[238] C. Zhang, et al., Exciton photoluminescence of CsPbBr $_3$ @SiO $_2$ quantum dots and its application as a phosphor material in light-emitting devices, Opt. Mater. Express 10 (4) (Apr. 2020) 1007, https://doi.org/10.1364/OME.389847.
[239] F. Gao, et al., Highly stable and luminescent silica-coated perovskite quantum dots at nanoscale-particle level via nonpolar solvent synthesis, Chem. Eng. J. 407 (Mar. 2021) 128001, https://doi.org/10.1016/j.cej.2020.128001.
[240] A. Loiudice, S. Saris, E. Oveisi, D.T.L. Alexander, R. Buonsanti, CsPbBr3 QD/AlOx inorganic nanocomposites with exceptional stability in water, light, and heat, Angew Chem. Int. Ed. Engl. 56 (36) (Aug. 2017) 10696–10701, https://doi.org/10.1002/anie.201703703.
[241] Z. Li, et al., Photoelectrochemically active and environmentally stable CsPbBr $_3$/TiO $_2$ core/shell nanocrystals, Adv. Funct. Mater. 28 (1) (Jan. 2018) 1704288, https://doi.org/10.1002/adfm.201704288.
[242] Y. Wei, et al., Highly luminescent lead halide perovskite quantum dots in hierarchical CaF $_2$ matrices with enhanced stability as phosphors for white light-emitting diodes, Adv. Opt. Mater. 6 (11) (Jun. 2018) 1701343, https://doi.org/10.1002/adom.201701343.
[243] Y. Cai, Y. Li, L. Wang, R. Xie, A facile synthesis of water-resistant CsPbBr $_3$ perovskite quantum dots loaded poly(methyl methacrylate) composite microspheres based on in situ polymerization, Adv. Opt. Mater. 7 (22) (Nov. 2019) 1901075, https://doi.org/10.1002/adom.201901075.
[244] J. Xu, et al., Transient optical properties of CsPbX $_3$/Poly(maleic anhydride- alt -1-octadecene) perovskite quantum dots for white light-emitting diodes, Phys. Status Solidi RRL – Rapid Res. Lett. 15 (1) (Jan. 2021) 2000498, https://doi.org/10.1002/pssr.202000498.
[245] P. Aryal, et al., Rapid and convenient crystallization of quantum dot CsPbBr3 inside a phosphate glass matrix, J. Alloys Compd. 866 (Jun. 2021) 158974, https://doi.org/10.1016/j.jallcom.2021.158974.
[246] X. Guo, H. Xie, W. Cai, F. Wang, B. Xu, C. Yang, Preparation of ultrastable and highly luminescent CsPbBr $_3$ quantum dots by a synergistic internal and external strategy of ligand modification and silica coating, J. Phys. Chem. C 127 (45) (Nov. 2023) 22139–22148, https://doi.org/10.1021/acs.jpcc.3c05055.
[247] M.A. Haque, A. Lohar, R. Gahlaut, I. Shaikh, S. Sartale, S. Mahamuni, The effect of surface treatment and polymer matrix on photoluminescence intermittency of strongly confined CsPbBr3 quantum dots, J. Mater. Sci. Mater. Electron. 34 (22) (Aug. 2023) 1642, https://doi.org/10.1007/s10854-023-11016-2.
[248] H. Ebe, et al., Guanidium iodide treatment of size-controlled CsPbI3 quantum dots for stable crystal phase and highly efficient red LEDs, Chem. Eng. J. 471 (Sep. 2023) 144578, https://doi.org/10.1016/j.cej.2023.144578.
[249] W. Stöber, A. Fink, E. Bohn, Controlled growth of monodisperse silica spheres in the micron size range, J. Colloid Interface Sci. 26 (1) (Jan. 1968) 62–69, https://doi.org/10.1016/0021-9797(68)90272-5.
[250] T.C. Sum, N. Mathews, Advancements in perovskite solar cells: photophysics behind the photovoltaics, Energy Environ. Sci. 7 (8) (2014) 2518–2534, https://doi.org/10.1039/C4EE00673A.
[251] I. Dursun, et al., Perovskite nanocrystals as a color converter for visible light communication, ACS Photonics 3 (7) (Jul. 2016) 1150–1156, https://doi.org/10.1021/acsphotonics.6b00187.
[252] D. Shi, et al., Low trap-state density and long carrier diffusion in organolead trihalide perovskite single crystals, Science 347 (6221) (Jan. 2015) 519–522, https://doi.org/10.1126/science.aaa2725.
[253] Q. Dong, et al., Electron-hole diffusion lengths > 175 μm in solution-grown CH $_3$ NH $_3$ PbI $_3$ single crystals, Science 347 (6225) (Feb. 2015) 967–970, https://doi.org/10.1126/science.aaa5760.
[254] T. Chiba, J. Kido, Lead halide perovskite quantum dots for light-emitting devices, J. Mater. Chem. C 6 (44) (2018) 11868–11877, https://doi.org/10.1039/C8TC03561J.
[255] X. Du, et al., High-quality CsPbBr $_3$ perovskite nanocrystals for quantum dot light-emitting diodes, RSC Adv. 7 (17) (2017) 10391–10396, https://doi.org/10.1039/C6RA27665B.
[256] T. Fang, T. Wang, X. Li, Y. Dong, S. Bai, J. Song, Perovskite QLED with an external quantum efficiency of over 21% by modulating electronic transport, Sci. Bull. 66 (1) (Jan. 2021) 36–43, https://doi.org/10.1016/j.scib.2020.08.025.
[257] G. Li, J. Huang, H. Zhu, Y. Li, J.-X. Tang, Y. Jiang, Surface ligand engineering for near-unity quantum yield inorganic halide perovskite QDs and high-performance QLEDs, Chem. Mater. 30 (17) (Sep. 2018) 6099–6107, https://doi.org/10.1021/acs.chemmater.8b02544.
[258] Q. Zhang, M. Jiang, G. Yan, Y. Feng, B. Zhang, Surface ligand engineering involving fluorophenethyl ammonium for stable and strong emission CsPbBr $_3$ quantum dots and high-performance QLEDs, J. Mater. Chem. C 10 (15) (2022) 5849–5855, https://doi.org/10.1039/D2TC00034B.
[259] C. Wu, H. Zhang, S. Wang, W. Wang, J. Dai, Room-temperature one-pot synthesis of highly stable SiO2-coated Mn-doped all-inorganic perovskite CsPb0.7Mn0.3Br0.75Cl2.25 quantum dots for bright white light-emitting diodes, J. Lumin. 223 (Jul. 2020) 117236, https://doi.org/10.1016/j.jlumin.2020.117236.
[260] E. Moyen, H. Jun, H.-M. Kim, J. Jang, Surface engineering of room temperature-grown inorganic perovskite quantum dots for highly efficient inverted light-emitting diodes, ACS Appl. Mater. Interfaces 10 (49) (Dec. 2018) 42647–42656, https://doi.org/10.1021/acsami.8b15212.
[261] H.-S. Yun, et al., CsPbBr $_3$ perovskite quantum dot light-emitting diodes using atomic layer deposited Al $_2$ O $_3$ and ZnO interlayers, Phys. Status Solidi RRL – Rapid Res. Lett. 14 (1) (Jan. 2020) 1900573, https://doi.org/10.1002/pssr.201900573.
[262] D. Yan, Q. Mo, S. Zhao, W. Cai, Z. Zang, Room temperature synthesis of Sn $^{2+}$ doped highly luminescent CsPbBr $_3$ quantum dots for high CRI white light-emitting diodes, Nanoscale 13 (21) (2021) 9740–9746, https://doi.org/10.1039/D1NR01492G.
[263] X. Tang, et al., Ultrathin, core–shell structured SiO $_2$ coated Mn $^{2+}$ -doped perovskite quantum dots for bright white light-emitting diodes, Small 15 (19) (May 2019) 1900484, https://doi.org/10.1002/smll.201900484.
[264] Z. Wang, et al., Enhancing the brightness of CsPbBr $_3$ quantum dot electroluminescence light-emitting diodes by manipulation of PEDOT:PSS films, J. Mater. Chem. C 9 (44) (2021) 15910–15917, https://doi.org/10.1039/D1TC03943A.
[265] F. Chen, Q. Lin, H. Shen, A. Tang, Blue quantum dot-based electroluminescent light-emitting diodes, Mater. Chem. Front. 4 (5) (2020) 1340–1365, https://doi.org/10.1039/D0QM00029A.
[266] E.M. Sanehira, et al., Influence of electrode interfaces on the stability of perovskite solar cells: reduced degradation using MoO $_x$/Al for hole collection,

ACS Energy Lett. 1 (1) (Jul. 2016) 38–45, https://doi.org/10.1021/acsenergylett.6b00013.
[267] X. Ling, J. Yuan, W. Ma, The rise of colloidal lead halide perovskite quantum dot solar cells, Acc. Mater. Res. 3 (8) (Aug. 2022) 866–878, https://doi.org/10.1021/accountsmr.2c00081.
[268] D. Jia, et al., Surface matrix curing of inorganic CsPbI $_3$ perovskite quantum dots for solar cells with efficiency over 16, Energy Environ. Sci. 14 (8) (2021) 4599–4609, https://doi.org/10.1039/D1EE01463C.
[269] A. Sunny, S. Rahman, Most M. Khatun, S.R.A. Ahmed, Numerical study of high performance HTL-free CH $_3$ NH $_3$ SnI $_3$ -based perovskite solar cell by SCAPS-1D, AIP Adv. 11 (6) (Jun. 2021) 065102, https://doi.org/10.1063/5.0049646.
[270] J. Khan, I. Ullah, J. Yuan, CsPbI $_3$ perovskite quantum dot solar cells: opportunities, progress and challenges, Mater. Adv. 3 (4) (2022) 1931–1952, https://doi.org/10.1039/D1MA01075A.
[271] T. Ma, S. Wang, Y. Zhang, K. Zhang, L. Yi, The development of all-inorganic CsPbX3 perovskite solar cells, J. Mater. Sci. 55 (2) (Jan. 2020) 464–479, https://doi.org/10.1007/s10853-019-03974-y.
[272] M.B. Faheem, et al., All-inorganic perovskite solar cells: energetics, key challenges, and strategies toward commercialization, ACS Energy Lett. 5 (1) (Jan. 2020) 290–320, https://doi.org/10.1021/acsenergylett.9b02338.
[273] Y. Wang, Y. Chen, T. Zhang, X. Wang, Y. Zhao, Chemically stable black phase CsPbI $_3$ inorganic perovskites for high-efficiency photovoltaics, Adv. Mater. 32 (45) (Nov. 2020) 2001025, https://doi.org/10.1002/adma.202001025.
[274] N.A.N. Ouedraogo, et al., Stability of all-inorganic perovskite solar cells, Nano Energy 67 (Jan. 2020) 104249, https://doi.org/10.1016/j.nanoen.2019.104249.
[275] C. Zhang, et al., Inorganic halide perovskite materials and solar cells, Apl. Mater. 7 (12) (Dec. 2019) 120702, https://doi.org/10.1063/1.5117306.
[276] P. Luo, et al., Solvent engineering for ambient-air-processed, phase-stable CsPbI $_3$ in perovskite solar cells, J. Phys. Chem. Lett. 7 (18) (Sep. 2016) 3603–3608, https://doi.org/10.1021/acs.jpclett.6b01576.
[277] J. Yuan, et al., Band-aligned polymeric hole transport materials for extremely low energy loss α-CsPbI3 perovskite nanocrystal solar cells, Joule 2 (11) (Nov. 2018) 2450–2463, https://doi.org/10.1016/j.joule.2018.08.011.
[278] X. Huang, et al., B-site doping of CsPbI3 quantum dot to stabilize the cubic structure for high-efficiency solar cells, Chem. Eng. J. 421 (Oct. 2021) 127822, https://doi.org/10.1016/j.cej.2020.127822.
[279] L. Zhang, et al., All-inorganic CsPbI $_3$ quantum dot solar cells with efficiency over 16% by defect control, Adv. Funct. Mater. 31 (4) (Jan. 2021) 2005930, https://doi.org/10.1002/adfm.202005930.
[280] J. Shi, et al., Efficient and stable CsPbI $_3$ perovskite quantum dots enabled by in situ ytterbium doping for photovoltaic applications, J. Mater. Chem. A 7 (36) (2019) 20936–20944, https://doi.org/10.1039/C9TA07143A.
[281] C. Bi, et al., Stable CsPb $_{1-x}$ Zn $_x$ I $_3$ colloidal quantum dots with ultralow density of trap states for high-performance solar cells, Chem. Mater. 32 (14) (Jul. 2020) 6105–6113, https://doi.org/10.1021/acs.chemmater.0c01750.
[282] X. Zhang, et al., α-CsPbBr $_3$ perovskite quantum dots for application in semitransparent photovoltaics, ACS Appl. Mater. Interfaces 12 (24) (Jun. 2020) 27307–27315, https://doi.org/10.1021/acsami.0c07667.
[283] X. Zhang, et al., Homojunction perovskite quantum dot solar cells with over 1 μm-thick photoactive layer, Adv. Mater. 34 (2) (Jan. 2022) 2105977, https://doi.org/10.1002/adma.202105977.
[284] C. Lu, et al., Efficient inverted CsPbI3 perovskite solar cells fabricated in common air, Chem. Eng. J. 452 (Jan. 2023) 139495, https://doi.org/10.1016/j.cej.2022.139495.
[285] S. Akin, Y. Altintas, E. Mutlugun, S. Sonmezoglu, Cesium lead based inorganic perovskite quantum-dots as interfacial layer for highly stable perovskite solar cells with exceeding 21% efficiency, Nano Energy 60 (Jun. 2019) 557–566, https://doi.org/10.1016/j.nanoen.2019.03.091.
[286] J. Jiang, R. Li, D. Liu, H. Xie, Q. Zeng, Y. Li, Efficient and stable CsPbI $_2$ Br inorganic perovskite solar cell Co-modified with ionic liquids and quantum dots, ACS Appl. Energy Mater. 6 (10) (May 2023) 5378–5387, https://doi.org/10.1021/acsaem.3c00401.
[287] X. Lin, et al., Black phosphorus quantum dots as an effective perovskite interfacial modification layer for efficient low-temperature processed all-inorganic CsPbI2Br perovskite solar cells, Sol. Energy 206 (Aug. 2020) 793–798, https://doi.org/10.1016/j.solener.2020.06.053.
[288] X. Qi, et al., Quantum dot interface-mediated CsPbIBr $_2$ film growth and passivation for efficient carbon-based solar cells, ACS Appl. Mater. Interfaces 13 (46) (Nov. 2021) 55349–55357, https://doi.org/10.1021/acsami.1c16290.
[289] J.B. Hoffman, A.L. Schleper, P.V. Kamat, Transformation of sintered CsPbBr $_3$ nanocrystals to cubic CsPbI $_3$ and gradient CsPbBr $_x$ I $_{3-x}$ through halide exchange, J. Am. Chem. Soc. 138 (27) (Jul. 2016) 8603–8611, https://doi.org/10.1021/jacs.6b04661.
[290] Y. Wang, CsPbX3 perovskite quantum dot laser, Highlights Sci. Eng. Technol. 27 (Dec. 2022) 334–342, https://doi.org/10.54097/hset.v27i.3775.
[291] Q. Zhao, et al., Advantageous Properties of Halide Perovskite Quantum Dots towards Energy-Efficient Sustainable Applications, Green Energy Environ, 2023, https://doi.org/10.1016/j.gee.2023.04.001. S2468025723000559, Apr.
[292] Y. Wang, X. Li, V. Nalla, H. Zeng, H. Sun, Solution-processed low threshold vertical cavity surface emitting lasers from all-inorganic perovskite nanocrystals, Adv. Funct. Mater. 27 (13) (Apr. 2017) 1605088, https://doi.org/10.1002/adfm.201605088.
[293] Y. Wang, X. Li, V. Nalla, H. Zeng, H. Sun, Solution-processed low threshold vertical cavity surface emitting lasers from all-inorganic perovskite nanocrystals, Adv. Funct. Mater. 27 (13) (Apr. 2017) 1605088, https://doi.org/10.1002/adfm.201605088.
[294] H. Zhang, et al., The preparation and up-conversion properties of full spectrum CsPbX $_3$ (X = Cl, Br, I) quantum dot glasses, Nanoscale 11 (39) (2019) 18009–18014, https://doi.org/10.1039/C9NR06509A.
[295] S. Wang, et al., Erasable glass-stabilized perovskite quantum dots for NIR-laser-stimuli-responsive optical security, Cell Rep. Phys. Sci. 3 (3) (Mar. 2022) 100794, https://doi.org/10.1016/j.xcrp.2022.100794.
[296] Y. Wang, X. Li, J. Song, L. Xiao, H. Zeng, H. Sun, All-inorganic colloidal perovskite quantum dots: a new class of lasing materials with favorable characteristics, Adv. Mater. 27 (44) (Nov. 2015) 7101–7108, https://doi.org/10.1002/adma.201503573.
[297] V.I. Klimov, et al., Optical gain and stimulated emission in nanocrystal quantum dots, Science 290 (5490) (Oct. 2000) 314–317, https://doi.org/10.1126/science.290.5490.314.
[298] Y.-H. Hsieh, et al., Perovskite quantum dot lasing in a gap-plasmon nanocavity with ultralow threshold, ACS Nano 14 (9) (Sep. 2020) 11670–11676, https://doi.org/10.1021/acsnano.0c04224.
[299] X. Tang, et al., Room temperature single-photon emission and lasing for all-inorganic colloidal perovskite quantum dots, Nano Energy 28 (Oct. 2016) 462–468, https://doi.org/10.1016/j.nanoen.2016.08.062.
[300] D.-G. Zhang, L.-Y. Jian, Z.-L. Tseng, H.-M. Cheng, J.-H. Lin, Investigation of random lasing from all-inorganic halide perovskite quantum dots prepared under ambient conditions, Nanoscale 13 (5) (2021) 3246–3251, https://doi.org/10.1039/D0NR08326G.
[301] F. Paulus, C. Tyznik, O.D. Jurchescu, Y. Vaynzof, Switched-on: progress, challenges, and opportunities in metal halide perovskite transistors, Adv. Funct. Mater. 31 (29) (Jul. 2021) 2101029, https://doi.org/10.1002/adfm.202101029.
[302] Y. Chen, Y. Chu, X. Wu, W. Ou-Yang, J. Huang, High-performance inorganic perovskite quantum dot-organic semiconductor hybrid phototransistors, Adv. Mater. 29 (44) (Nov. 2017) 1704062, https://doi.org/10.1002/adma.201704062.
[303] S. Zhou, et al., Ag-doped halide perovskite nanocrystals for tunable band structure and efficient charge transport, ACS Energy Lett. 4 (2) (Feb. 2019) 534–541, https://doi.org/10.1021/acsenergylett.8b02478.
[304] J. Zhang, et al., Tailoring neuroplasticity in flexible perovskite QDs-based optoelectronic synaptic transistors by dual modes modulation, Nano Energy 95 (May 2022) 106987, https://doi.org/10.1016/j.nanoen.2022.106987.
[305] K. Wang, S. Dai, Y. Zhao, Y. Wang, C. Liu, J. Huang, Light-stimulated synaptic transistors fabricated by a facile solution process based on inorganic perovskite quantum dots and organic semiconductors, Small 15 (11) (Mar. 2019) 1900010, https://doi.org/10.1002/smll.201900010.
[306] S. Subramanian Periyal, M. Jagadeeswararao, S.E. Ng, R.A. John, N. Mathews, Halide perovskite quantum dots photosensitized-amorphous oxide transistors for multimodal synapses, Adv. Mater. Technol. 5 (11) (Nov. 2020) 2000514, https://doi.org/10.1002/admt.202000514.
[307] M. Dai, Z. Song, C.-H. Lin, Y. Dong, T. Wu, J. Chu, Multi-functional multi-gate one-transistor process-in-memory electronics with foundry processing and footprint reduction, Commun. Mater. 3 (1) (Jun. 2022) 41, https://doi.org/10.1038/s43246-022-00261-3.
[308] M.M. Shulaker, et al., Three-dimensional integration of nanotechnologies for computing and data storage on a single chip, Nature 547 (7661) (Jul. 2017) 74–78, https://doi.org/10.1038/nature22994.
[309] F. Rao, et al., Reducing the stochasticity of crystal nucleation to enable subnanosecond memory writing, Science 358 (6369) (Dec. 2017) 1423–1427, https://doi.org/10.1126/science.aao3212.
[310] V.K. Sangwan, et al., Multi-terminal memtransistors from polycrystalline monolayer molybdenum disulfide, Nature 554 (7693) (Feb. 2018) 500–504, https://doi.org/10.1038/nature25747.
[311] J.-M. Hu, L.-Q. Chen, C.-W. Nan, Multiferroic heterostructures integrating ferroelectric and magnetic materials, Adv. Mater. 28 (1) (Jan. 2016) 15–39, https://doi.org/10.1002/adma.201502824.
[312] F. Zahoor, T.Z. Azni Zulkifli, F.A. Khanday, Resistive random access memory (RRAM): an overview of materials, switching mechanism, performance, multilevel cell (mlc) storage, modeling, and applications, Nanoscale Res. Lett. 15 (1) (Dec. 2020) 90, https://doi.org/10.1186/s11671-020-03299-9.
[313] Y. Wang, et al., Synergies of electrochemical metallization and valance change in all-inorganic perovskite quantum dots for resistive switching, Adv. Mater. 30 (28) (Jul. 2018) 1800327, https://doi.org/10.1002/adma.201800327.
[314] Z. Chen, et al., Light assisted multilevel resistive switching memory devices based on all-inorganic perovskite quantum dots, Appl. Phys. Lett. 114 (18) (May 2019) 181103, https://doi.org/10.1063/1.5087594.
[315] M.-C. Yen, et al., All-inorganic perovskite quantum dot light-emitting memories, Nat. Commun. 12 (1) (Jul. 2021) 4460, https://doi.org/10.1038/s41467-021-24762-w.
[316] L. Vásárhelyi, Z. Kónya, Á. Kukovecz, R. Vajtai, Microcomputed tomography–based characterization of advanced materials: a review, Mater. Today Adv. 8 (Dec. 2020) 100084, https://doi.org/10.1016/j.mtadv.2020.100084.
[317] Y. Li, et al., Template-assisted fabrication of flexible perovskite scintillators for X-ray detection and imaging, Adv. Opt. Mater. 11 (16) (Aug. 2023) 2300169, https://doi.org/10.1002/adom.202300169.

[318] W. Ma, et al., Highly resolved and robust dynamic X-ray imaging using perovskite glass-ceramic scintillator with reduced light scattering, Adv. Sci. 8 (15) (Aug. 2021) 2003728, https://doi.org/10.1002/advs.202003728.
[319] Z.-W. Lü, et al., New flexible CsPbBr3-based scintillator for X-ray tomography, Nucl. Sci. Tech. 33 (8) (Aug. 2022) 98, https://doi.org/10.1007/s41365-022-01085-z.
[320] M. Hu, et al., A pixelated liquid perovskite array for high-sensitivity and high-resolution X-ray imaging scintillation screens, Nanoscale 15 (38) (2023) 15635–15642, https://doi.org/10.1039/D3NR02841K.